GDAŃSK UNIVERSITY OF TECHNOLOGY

The author of the doctoral dissertation: Parisa Radan
Scientific discipline: Civil Engineering, Geodesy and Transport

DOCTORAL DISSERTATION

Title of doctoral dissertation: Wind effect on ice dynamics

Title of doctoral dissertation (in Polish): Wpływ wiatru na dynamikę lodu

Supervisor *signature*
dr hab. Inż, Tomasz Kolerski, prof. PG

Gdańsk, 2024

POLITECHNIKA GDAŃSKA

STATEMENT

The author of the doctoral dissertation: Parisa, Radan

I, the undersigned, declare that I am aware that in accordance with the provisions of Art. 27 (1) and (2) of the Act of 4th February 1994 on Copyright and Related Rights (Journal of Laws of 2021, item 1062), the university may use my doctoral dissertation entitled:
Wind effect on ice dynamics
for scientific or didactic purposes.[1]

Gdańsk, ...
signature of the PhD student

Aware of criminal liability for violations of the Act of 4th February 1994 on Copyright and Related Rights and disciplinary actions set out in the Law on Higher Education and Science(Journal of Laws 2021, item 478), as well as civil liability, I declare, that the submitted doctoral dissertation is my own work.

I declare, that the submitted doctoral dissertation is my own work performed under and in cooperation with the supervision of Tomasz Kolerski.

This submitted doctoral dissertation has never before been the basis of an official procedure associated with the awarding of a PhD degree.

All the information contained in the above thesis which is derived from written and electronic sources is documented in a list of relevant literature in accordance with Art. 34 of the Copyright and Related Rights Act.

I confirm that this doctoral dissertation is identical to the attached electronic version.

Gdańsk,..... .....
signature of the PhD student

I, the undersigned, agree/~~do not agree~~* to include an electronic version of the above doctoral dissertation in the open, institutional, digital repository of Gdańsk University of Technology.

Gdańsk,..... .....
signature of the PhD student

**delete where appropriate*

[1] Art 27. 1. Educational institutions and entities referred to in art. 7 sec. 1 points 1, 2 and 4–8 of the Act of 20 July 2018 – Law on Higher Education and Science, may use the disseminated works in the original and in translation for the purposes of illustrating the content provided for didactic purposes or in order to conduct research activities, and to reproduce for this purpose disseminated minor works or fragments of larger works.

2. If the works are made available to the public in such a way that everyone can have access to them at the place and time selected by them, as referred to in para. 1, is allowed only for a limited group of people learning, teaching or conducting research, identified by the entities listed in paragraph 1.

GDAŃSK UNIVERSITY OF TECHNOLOGY

DESCRIPTION OF DOCTORAL DISSERTATION

The Author of the doctoral dissertation: Parisa Radan

Title of doctoral dissertation: Wind effect on ice dynamics

Title of doctoral dissertation in Polish: Wpływ wiatru na dynamikę lodu

Language of doctoral dissertation: English

Supervisor: Tomasz Kolerski

Date of doctoral defense:

Keywords of doctoral dissertation in Polish: Wpływ wiatru; Dryf lodu; Symulacja numeryczna; Model DynaRICE; Eksperyment w kanale falowym; Koncentracja lodu; Particle Image Velocimetry (PIV); Particle Tracking Velocimetry (PTV); Pomiar prędkości wiatru; Prędkość lodu; Pokrywa lodowa; Modelowanie eksperymentalne; Dynamika pola wodnego.

Keywords of doctoral dissertation in English: Wind effect; Ice drift; Numerical simulation; DynaRICE model; Wave flume experiment; Ice concentration; Particle Image Velocimetry (PIV); Particle Tracking Velocimetry (PTV); Wind velocity measurement; Ice velocity; Ice cover; Experimental modelling; Water field dynamics.

Summary of doctoral dissertation in Polish: Badanie dotyczy wpływu wiatru na prędkość lodu. W badaniach eksperymentalnych mierzono prędkość wiatru oraz lodu. Lód symulowano za pomocą palet polipropylenowych, a warunki termiczne nie były brane pod uwagę. Generator wiatru składający się z trzech wentylatorów generował trzy różne pola wiatrowe. Do eksperymentów uwzględniono dwa rozmiary lodu (o prostokątnym kształcie). Oba rodzaje lodu miały grubość 1 cm i prostokątny kształt. W przypadku rozmiaru 10×10 cm, zmiennym parametrem w eksperymentach była koncentracja lodu. Do eksperymentów użyto wody początkowej. Do pomiaru prędkości wiatru i wody zastosowano technikę PIV (ang. Particle Image Velocimetry), a do pomiaru prędkości lodu technikę PTV (ang. Particle Tracking Velocimetry).

Dostosowując współczynnik oporu aerodynamicznego w modelu DynaRICE z wartości 0,0015 do 0,002, 0,0025 oraz 0,009 dla odpowiednio wysokich, średnich i niskich prędkości wiatru, uzyskano wyniki prędkości lodu z modelu DynaRICE bliżej zgodne z wynikami eksperymentalnymi. Prędkości wiatru powyżej 2 m/s mają kluczowy wpływ na dynamikę lodu, co wskazuje, że domyślna wartość współczynnika oporu aerodynamicznego wynosząca 0,0015 jest odpowiednio zastosowana w modelu DynaRICE. Dalsze ulepszenia mogłyby zostać osiągnięte poprzez uwzględnienie zmian współczynnika oporu aerodynamicznego dla całego zakresu prędkości wiatru w modelu DynaRICE.

Summary of doctoral dissertation in English: The study is related to the wind effect on ice velocity. In the experimental study wind and ice velocities were measured. The ice was simulated with polypropylene pallets and no thermal condition was considered. A wind generator consisting of three fans would generate three different wind fields. Two ice sizes were considered for the experiments (with rectangular shape). These both types of ice had a thickness of 1cm and a rectangular shape. For the size of 10×10 cm, concentration of ice was a varying parameter for the experiments. Initial water was used for the experiments. For measuring wind and water velocity, PIV technique (Particle Image Velocimetry) and for ice velocity PTV technique (Particle Tracking Velocimetry) were used.
By adjusting the wind drag coefficient in the DynaRICE model from 0.0015 to 0.002, 0.0025, and 0.009 for high, medium, and low wind velocities, respectively, the ice velocity results from the DynaRICE model more closely aligned with the ice velocity results from the experimental simulation. Wind velocities above 2 m/s primarily affect ice dynamics, indicating that the default value of 0.0015 for the wind drag coefficient is appropriately applied in the DynaRICE model. Further improvement could be achieved by accounting for changes in the wind drag coefficient under the entire range of wind velocity conditions within the DynaRICE model.

PhD thesis

Title

Wind effect on ice dynamics

By:

Parisa Radan

Supervisor:

Tomasz Kolerski

Discipline of Civil Engineering, Geodesy and Transport

Department of Geotechnical and Hydraulic Engineering

Faculty of Civil and Environmental Engineering

Gdańsk University of Technology

Gdańsk, December 2024

To my sister,

Pegah…

Contents

Abstract

This study relates to the wind effect on ice drift, utilizing both experimental and numerical simulations. The experiments were conducted in the wave flume at the Institute of Hydro-Engineering of the Polish Academy of Sciences (IHE PAS), where ice pieces (10×10 cm) and ice covers (40×50 cm) were simulated from propylene pallets. A water field (59.5 cm depth) was established, with a wind field (20 cm height) generated above it. Wind and water velocities were measured using Particle Image Velocimetry (PIV) and Particle Tracking Velocimetry (PTV) techniques. Three distinct wind fields were created using a wind generator, and subsequent statistical analyses of the PIV and PTV data were performed. The PIV technique employed water particles as seeding material, leading to reliable wind velocity measurements, verified against an anemometer. The obtained wind velocity and ice concentration were used as inputs for the numerical simulation with the DynaRICE model, and the ice velocity was captured from the simulation at the same scale as the physical model.

In conclusion, this study primarily investigated the effect of wind on ice, with emphasis on ice characteristics such as concentration and size. The PIV and PTV techniques produced reliable measurements, with the optimal categorization of PIV results aiding in determination of wind velocity. Results showed that wind velocity significantly influences ice velocity and impacts surface ice drift through ice concentration. An inverse linear relationship was observed between ice concentration and averaged ice velocity. The results of the DynaRICE model showed ice velocities that were closer to experimental values under high wind velocity conditions when using the default value of the wind drag coefficient (0.0015). Differences between ice cover and ice pieces velocities were also observed, with the DynaRICE model results. Future work should focus on optimizing the wind velocity measurement and examining a continuous range of ice velocity data for a deeper understanding of wind-ice dynamics.

Keywords: Wind effect; Ice drift; Numerical simulation; DynaRICE model; Wave flume experiment; Ice concentration; Particle Image Velocimetry (PIV); Particle Tracking Velocimetry (PTV); Wind velocity measurement; Ice velocity; Ice cover; Experimental modelling; Water field dynamics.

Niniejsza praca dotyczy wpływu wiatru na dryf lodu, wykorzystując zarówno badania eksperymentalne, jak i symulacje numeryczne z wykorzystaniem modelu DynaRICE. Eksperymenty przeprowadzono w kanale falowym w Instytucie Budownictwa Wodnego Polskiej Akademii Nauk (IBW PAN), gdzie symulowano kawałki lodu (10×10 cm) oraz pokrywę lodową (40×50 cm) z wykorzystaniem płyt polipropylenowych. W kanał napełniony był wodą do głębokości 59,5 cm, nad którym wytworzono 20 centymetrowy tunel w którym generowano pole wiatrowe. Prędkości wiatru i wody mierzono technikami PIV (Particle Image Velocimetry) i PTV (Particle Tracking Velocimetry). Za pomocą generatora wiatru stworzono trzy różne pola wiatrowe, a następnie przeprowadzono analizy statystyczne zebranych danych. Technika PIV wykorzystywała cząstki wody jako materiał znacznikowy, co pozwoliło na uzyskanie wiarygodnych pomiarów prędkości wiatru, zweryfikowanych za pomocą anemometru. Uzyskane prędkości wiatru oraz koncentracja lodu zostały wykorzystane jako dane wejściowe do symulacji numerycznej w modelu DynaRICE, a prędkość lodu została odwzorowana z modelu symulacyjnego w tej samej skali, co model fizyczny.

Podsumowując, niniejsze badanie koncentrowało się głównie na wpływie wiatru na lód, ze szczególnym uwzględnieniem cech lodu, takich jak koncentracja i rozmiar. Techniki PIV i PTV dostarczyły wiarygodnych pomiarów, a optymalna kategoryzacja wyników PIV pomogła w określeniu prędkości wiatru. Wyniki wykazały, że prędkość wiatru ma znaczący wpływ na prędkość lodu i oddziałuje na dryf powierzchniowy lodu poprzez koncentrację lodu. Zaobserwowano odwrotną zależność liniową między koncentracją lodu a średnią prędkością lodu. Wyniki modelu DynaRICE wykazały prędkości lodu bliższe wartościom eksperymentalnym w warunkach wysokiej prędkości wiatru, przy użyciu domyślnej wartości współczynnika oporu wiatru (0,0015). Zaobserwowano również różnice między prędkością pokrywy lodowej a prędkością fragmentów lodu w wynikach modelu DynaRICE. Przyszłe badania powinny skoncentrować się na optymalizacji pomiaru prędkości wiatru oraz analizie ciągłego zakresu danych dotyczących prędkości lodu, aby lepiej zrozumieć dynamikę wiatru i lodu.

Słowa kluczowe: Wpływ wiatru; Dryf lodu; Symulacja numeryczna; Model DynaRICE; Eksperyment w kanale falowym; Koncentracja lodu; Particle Image Velocimetry (PIV); Particle Tracking Velocimetry (PTV); Pomiar prędkości wiatru; Prędkość lodu; Pokrywa lodowa; Modelowanie eksperymentalne; Dynamika pola wodnego.

1 Introduction

1.1 Objectives of the study

The main objective of this study is to investigate the effect of wind on surface ice drift. Past literature contains limited studies related to the effect of wind on ice dynamics. Therefore, this study will consider different parameters attributed to ice dynamics under wind influence, including the size and concentration of the ice as well as wind velocity.

This study examines the effect of air movement on ice transport, particularly in stationary water bodies where wind drag predominates over water drag. The proposed solutions and research layout are original and based on our own perspectives. The study comprises experimental, analytical and numerical components. The experimental research is self-funded, with no commercial incentives, and aims to conduct basic experiments with cost considerations.

The first objective of the study is to perform experimental measurement on ice movement under the influence of different wind velocities. The experimental simulation involved several steps, starting with the preparation of the experimental set up. The experiments were conducted at the Institute of Hydro-Engineering of the Polish Academy of Sciences (IHE PAS), specifically in the wave flume. This flume had not previously been used for wind-related experiments, so it required additional equipment. The aim is to enhance the quality of this equipment for future studies. Since the experiments were not conducted in a cold room, ice had to be simulated using an appropriate material that fulfilled the required ice characteristics.

In this study, Particle Image Velocimetry (PIV) technique was used in both wind and water fields. Although, PIV measurements had been previously conducted for water in this flume, preparing the wind field for PIV measurement presented an unknown aspect of this study, including introducing seeding particles to the wind field. Efforts were made to identify proper seeding particles for wind field measurement. Since seeding a wind flume can be a challenging part of a study (Stanislas et al., 2013), special care was taken to select appropriate seeding particles for the wind field, based on the flume's characteristics. In the air, light will be diffused, if the properties of the seeding material allow it (Stanislas et al., 2013). Therefore, special attention was given to the introduction of seeding particles into the field. The

measurement of the wind velocity field was performed using the PIV technique with water particles as the seeding material, selected after testing other materials. It was also necessary to consider whether using water particles as seeding material might affect the PIV measurement results.

Both open and closed circuits were considered for the wind and water fields, respectively, with the wind field adjacent to the still water surface. To the Author's knowledge, past literature indicates that water particles have been used in PIV measurement at higher wind velocities than those in this study. Following the PIV measurement of the wind field, calibration of the wind velocity measurement was conducted using an anemometer device. Additionally, it was necessary to model ice with an appropriate material based on the experiment requirements. Different case scenarios were considered, varying parameters such as ice concentration, ice floe size and wind velocity. Experiments were planned to account for these parameters. For ice velocity measurement, the Particle Tracking Velocimetry (PTV) Technique was used with care taken to record the ice movement and calculate velocities. Statistical analysis was performed, on the results obtained from both the PIV and PTV techniques.

The second objective of the study is to simulate case scenarios using the DynaRICE model and compare the obtained ice velocities with the experimental simulation results. For this purpose, the wind velocities, ice concentrations, and sizes from the experimental simulations were used as the input data for the DynaRICE model.

1.2 Motivation behind the study

There is sufficient evidence of the wind's effect on river ice dynamics. A notable example is the severe ice flood on the Vistula River in 1982, partly caused by strong winds blowing in the opposite direction of the river flow in the upper part of Wloclawek Reservoir (Kołodko and Jackowski, 1984). Wind is considered the main drive of the ice movement in shallow inland water bodies, such as reservoirs, lakes, and lagoons. The drag exerted by the wind on ice can impose significant static loads on shores or structures (Shen et al., 1997). To properly design hydraulic structures, results from theoretical studies need to be complemented by laboratory experiments on ice forces (Kolerski et al., 2021). The study is motivated by the need to

investigate river ice dynamics influenced by wind, focusing on the ice characteristics themselves.

The current status of the wind drag formulation does not include many ice properties, such as concentration, size, and thickness. The aim of this study is to incorporate more parameters into the understanding of ice movement influenced by wind. This research provides a basis for developing a new formulation which will be more general and capable of reproducing ice dynamic with higher accuracy.

Considering various ice parameters under wind influence, experimental study was an important part of this study. Through experimental modelling, a prototype model was developed to observe the effects of changing wind velocity and ice piece characteristics on ice dynamic. One of the key parameters of wind shear tension on ice is the wind drag coefficient. This study aims to determine whether the wind shear tension formulation needs to consider the effects of ice concentration and size, which influence wind drag coefficient. Physical modelling is essential to set the formulation, considering the wind drag coefficient. For this aspect, modelling the real-case scenarios was needed.

The physical model was produced using the DynaRICE model, the most comprehensive mathematical model for river ice process. This physical model can be used for future studies related to real-case scenarios of wind effects on ice, particularly concerning interactions with river basins and hydraulic structures. Since ice jam can exert significant forces on hydraulic structures and cause noticeable changes to river basins, this study can be useful for the river management objectives.

2 Literature review

This section provides a review of previous studies related to the river ice processes, tension enforced on the ice by wind, laboratory experiments of river ice dynamics, Particle Image Velocimetry (PTV technique), Particle Tracking Velocimetry (PIV technique) and mathematical modelling are provided. These six subchapters serve as the background for this study. This study examines the ice drift under wind influence using both numerical and experimental simulations. The PIV technique is used to measure wind and water velocities, while the PTV technique measures ice velocity in experimental simulations. Ice velocity results from experimental simulations are compared with those from the numerical simulations using the DynaRICE model.

2.1 River ice processes

River ice process comprises various mechanical, hydrological, hydrodynamic, and meteorological phenomena related to the formation, transport, erosion, deterioration and jamming of different types of ice (Shen, 2010). Associated to the hydraulics aspects, the interactive ice effect on the rivers is of importance, therefore, in deep knowledge of river ice types needs to be achieved (Ashton, 1986). Various types of ice may form in different stages of ice process during wintertime.

The freeze-up process in rivers involves the formation of ice under various flow and thermal conditions, influenced significantly by the type of water flow and thermal stratification within the river (Hammar et al., 2002; Matousek, 1984). Two general types of ice formation are observed depending on the flow condition, which relates to the vertical mixing of water column (Shen, 1996).

Calm water conditions: In areas of calm water, typically near the edges or in sheltered sections of the river, the freeze-up process begins with the formation of skim ice (Kolerski and Shen, 2015; Michel and Ramseier, 1971). Skim ice forms when the surface water temperature drops below freezing, causing a thin layer of ice to develop on the surface. This initial ice layer can gradually thicken to form a complete ice cover over time as temperatures continue to drop.

Turbulent Flow Conditions: In sections of the river where there is turbulent flow, such as around rapids or areas with significant water movement, a different type of ice formation

occurs known as frazil ice (Osterkamp, 1978). Frazil ice forms from small ice crystals that develop in supercooled water, where the water temperature is below freezing but still in a liquid state. These ice crystals can aggregate and form a slushy or icy mixture that can accumulate and eventually coalesce into larger ice formations.

The thermocline refers to a distinct layer in a body of water characterized by a rapid change in temperature over a short vertical distance. In rivers, the thermocline plays a crucial role in influencing ice formation, particularly under calm water conditions (Beltaos and Prowse, 2009). In these areas, such as deep reservoirs or near riverbanks where there is minimal turbulence and low flow velocity, thermal stratification occurs as the water cools. Near freezing temperatures, lighter cold water remains at the surface and freezes quickly, while deeper layers of the water body maintain temperatures around 4 degrees Celsius.

Border ice, which is the ice formed along the shore is essential in freeze up processing; It influences ice generation, flow condition and cover formation (Huang et al., 2012). While skim ice is the flat aggregates of ice particles (element, containing a group of ice pieces), running on the surface of water, in the shape of grease layer or thin ice floes. Skim ice, in line with frazil, are the main types of ice run (Matousek, 1984; Shen et al., 2000). Ice run along the edges of border ice causes hydraulic accumulation, and as the consequence, the transactional growth of the border ice, up to the point of ice cover formation by surface ice accumulation (Huang et al., 2012).

Conversely, turbulent flow in rivers can disrupt the thermocline by mixing the water column. This turbulence occurs in areas with faster flow rates or around obstacles like rapids. The mixing action brings colder water from deeper layers to the surface, leading to the formation of frazil ice (Hammar and Shen, 1995). Frazil ice consists of small ice crystals that form in supercooled water, where the water temperature is below freezing but remains in a liquid state due to agitation and mixing caused by turbulent flow.

Frazil ice which is formed in the supercooled water temperature may initiate the formation of various ice types (Hammar and Shen, 1995). The vertical mixing of the frazil ice in the turbulent flow may result to the conglomeration of the frazil particles into flocs (Shen, 2010). Turbulence also plays a pivotal role in the dipping of the particles, preventing the formation of ice cover and thermal isolation. Therefore, turbulence is crucial for the continuous heat

transfer across the water depth to the atmosphere (Hammar and Shen, 1995). Along with supercooling condition and turbulence, the existence of the sufficient amount of seed ice crystals is necessary to fulfilling a good condition to proceed the ice conglomeration. The nucleation originates from falling cold dust into the water, and presence of supercooled ice and snow particles in the water. Once the seeding process commences, the ice particles will enlarge and augmented due to the latent heat transfer to the atmosphere and the heat exchange with the channel bed. Needless to say, the secondary nucleation caused by the collision of enlarged frazil particles to the boundaries or other flocs, leads to the multiplication of the particles. The enlargement and multiplication of the particles balance the latent heat transferred from the ice particles to the atmosphere by raising the water temperature to 0°C (Hammar and Shen, 1995).

In supercooling water, frazil particles can be in an active mode. In these situations, the particles not only grow, but they also can adhere to the equipment, such as in hydropower systems. This intern can cause power generation losses in the cold seasons (Gebre et al., 2013). To stimulating the formation of ice cover by reducing water discharge in power production plants, is an advantageous approach for thermal stabilization of the channel and frazil formation (Asvall, 2007). There are also following advantageous in the stimulated cover formation, such as, prohibition of ice jam formation downstream of the reservoirs, and the jam formation at the spillways. Apart from the importance of the action needed to be taken in the in relation to the ice formation regulation, the cover existence diminishes the power production capability of the river. The causes are the discharge reduction to progress the ice cover formation and its continuation, as well as head level depletion over the hydropower system. Therefore, the power production diminishes, and efficiency of the power production are needed to be taken into account (Yapa and Shen, 1984; Kolerski and Radan, 2022).

Once frazil particles are grown in size and increased in buoyancy, they float towards the water surface forming larger conglomerates. The concentration of the surface ice layer is considered as a higher magnitude, in comparison to the suspension ice; continuing growth of this parameter results in the formation of ice pans. Travelling downstream, due to the additionally accumulation of frazil, undersides and margins of the ice pans, as well as interspatial water freezing, strength and size of the ice pans increase. In case of travelling through long distances, ice pans may become as part of larger ice floes; crossing rapid sections, they may

break down in the shape of fragments. In case of existing obstacles on the path of the surface ice, ice cover extends upstream. The consolidation of the ice pieces at the leading edge of a cover (which firstly increases mass density to the maximum concentration, and further in case of possibility, increases the ice thickness), and the freeze up of the interstitial water between the ice pieces convert the ice pieces to the ice cover, due to the mechanical and thermal effects, respectively (Wazney et al., 2019). Due to the partially coverage of the water surface and the resultant thermal isolation, less ice production can be anticipated; the remaining frazil ice may travel underside of the cover, forming hanging dams (Lal and Shen, 1991).

In conclusion, the freeze-up process in rivers is a dynamic interplay of water flow, thermal conditions, and seasonal changes. Understanding these processes is crucial for assessing river ice hazards, managing water resources effectively, and mitigating risks to infrastructure and ecosystems along riverine environments.

Ice breakup typically occurs in the middle or end of the winter season and can be classified into two types: thermal and mechanical (Beltaos 1996). Thermal breakup is caused by increased air temperatures, which raise the temperature of the ice, leading to a weakening of the ice cover's strength (Beltaos, 2003; Shen and Huang, 2024). Rainfall also intensifies the process and causes rapid weakening of the ice cover's strength (Kolerski and Shen, 2015). Mechanical breakup, on the other hand, is triggered by an increase in water discharge in the river, which results in the breaking of the ice cover and the movement of ice downstream. The occurrence of breakup depends on climatic conditions, as variations in temperature and precipitation patterns significantly influence the timing and type of ice breakup.

Mechanical breakup of ice on rivers refers to the physical disintegration of river ice due to external forces, primarily caused by increasing water flow, temperature changes, or a combination of both. During the spring or midwinter thaw, as temperatures rise, snowmelt and increased precipitation contribute to higher water levels in rivers (Prowse et al., 2007). This adds pressure underneath the ice layer, leading to cracks and fractures. With snowmelt, the flow of water under the ice intensifies, exerting upward and lateral forces on the ice cover. This causes the ice to break apart into large chunks. Both wind and rain have impact on the breakup process. Wind can push the ice downstream, while rain can help melting it (Kolerski and Shen, 2015). These factors, combined with the mechanical forces from water flow, further fragment the ice. Mechanical breakup can be quite unpredictable and is influenced by

various environmental factors like river topography, the thickness of the ice, and regional weather patterns.

Since the border ice formation influences the emergence and progression of the ice cover, Huang et al. (2012) reviewed and unified a set of formulation related to these phenomena. This formulation was implemented to a two-dimensional thermal-dynamic model, being validated with the field data from the upper St. Lawrence River (Huang et al., 2012).

Liu and Shen (2000) developed a two-dimensional model for the ice transport simulation. In the model, the surface ice dynamic and the flow hydrodynamic were coupled. For the simulation of ice dynamics, smoothed particle hydrodynamics with Lagrangian discrete-parcel method, and for solving hydrodynamic equations, the Finite-element method was applied. Ice entering behind the booms, underside erosion of the ice accumulation and its leading edge, etc. were considered (Liu and Shen, 2000).

Zhai et al. (2022) developed a numerical model for the dynamics of river ice (DEMRICE), by means of the discrete element method. The aim was simulating ice jams (considering seepage flow through the ice), and ice floe movement under the influence of hydraulic variable alterations. The information related to FEM mesh elements (hydrodynamics) had to be coupled with DEM's (ice dynamics); therefore, a linear interpolation function was applied. The DynaRICE model, and the natural flow behaviour in a specific bend (Yellow River) were used, targeting model validation. Output ice forces on the banks were found to be useful in bank protection configurations. DEMRICE model consumes less computation time, in comparison to the DynaRICE model; although, three-dimensional ice dynamic results can be provided. This model can be implemented to other floating objects (Zhai et al., 2022).

Lu et al. developed a two-dimensional numerical simulation for the ice dynamic and jamming, as well as their effects on the hydropower running at the upper Niagara River. The hydrodynamic (finite-element method) and ice dynamic (smoothed particle hydrodynamics method) were coupled at the water and ice interface, by procedures influencing both ice and water dynamics. The ice dynamic simulation was calibrated based on a specific date for the lake ice run, leading to substantial ice jam formation at the hydropower station intake. At hand field data were water level and discharge at various locations, as well as observed ice conditions based on reported data with 1 to 3 hours of time intervals. The boundary

conditions allocated to this simulation were reported wind velocities and water level, as well as ice discharge in a specific location (Fort Erie), together with water discharge for the downstream boundary. One of the main aims of the study was to expand the knowledge on the effect of wind on the ice movement and jamming process (Lu et al., 1999).

2.1.1 Tension enforced on the ice by wind

Wind is an important influential factor in formation, movement and break up of ice in river and sea. Wu (1968) conducted a laboratory measurement, consisting of wind profile surveys, measurement of drift currents and water surface observations for a large range of wind velocities. The experiments took place in a wind-wave tank. In this study, variety of wind profiles were systematically measured. For these measurements, vertical movement of a pitot-static tube was used. At the same time, the disturbed water surface was recorded, using a prob for measuring wave height and a device for wave slope. This boundary layer survey established a logarithmic distribution and confirms the validity of the constants in the distribution (Wu, 1968). The velocity profile known as Karman-Prandtl velocity distribution is in provided in Eq. 2- 1 and Eq. 2- 2 (Wu, 1973).

$$\frac{u_a}{(u_*)_a} = \frac{1}{\mathrm{K}}\ln\left(\frac{y}{k}\right) + 8.5 \qquad \textit{Eq. 2- 1}$$

$$(u_*)_a = \sqrt{\frac{\tau_0}{\rho_a}} \qquad \textit{Eq. 2- 2}$$

In Eq. 2- 1, u_a is the measured wind velocity at an elevation of y above the mean surface of water. $(u_*)_a$ is shear velocity of the wind, K is Karman universal constant equals to 0.4 and k is the roughness depth of the disturbed water under the wind influence. In Eq. 2- 2, τ_0 is the wind stress on the water surface, ρ_a is the air density. Based on the logarithmic distribution of Eq. 2- 1, wind velocity coefficient (C_y) can be defined by Eq. 2-3 (Wu, 1973).

$$C_y = \frac{\tau_0}{\rho_a {U^2}_y} = \left[\frac{\mathrm{K}}{ln\left(\frac{y}{d}\right)}\right]^2 \qquad \textit{Eq. 2- 3}$$

In Eq. 2-3, U_y represents wind velocity measured at an anemometer height of y, above the mean surface of water. $d = \frac{k}{30}$ and denotes the dynamic roughness of water surface disturbed by wind. Wu (1973) provided the values for wind-stress coefficient between 6×10^{-3} to 2×10^{-2} (Wu, 1973). These studies provide fundamental insight in wind-shear tension in ice-covered regions. Although, for ice covered surfaces lower values are expected. The wind-shear tension in ice-covered regions correlates with wind and ice velocities. Overland (1985) estimated the air drag coefficient on first-year ice in the sea from aircraft measurements. The obtained ranges from observations at a 10 m distance from the sea surface varied with ice roughness and seasonal meteorological condition. Overland (1985) mentioned that in ice modelling, it is important to define an effective wind drag coefficient on sea ice to correlate regional stress and wind since sea ice varies in features at the scales smaller than 20 km. In this work, it was also mentioned that the regional stress is affected by surface roughness, buoyancy flux and external atmospheric conditions, namely inversion height, which is the altitude at which a temperature inversion occurs. Overland (1985) estimated that the air-stress drag coefficient on smooth, flat ice to range from 1.3 to 1.5×10^{-3}, and from 2.5 to 3×10^{-3} for wind velocities above 5 m/s and below-freezing degree temperatures for an almost continuous ice pack. The value of 1.5×10^{-3} for large flat floes in 0° is a subjective median for the wind drag coefficient values related to a series of data sets. These data sets are Beaufort (1957-1958), Arctic (August 1956), Beaufort (1975-1976), Gulf of Bothnia (April-May 1971 and March-April 1977) (Overland, 1985). Guest and Davidson (1991) proposed aerodynamic roughness for different types of sea ice. They suggested a wind drag coefficient of 1.5×10^{-3} for extremely smooth first-year or multiyear sea ice with without pressure ridges (Guest and Davidson, 1991).

Since the fluctuations in the wind stress significantly influenced volume of the sea ice in the Arctic Ocean over the past several decades, Watanabe and Hasumi (2005) investigated timescale of sea ice variation to wind stress using a coupled sea ice-ocean model. To elucidate the time scale of sea ice response to rapid change of wind stress and other controlling mechanisms, their model was forced by two small and large outflows. They found the

timescale of sea ice response and its controlling mechanisms to act differently, based on the decreasing or increasing outflow (Watanabe and Hasumi, 2005). Spreen et al. (2011) examined spatial trends in Arctic sea ice drift speed using SSM/I satellite data and wind force influence from daily wind data, during winter months. The wind speed was 10 m above the surface from atmospheric reanalyses. Their results showed the Arctic Basin sea ice drift speed increases much larger than that of wind, although the wind speed influenced speed drift changes (Spreen et al., 2011). Overland and Pease (1998) developed a sea ice dynamic model for coastal seas with physical length less than 10 km and coupled it to appropriate coastal currents. They examined cases related to the ice, in which the internal ice stress divergence was significant (due to the wind direction irregularities) for modelling nearshore ice behaviour. They considered polynyas, rubble fields and flat first-year ice. They coupled thickness, strength and compactness since low-strength region were in contrast with consolidated ice under compression (Overland and Pease, 1988). Høyland et al. (2021) investigated fatigue damage related to fixed offshore structures prone to drifting ice. They adopted the Copernicus database alongside basic analytical equations to derive large-scale ice statistics, and for the structural scale, they evaluated the results with ice load data from the Norströmsgrund lighthouse. For the fatigue estimations. They combined wind, wave, and ice loads, using simulated analysis of time-series of the various loads. Their results indicated that ice loads are higher than those of winds and waves, while the cumulative frequency of the former is much lower than the latter (Høyland et al., 2021).

Shan et al. (2022) conducted experimental research on the effects of wind shear stress and ice cover, which was simulated using smooth plexiglas, on the water velocity profile distribution. They mentioned that only the wind velocity component along the flow direction can mainly affect the velocity distribution. All their measured velocity distribution corresponded to one of these three patterns; a bowl shaped velocity distribution, a typical boundary layer profile, or an S-shaped velocity distribution (Shan et al., 2022).

Shen et al. (1995) improved ice process formulation (RICEN model) for a channel network in terms of supercooling condition, undercover frazil ice accumulation and transport capacity, including wind effect, etc. The model was used for the ice conditions in the upper Niagra River and the lower Yellow River. For the river hydraulics of this model, the continuity equation (comprising discharge and cross-sectional area) and momentum equation were solved. Shear

tension of the air comprised terms for water and ice, calculated based on the surface ice concentration. Additionally, considering the ice in an equilibrium state, the shear stress on top of the ice assumed to be equal to that between water and moving ice. Furthermore, for the momentum equation, the flow resistance encompassed both underside of ice and bed resistances (Shen et al., 1995). Shen et al. (2000) considered momentum ice run under the internal resistance, gravity, water and wind forces, taking into account the surface ice run as a continuum (Shen et al., 2000). Lal and Shen (1993) attributed the rate of work done by wind on ice in turbulent fluctuations to shear stress of the wind and the water velocity near the surface. They attributed the wind shear stress to wind velocity at 10 m above the water surface and density of air as well as constant wind drag coefficient (1.3×10^3) (Lal and Shen, 1993). Shen et al., used DynaRICE model to simulate dynamic and transport of surface ice in Thames river, considering the wind and current forces and based on a mid-winter breakup in 1986. They considered ice to be broken from upstream and supply the ice to the domain with a concentration range of 0.3-0.35 at the upstream boundary for the model validation. Also, Ice flow thickness of 0.25 m was used as another source of ice supply upstream boundary. This validation was performed by a number of field measured data. Their results showed an ice jam formation was due to the ice congestion following ice floe convergence (Shen et al., 2008).

Wang et al. (1995) performed a model calibration based on the historical data and observations in the Tonawanda Channel of the upper Niagara River and a parametric study on ice jamming processes. This parametric study showed the effect of wind, water level and ice thickness on ice jamming processes in upper Niagra River. Their results showed a threshold of wind velocity for ice jam occurrence since low wind velocities wouldn't lead to adequate ice transport and jamming. Although, the increase in ice discharge rather largen the thickness of the jam than its length. Besides, the wind velocity increase had to rise both the transporting ice volume to the river and the flow, per se. They indicated ice booms as an option for ice jam mitigation (ice discharge control) (Wang et al., 1995). Kolerski et al. (2013) evaluated designed ice boom for water quality protection in Lake Notoro with DynaRICE model. They took into account various scenarios for simulating loads on the ice boom (including wind and tidal loads) to control passing sea ice through lake. Based on the results for different scenarios, they concluded wind can change the maximum load and load distribution on the boom spans

(Kolerski et al., 2013). Shen and Liu (2003) stated the importance of wind is limited to large rivers and wind direction aligned with the rivers (Shen and Liu, 2003).

Carter et al. mentioned the static ice forces may be limited to the environmental driving forces (e.g., thermal expansion, wind) and hydrodynamic forces (e.g., water flow and the flow level changes), or the ice cover ability to transform the forces. These static forces (including wind forces) are able to collapse the cover against a fixed structure (Carter et al., 1998). Su et al. (1997) conducted baseline simulations to develop understanding of flow and ice transport in Grass Islan Pool (GIP). The aim was to find the effectiveness of a number of suggested structural and physical plans for preventing ice jams and resultant power losses. They used non-linear viscous-plastic constitutive law for the relation between internal ice stress and strain rate. It was due to the fact that during the ice jamming and stoppage process, ice jam mainly behaves like a solid object and the stress state acts independent from strain rate. The viscous plastic law estimates the rigid state of a stationary ice mass to a very slow flow state. To this purpose they calibrated the model with an empirical ice parcel stoppage criterion. They conducted simulations both with and without the effect of wind. They noticed existing wind did not extremely change the ice jam volume in the control area and the necessary time for occurring an ice stoppage in an ice escape channel (Su et al., 1997).

2.2 Laboratory experiments of river ice dynamics

For experiments related to ice dynamics, an important factor to consider is whether the experiments are performed in cold temperature or if a substitute material is used to simulate ice. Evers et al. (2002) conducted an indoor experiment related to the pancake ice growth. Their set up was equipped with two wave tanks in a cold room, and the wave generators operated separately from each other in two matching flumes. The aim was to separate dynamics and thermodynamic effects. Apart from experiments with using generated waves, they grew ice in still water in the same cold room with isolating walls and bottom. They collected hourly data related to wave, ice and environmental conditions (Evers et al., 2002). Hopkins et al. compared their DEM simulations with physical models' tests using natural ice. The models were replicated in a refrigerated rectangular flume. The ice boom consisted of seven wooden cylinders and the arrangement allowed for both streamwise and downstream loads on the boom. Uniform freshwater ice sheet was developed in the feed tank. Ice sheets

were broken into angular pieces or floes. One of the main differences between the experiments and the DEM model simulations were the geometry of ice floes. In the simulations the ice floes were cylindrical disks uniformly distributed in size and thickness. In the experiments, however, ice floes were polygonal pieces broken from an ice sheet with varying sizes and a uniform thickness distribution (Hopkins and Tuthill, 2002).

Wang et al. (2016) investigated an experimental study on ice jams around bridge piers with three different diameters. They simulated ice cubes and ice cover using polyethylene and styrofoam due to its similar mass density to ice and represented the piers with plastic cylinders. They observed that the ice jam formation relates to the Froud number, the pier diameter and water discharge. They identified different characteristics of the ice jams before and after the piers and found that the rate of formation downstream was greater than upstream. They observed increased submergence of the ice cubes due to the presence of the piers (Wang et al., 2016). Unduche and Doering (2007) conducted an experimental study on different types of ice runs, varying the parameters of flow depth, velocity, air temperature and bed roughness. They located cameras on the top and side of the experimental set up of a channel in a cold room to capture the images of ice on the surface and at depth. They obtained four different types of ice formations: a skim ice cover, a skim ice run, a complete frazil ice formation, and a skim ice and frazil slush run. The types of ice formation were dependent on the degree of turbulence, related to the changing parameters of the experiments (Unduche and Doering, 2007).

Haynes et al. (1983) performed experiments on the ice forces on the simulated bridge piers, taking into account the variation in velocity of ice sheet and slope as well as the ratio of the width of the structure to the ice thickness. Experiments were conducted by producing ice sheet in refrigerated basins and pushing it towards different structure models. Structural response to the longitudinal and transversal, as well as torsional patterns of vibration were measured by the accelerometers. Results indicated that the inclination of the structure mainly influenced the ultimate requisite force related to the bending failure. Furthermore, by increasing the velocity of ice sheet movement towards the structure the failure changes from bending to crushing; velocity magnetite related to this transformation mode increases with the slope angle starting from vertical direction (Haynes et al., 1983).

Zufelt and Ettema (1996) provided an outline on the properties of substitute materials for ice in physical modelling. It included reviews on the similitude criteria for reproducing the ice processes. They classified ice modelling materials as unbreakable ice sheets, unbreakable ice pieces, ice piece accumulation, and breakable sheets. They stated, at the aim of ice process simulation, which is categorized in hydraulic and ice load modelling, any of these materials can be taken into account. Moreover, they declared, hydraulic modelling entailed unbreakable sheets and ice pieces, while breakable sheets and breakable or unbreakable ice pieces for ice load simulation (Zufelt and Ettema, 1996).

Crissman et al. (1995) performed a study on the design enhancement on the design of ice boom located in Erie-Niagara Lake. The aim was to replace the timbers of the ice boom with steel pipe pontoons, in a 30-year duration of investigation attributed to the ice boom function. The performance assessment of the existing and several alternative configurations of the ice boom related to the various historical ice runs with the implementation of the coupled ice-hydrodynamic numerical simulation for the overtopping ice (transported ice over the boom) was carried out. The simulation results showed, the cost effectivity of the design improvement. The line load on the boom was calculated according to the tension measurements. For the ice load calculation, they considered the forces related to the wind set up and wind waves to be neglected, due to the difficulty in the analysis. Considering the free floating feature for the boom, the forces were narrowed down to horizontal ones (Crissman et al., 1995).

Sodhi (1996), put up a physical model at the shape of an inclined riprap embankment, aiming to collecting data on the damages to riprapped banks affected by ice shoving. The scale of the physical model was chosen based on the typical flexural strength of the ice. The ice was shoved by pushing the riprap model towards the ice sheets. The slope of the riprap and size, as well as mix of the covering rocks of the embankment were changed for different sets of experiments. Moreover, the horizontal and vertical ice loads on the structure were calculated by means of load sensors. The experimental results indicated that ice sheet buckled numerous times during each test. Additionally, shallow-slope banks showed minuscule or no damage, following the ice ride up. It was also noticed that the most sever damages were observed at or below the water surface level (Sodhi, 1996).

Essel et al. (2021) conducted a 3D numerical and 2D experimental study on the influence of partial ice covers, with varying rates of flow surface coverage, on turbulence and secondary currents. The PIV technique was used for the experiments in a recirculating open flow channel. They simulated ice covers with glossy see-through acrylic plates, installed symmetrically adjacent to both sidewalls of the channel, using hanging rods. The water level was maintained at the same height despite a slight increase caused by the ice covers. The results of the PIV technique were used to evaluate the predictivity of five RANS-based turbulence models. The experimental results indicated that the mean velocity in the direction of the flow and the Reynolds normal stresses increased at the central cross-sectional plane of the channel in the presence of the ice covers. They observed the mingling of the core secondary current with the side current, forming a convergence between the area beneath the ice-covered surface and open water, driven by a single driving force (Essel et al., 2021).

2.2.1 Particle Image Velocimetry (PIV technique)

Image based velocimetry is a non-invasive technique which is able to provide continuous flow field as opposed to point-based results (Lin et al., 2019). Imaged-based velocimetry technique is divided into two groups of Particle Image Velocimetry (PIV) and Particle Tracking Velocimetry (PTV). The former is an Eulerian methodology which estimates velocities at image subregions, while the latter is a Lagrangian approach that calculates the velocities in a view field based on the detected particle movements (Lin et al., 2019). Particle Image Velocimetry (PIV) is a state-of-the-art technique and non-intrusive approach to measure the instantaneous fluid velocity fields. These velocity fields can be produced by this technique, if seeding material reflect the flow field. The velocity field needs to be traced with the seeding material and to be illuminated with a laser sheet. By each two pulsing of the laser at a regular interval, the succeeding position of the particles can be recorded.

Paprota (2020) performed numerical and experimental study related to an interaction of two independent waves and its effect on mass transport. For the experimental study, PIV technique was used for calculating the wave velocity field. Numerical and experimental results showed good resemblance for mass transport and particle trajectories (Paprota, 2020). The selection of a seeding material for the air section of the PIV measurement can be more challenging, in comparison to the water field. Let alone, the air field is under the

influence of wind. PIV measurement is also able to produce solid results in two-phased flows, e.g., air-bubbled water flows, with bubbles as the seeding material (Paprota, 2017). In air-bubbled flows air is soluble in water. Therefore, it may come to mind, wind flow may be treated as a two-phased flow, if a liquid is introduced as the seeding material in this gas field (wind). Hardalupas et al., described an optical instrument for droplet size and velocity, as well as gas field. They used PIV technique for the gas phase velocity calculation. The droplet and gas were taken as two phases, and gas phase were seeded with aluminium oxide particles separately. They successfully could distinguish between droplet and seeding particle centres (Hardalupas et al., 2010). Although, considering two phases is not concerning this study. It still can be suggested for future studies.

A seeding material for the PIV measurement in the wind field needs to be chosen, in a way to satisfy both wind velocity field measurement and experimental set up condition, e.g., the place for installing the required devices. There are related studies to PIV measurement; each of which dedicates to various PIV measured fields. In the studies considering different fields to be measured with PIV technique, for each section separate type of seeding material is needed. Techet and McDonald (2005) used a high-speed PIV measurement on breaking waves to be forced to a steep surface, therefore varying surface level was considered. A high-speed digital video camera for capturing 500 frames per second was used to get quantitative data from water and airfield. A diode line sheet generator laser was used to produce line sheet. To reflect the air and water field, water-based fog and hollow glass spheres were used, respectively. The air field was not under the wind influence; therefore, no wind was affecting the water field. They found difficulties in achieving uniform seeding with fog for the air field, to obtain satisfactory resolution for PIV measurement. Although, their vorticity results well agreed with a previous study on both air and water side (Techet and McDonald, 2005). Zhang et al., used PIV technique for velocity measurement of the wind field with olive oil seeding particles, in a wind-blown sand field. They noticed a significant influence of wind-blown sand on the wind velocity field. They had to consider a specific freestream wind speed at a lower magnitude to achieve sufficient concentration of seeding particle material and sand for measuring velocity fields of wind and wind-blown sand. The olive oil particles were mainly distributed in the lower half height of the wind field, which was of a more importance for the measurement. Geometric mask which can be applied in PIV measurement to increase the

measurement accuracy was used to block sand particles from wind velocity field. Their result showed the deviation of the mean flow from so called log-profile. Also, increased turbulent intensities was observed in the higher concentration of the sand particles (Zhang et al., 2008).

It can be noticed that the particles with higher density which are blown in the air are more probable to affect the velocity of the wind field; seeding particles in the wind field may act as such. This is a consideration that can be taken into account for identifying seeding materials. It should be noticed that seeding particle materials need to be large enough to scatter the laser light and small enough to properly track the flow velocity field (Melling, 1997). Troitskaya et al. (2011) visualized turbulent air flow above mechanically produced gravity waves by micron-sized illuminative particles (almost spherical polyamide particles) (Troitskaya et al., 2011). Apart from size of the seeding particle material, its choosing appeals specific concern to be chemically inactive, non-abrasive, enduring (steady and being constantly supplied), and non-poisonous (Melling, 1997). fulfilling these characteristics, different materials can be suggested, which can be found in Melling (1997), for both liquid and gas fields. Furthermore, in application of PIV system in a river, degradable materials with insignificant portions related to river flux are suggested to not harm the river environment, e.g. well-distributed natural foam on the river surface (Creutin et al., 2003; Jodeau et al., 2008). In the gas fields, both solid particles and liquid droplets can be looked into, as seeding material options. Although, liquid particles are able to produce steadier seeding production rate (Melling, 1997). Based on the mentioned characteristics for seeding particles, and the mentioned advantage of the liquid type of seeding particles in gas fields, the question would be whether it is possible to seed water particles in the wind velocity field for PIV technique. PIV measurement technique has been used for fire safety related studies on water mist released from high pressure nozzles (Husted et al., 2009). In Husted et al, (2009), the pressure imposed on the water mist released through nozzles was considered.

2.2.2 Particle Tracking Velocimetry (PTV technique)

Cold region engineering needs information about cross sectional or the full field velocity distribution and ice movement rates (Ettema et al., 1997). These information come in handy for mitigation of the ice related issues and to discover relationships between water velocities and ice movement as well as wind, e.g., probability of ice jamming and assessing ice loads on

the structures and shorelines (Ettema et al., 1997). The establishment of image-based techniques has advanced the identification of water bodies (Tauro and Grimaldi, 2017). Both PIV and PTV are the most popular conventional image processing methods for measuring the flow fields (Fujita et al., 1998). Choosing the proper algorithm is based on the tracer concentration in the flow field. PIV technique is suggested when a group of particles or other quantities related to the flow form a pattern in successive images. In the case of low tracer concentration, it is useful to measure the displacement of individual particles (Fujita et al., 1998). This low image density algorithm is referred to as Particle Tracking Velocimetry (Fujita et al., 1998). PTV first, needs to spot the possible tracer particles, and then find the trajectory of the particles. Compared to PIV, it is more suitable for changing environmental conditions (Lin et al., 2019).

Tauro and Grimaldi (2017) used ice dices as thermal traces to sense distributed environmental flows and characterize the flow kinematics as a result of thermal signals to a portable camera with an axis perpendicular to the stream surface. The sufficient visibility and low concentration of the tracer particles allowed for implication PTV technique. They considered the eco-friendly easily propagated behaviour of ice dices as an advantage to be used as tracer particles. They videotaped the particle movements and extracted related images, with displaying ice dices as white tracers on a black background. They used PTVlab software to analyse the sequence of images and obtained flow velocity field maps. The found out the PTV results were in close comparison with a standard current flow meter (Tauro and Grimaldi, 2017). Dal Sasso et al. (2020) compared PTV and large-scale PIV techniques in terms of accuracy for different seeding conditions and case studies for calculating surface velocity. They noticed both techniques are sensitive to variation of dimension and dispersion of the seeding particles as well as seeding density for the image velocimetry. They mentioned environmental noises, e.g., shadows and illumination can negatively affect the seeding particles quantification. Furthermore, low seeding material resulted in incomplete flow filed. They also suggested to increase the duration of the videotapes to reduce error and find optimal frame windows (Dal Sasso et al., 2020). Tauro and Salvatori (2017) Analysed videos through PTV technique to estimate river surface velocities in comparison to radar data. The noticed PTV was not possible to be applied for videos related to night hours. They found a right angle for the optical sensor dedicated to captured videos for the most accurate velocity

results. Also, fish eye lens led to less accurate velocity results and intensely affected by illumination. They concluded PTV can be successful in low flow velocities (Tauro and Salvatori, 2017).

Wang and Wei (2015) described a virtual 3D-PTV verification. It was considered for assessing the accuracy of the PTV algorithm and simulating the experimental set up. They showed the possibility of producing virtual particle images and capturing the movement either by the user or the FLUENT Software. The illumination and shape variation of the visual particles were considered. The particle images were compared the results with PTVlab software. The results showed that the virtual particles could be generated and tracked as the real images from PTV cameras (Wang and Wei, 2015). Patalano et al. (2017) described PIVeR which is a practical toolbox for large-scale PIV and PTV methods and can be used as an add-on to the existing image processing tool boxes e.g., PIVlab and PTV lab. They considered PIVeR as an already operational and successful toolbox. They mentioned LSPIV and LSPTV are beneficial for both high-flow events e.g., flashfloods and low-flow events as well as synoptic water characterization e.g., flow over hydraulic structures (Patalano et al., 2017a).

2.3 Mathematical modelling

Modelling ice involved situations which comprise numerous existing processes, leaving them a complex combination for studying and modelling (Wolski et al., 2017). This convolution is observed in simple hydraulic phenomenon, e.g., single-phase flow, as it happens. Practically, to initiate the modelling, the dominant processes and attributed forces are required to be recognized (Zufelt and Ettema, 1996). The surface ice run is in the control of wind and water drag, as well as gravity force. The ice run is also under the influence of binary interaction between ice and hydraulic structures (Shen et al., 2000). Furthermore, surface ice run includes varying shapes and sizes of the particles, which is possible, yet impractical (due to the large amount of pieces) to be considered in the surface ice transport and the interaction of the particles; in the natural rivers, the surface ice can be considered as a continuum, due to the larger scale of the river channel to the particles' sizes (Shen et al., 1990).

Since the border ice formation influences the emergence and progression of the ice cover, Huang et al. (2012) reviewed and unified a set of formulation related to these phenomena.

This formulation was implemented to a two-dimensional thermal-dynamic model, being validated with the field data from the upper St. Lawrence River (Huang et al., 2012).

Liu and Shen (2000) developed a two-dimensional model for the ice transport simulation. In the model, the surface ice dynamic and the flow hydrodynamic were coupled. For the simulation of ice dynamics, smoothed particle hydrodynamics with Lagrangian discrete-parcel method, and for solving hydrodynamic equations, the Finite-element method was applied. Ice entering behind the booms, underside erosion of the ice accumulation and its leading edge, etc. were considered (Liu and Shen, 2000).

Zhai et al. (2022) developed a numerical model for the dynamics of river ice (DEMRICE), by means of the discrete element method. The aim was simulating ice jams (considering seepage flow through the ice), and ice floe movement under the influence of hydraulic variable alterations. The information related to FEM mesh elements (hydrodynamics) had to be coupled with DEM's (ice dynamics); therefore, a linear interpolation function was applied. The DynaRICE model, and the natural flow behaviour in a specific bend (Yellow River) were used, targeting model validation. Output ice forces on the banks were found to be useful in bank protection configurations. DEMRICE model consumes less computation time, in comparison to the DynaRICE model; although, three-dimensional ice dynamic results can be provided. This model can be implemented to other floating objects (Zhai et al., 2022).

Lu et al. developed a two-dimensional numerical simulation for the ice dynamic and jamming, as well as their effects on the hydropower running at the upper Niagara River. The hydrodynamic (finite-element method) and ice dynamic (smoothed particle hydrodynamics method) were coupled at the water and ice interface, by procedures influencing both ice and water dynamics. The ice dynamic simulation was calibrated based on a specific date for the lake ice run, leading to substantial ice jam formation at the hydropower station intake. At hand field data were water level and discharge at various locations, as well as observed ice conditions based on reported data with 1 to 3 hours of time intervals. The boundary conditions allocated to this simulation were reported wind velocities and water level, as well as ice discharge in a specific location (Fort Erie), together with water discharge for the downstream boundary. One of the main aims of the study was to expand the knowledge on the effect of wind on the ice movement and jamming process (Lu et al., 1999).

Lal and Shen (1993) developed a one-dimensional river ice numerical simulation, by the name of RICE. The model was made up of submodels attributed to the river hydraulics, ice cover formation, distributions related to the ice discharge and water temperature, emergence and erosion of under-cover accumulation of ice, stability of the ice covers, and thermal expansion and deterioration of ice cover. The theories on the ice processes were reviewed, recognizing the weak points. Due to the fact that, each ice processes were coded in separate subroutines, the modifications succeeding new theories could be accommodated in the model. This model can be implemented to identify the prominent controlling parameters for the ice condition related to a river, that allows providing guidelines for systematic data, flow regulation arrangement, and designing of ice control operations (Lal and Shen, 1993). This model which included two layers of surface ice and suspended ice flow was modified to be used in an entire river. The model would consistently consider both ice covered and open water reaches. The model was applied to upper St. Lawrence River and it provided desirable results (Shen et al., 1990).

Hammar and Shen progressed a mathematical model for the frazil ice evolution in a turbulent channel, by means of implementing frazil dispersal and temperature variation, as well as increase in the particle size (Hammar and Shen, 1995). The model was validated by existing laboratory data, examining the surface heat rate, seeding rate, secondary nucleation, and flow condition. The importance of seeding rate quantification, and the relationship between collision energy and secondary nucleation rate was indicated. The simulation illustrated the involved processes for the frazil evolution in turbulent flow. Also, turbulence features were considered as important in frazil evolution procedure, due to the dominating temperature, particle distribution and collision frequencies (Hammar and Shen, 1995).

Then CRISSP model was developed on the basis of two advanced RICE and DynaRICE simulations, with their enrichments. The last version of RICE model in use, was prevailing for the ice simulation. The model was implemented for studying ice conditions in the Ohio, Upper St. Lawrence, Niagara, Peace and Yellow Rivers, to prepare a good background for CRISSP-1D progression. The improvements consisted of adding internal boundary condition for modelling hydraulic structures, unsteady flow modelling improvements, generalization ice modelling to the river networks, introducing transverse flow distribution, etc (Shen, 2002).

CRISSP, Comprehensive River Ice simulation system project was progressed in 2000 (Wazney et al., 2019). The aim of this modelling was the engineering needs in hydropower system, inland navigation system, boom designing, ice jam related flooding, water transport, environmental and ecological issues associated to the ice, etc. across the United States and Canada (Shen, 2002). The model is validated by means of field conditions and successfully being applied on variety of studies attributed to the ice-period operation and ice control; including, Niagara hydropower project, ice jam in Missouri-Mississippi River, ice jam breakup in Shokotsu River, etc (Shen, 2005). CRISSP2D has been developed based upon the two state-of-the -art RICE and DynaRICE models: 1D and 2D, respectively. (Shen, 2002). CRISSP2D is expanded based on the thermal modules and ice dynamics simulation features of these models. The hydrodynamic and ice dynamics modules are coupled at specific time intervals specified by user for transfer of information (Shen, 2005). A one-dimensional model is not sufficient for river ice processes and problems related to the engineering and hydropower station projects. Based on the complexity in river geometry and flow pattern condition, a more detailed two-dimensional analysis is required, as such. Having said that, DynaRICE model is the only provided two-dimensional ice model (Shen, 2005).

Wazney et al. (2019) implemented a new formula in Crissp-2D simulation, related to the growth in ice crust during the ice cover formation, and the resistance increase. The crust was permitted to grow, based on the critical velocity, specifying the compressive strength by the user. The model could be used to simulate the ice cover failure and resulting consolidation on the occasions of the thermal strengthening rate surpassing that of increased forces. The new formulation enhanced the applicability of the model for processing of physical simulation during the freeze up, and its implementation on physical scenarios (Wazney et al., 2019).

One dimensional RIVICE model, developed by Environment Canada, is a hydrodynamic model that simulates the majority of ice processes and phenomena in rivers. The solver applies an infinitive finite-difference scheme, and ensures that the ice formation and development are decoupled from the hydraulic processes if calculations are performed frequently and proper time steps and length are applied, based on the situation at hand (Lindenschmidt and Sereda, 2014). There are still other models which simulate equilibrium ice jam in steady state condition, e.g., ICEJAM, MIKE-11, RIVER1D, HECRAS, etc (Carson et al., 2011).

3 Methodology

In this section, the physical modelling and numerical simulations with the DynaRICE model are described. The section includes description of the different experiments, the experimental set up, ice velocity measurements using PTV technique, and the experimental results used as input for the numerical simulations. One parameter considered in ice simulation is size of the ice, which is introduced in smaller and bigger sizes as ice pieces and cover. An ice cover may both form and breakup, due to the different thermal and mechanical effects in a river (Ashton, 1986). Ice pieces which are usually in smaller sizes compared to the ice covers, may already be existing due the thermal effects or/and emerge following the breakup of an ice cover. This thermal effect notion is just to be said at an aim of brief description of the ice piece and cover. Although, the thermal parameters are not of any concern of this study. The use of ice pieces and covers for this study is at the aim of considering the sizes of the ice pieces. For the ice pieces the concentration of ice is a considered parameter in this study.

Additionally, this section provides a description of wind velocity measurement using PIV technique and the selection of seeding material for the PIV technique. The measured wind velocities were used as the input for the numerical simulation. In the section related to the numerical simulations, the description of different runs is provided, including the process of achieving the desired ice concentrations.

3.1 Description of the laboratory simulation and physical modelling

The experiments were conducted in a wave flume and in two dimensions. The main assumption of this study is that there is no water movement, nevertheless, water moved under the effect of wind. For this study, the water velocity was measured under the influence of different wind fields. Although marginal water velocity values were obtained. Two sizes of ice pieces were considered for this study; the former considered as small ice pieces and the latter ice cover. The main assumption related to the ice pieces is that they are under the free drift after breakup condition. Additionally, ice pieces are not thermally produced; they are broken pieces with no relation to thermal condition. Therefore, no pancake ice, frazil and underneath jamming, ice accumulation, skim ice run, etc. are of concern of this study. For the wind and water velocity measurement non-intrusive technique of the PIV measurement was used. Three different wind fields were considered for the study as low medium and high

velocities. Water particles were used as the seeding material for the PIV measurement. A sufficient attempt was made for providing stable wind fields.

3.1.1 Experimental set up

Experiments were performed at the wave flume of the Institute of Hydro-Engineering of Polish Academy of Sciences (IBW PAS). The flume was 64.1 m long and 0.6 m wide, as well as 1.4 m high. The aim of the experiments was to investigate the effect of wind on the ice movement that can be defined by the Eq. 3-3. Therefore, different experiments with variety of wind velocities were conducted to consider their impact on ice velocity. In Figure 3- 1, a picture of the flume is presented.

This laboratory where the experiments are conducted, is mainly equipped with a wave flume and it was not previously designed for experiments related to wind measurements. Therefore, extra preparation was made to provide a wind flume. This preparation included designing and installing a ceiling above the water flow and a wind generator with the aim of blowing wind above the water.

The problem with designing the wind flume was that the elevated wave flume needed to be accessible from the top to the middle. Therefore, the ceiling had to be hung from the top of the wave flume with steel bars and installed inside the flume. In Figure 3- 1, the location of the ceiling is illustrated. Another issue that could arise is the splash of water particles on the plexiglass section. This could tarnish the transparency needed for laser light transfer in PIV measurement and disturb the camera view in PTV measurement. Therefore, care had to be taken during the experiments to keep the plexiglass section of the ceiling clean. The same care had to be taken for the measurement window of the wind flume which was supposed to be the view of PIV camera for wind velocity measurement. In Figure 3- 2, the ceiling which is hung by the steel bars and a laser device on top of the wind flume as well as the top view of the wind flume are shown.

Figure 3- 1. The location of the ceiling and its distance from the top of the wave flume.

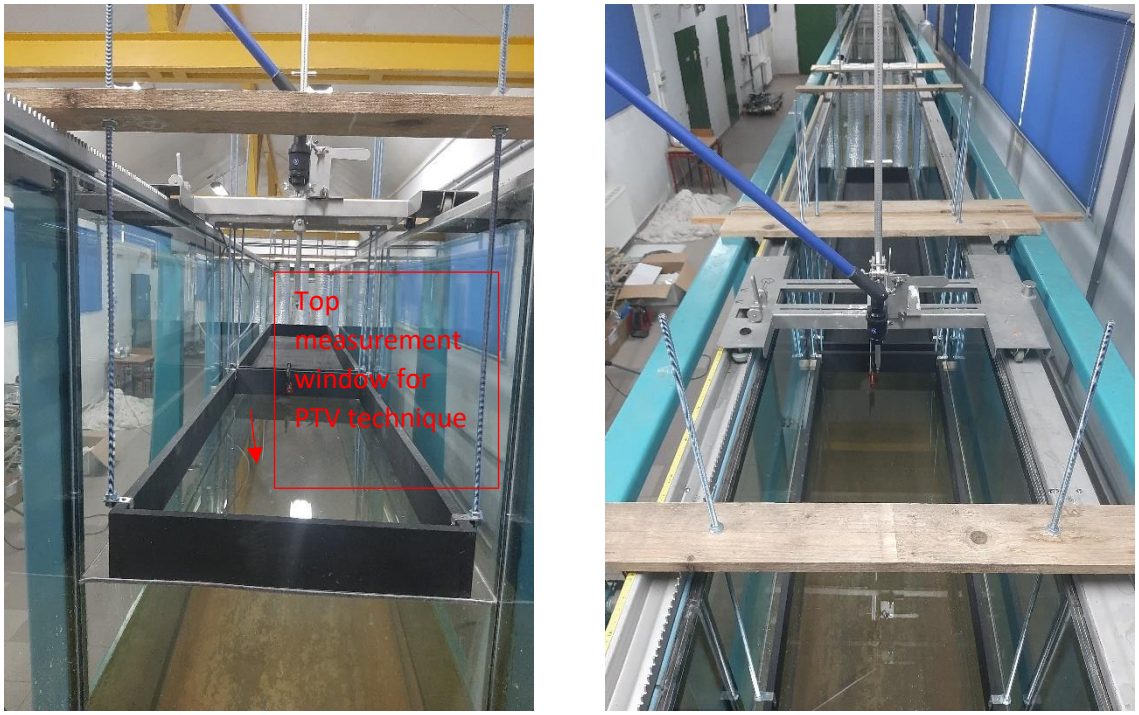

(a) (b)

Figure 3- 2. A view of hanged ceiling with the bars (a) and the laser device on top of the plexiglass section of the ceiling (b), showing a view of the wind flume from the top and the top measurement window.

The wind generator consisting of three fans was located on top of the flume. To prevent air leakage from a narrow gap between the ceiling edges and the flume walls, and to avoid cracking the flume walls, isolation tape was used. The generated wind by each fan travelled to the wind flume inlet through a connecting tube. The other ends of the tubes were fixed at the flume inlet by hangers. Three wind fields were generated by one, two and three working fans. In Figure 3- 3, the installed ceiling and the location of the wind generator can be seen.

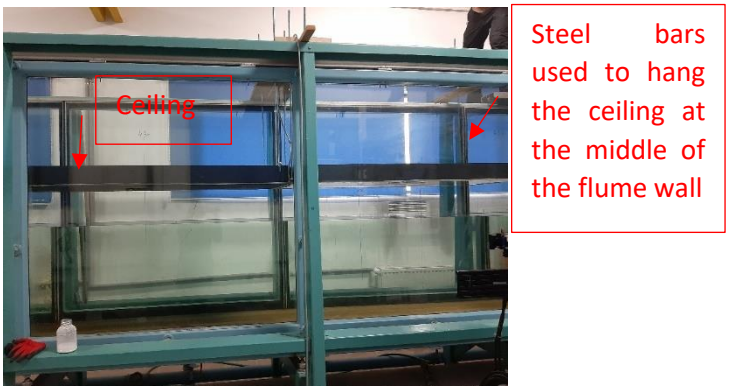

(a)

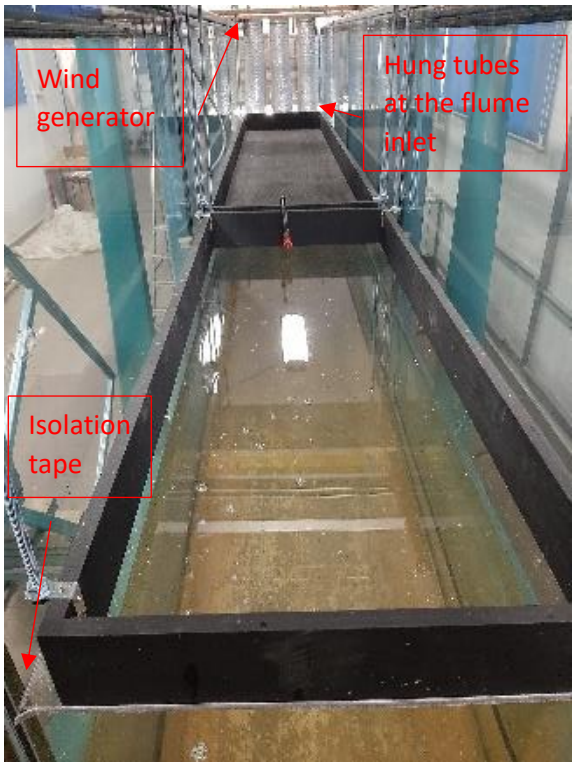

(b)

Figure 3- 3. A part of the flume including experimental set up (a), installed ceiling inside the flume to isolate the wind above the water surface (b).

As mentioned before, to isolate the wind generation above the water surface, a ceiling was installed (wind flume height was 20 cm). The top measurement window for PTV technique was made of plexiglass (1.4 m long), to make ice pieces movements visible from the upper section, and also to transfer the laser light (in PIV measurement) through the plexiglass. While the part of the ceiling closer to the wind generator was made of wood (2.5 m long). The wind generator was installed at the upstream of the channel. Three different wind velocity fields by turning on one, two, and three fans, were generated. In Figure 3- 4, the configuration of the wind generator and its installation inside the flume are illustrated.

(a) (b)

Figure 3- 4. Set up for the wind generator (a), the installation of the wind generators on top of the flume.

Zero water discharge (stationary water) was applied for all the experiments, although, the water velocity under the influence of wind velocity was measured. To perform experiments in the room temperature, ice was simulated from polypropylene cut in rectangular shape. The ice pieces of 10×10 cm size with the thickness of 1 cm were considered. For the cover movement, 4 pieces of polypropylene with the lengths of edges of 50×40 cm, and the thickness of 1 cm were taken into account. To carry out the measurements for the ice pieces movements, the particle track velocimetry (PTV) was applied. This method tracks the route of individual particles which in this method are the ice pieces. Based on this approach, the velocity of the pieces is to be calculated as a function of their displacement in specific timing, from the recorded videos during an experiment. The videos are captured from the top of the flume parallel to the top measurement window (plexiglass section). In Figure 3- 5, a picture showing the ice pieces under the effect of wind is provided.

Figure 3- 5. Ice pieces under the wind effect.

3.1.2 Particle image velocimetry description

To carry out the measurement of the wind velocity and two-dimensional water velocity field, PIV technique was used. The method requires a computer to collect snapshots and a software to analyse the series of pictures (Ettema et al., 1997). The measurements of these velocity fields were performed by a Flow Master PIV system. It included a CCD camera, with a resolution of 1280×1024 pixels, and a 50 mJ dual laser-head system (repetition of 50 Hz). The seeding materials for water and wind velocity were used to reflect the velocity field under the light of pulsing laser. Their reflection was recorded by a pair of two single-exposure images. The exposures to the camera for recording the reflections were set at time intervals of 0.0018. Based on this time intervals between capturing the images and the displacement of the seeding particles, the velocity vectors were defined in so called “interrogation windows” (selected subareas). The velocity measurement was calibrated and performed in a plane parallel to the flow direction (Biegowski et al., 2020). In Figure 3- 6, illuminated wind fields and water particles as seeding material are illustrated. The difference between Figure 3- 6 (a) and Figure 3- 6 (b) is the number of working fans which relate to the one and three fans, accordingly. For the three working fans, more seeding particles are carried out with the

blowing of wind, therefore a consolidated seeded field is observed. In Figure 3- 7, an illuminated water field under the laser pulse is shown.

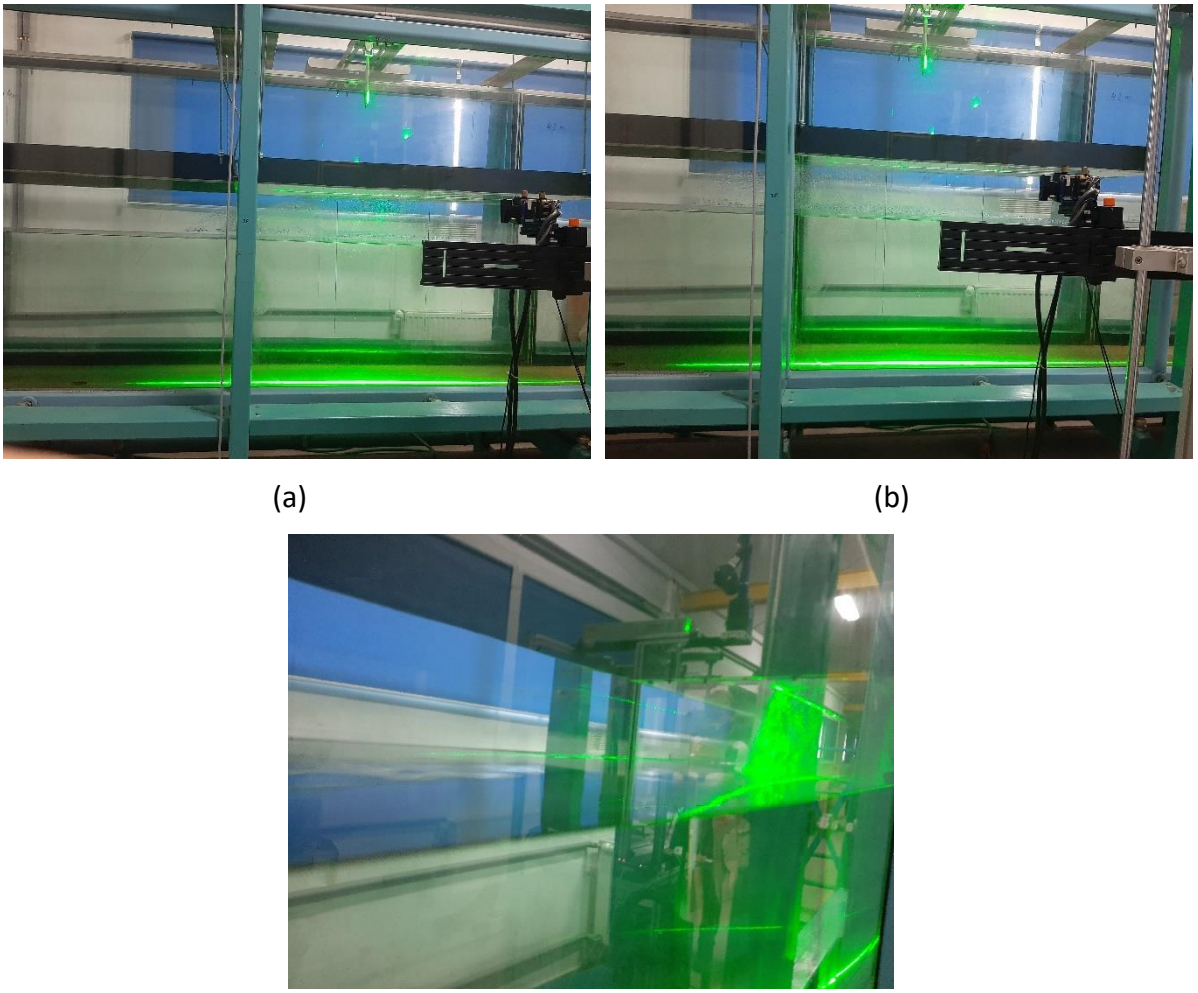

(a) (b)

(c)

Figure 3- 6. The illuminated wind field by the laser light for one (a) and three working fans (b) as well as a side view of the laser sheet (c).

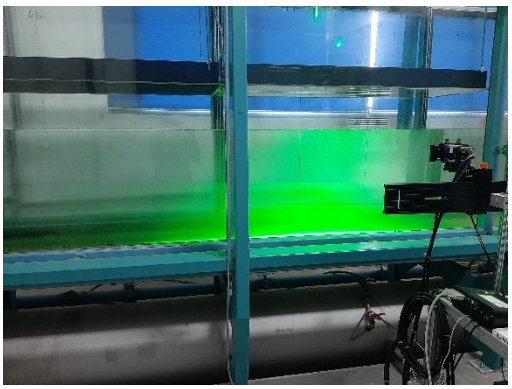

Figure 3- 7. Illuminated water field under laser pulse.

To make the water velocity field reflect by the laser light in front of the camera, hollow glass particles were used as the seeding materials. To make wind velocity field reflecting, there were different choices that are descripted in a further section. The water particles were taken in use and found out to be effective. Therefore, a section to accommodate spray nozzles was added to the experimental set up. Figure 3- 8 shows the laser light on the water mist from a single spray nozzle, which was captured in the laboratory.

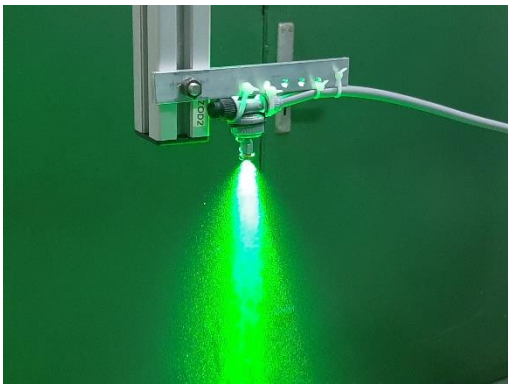

Figure 3- 8. Illumination of the water mist under the laser light.

3.1.3 Description of the experiments related to the wind velocity on ice

Three wind velocity fields were considered for the study identifying low, medium, and high wind velocities. The measurement of the wind velocity was performed above the stationary surface of non-flowing water. The water velocity was measured to determine the effect of the wind drag. For the measurement of both water and wind velocity fields, the Particle Image Velocimetry (PIV) technique was used. The seeding particles must have been used in both wind and water fields to ensure they reflect in the field of view of the PIV camera. The water particles were used for seeding the wind fields, and hollow glass spheres for the water fields.

In Figure 3- 9, a schematic view of the related experimental setup in the laboratory is provided. A perspective view of the channel displays the most important pieces of equipment: measurement window (the utilized section for the PIV measurement), fans, laser device, camera and the calibration plate.

Low, medium and high wind velocities (three velocity fields) were adjusted, with turning on one, two, and three fans, respectively.

The measuring section of the flume was covered with a ceiling consisting of wooden and plexiglass parts with the lengths of 2.5 and 1.4 m, respectively, and these parts are depicted in Figure 3- 9. The plexiglass cover creates a transparent section for transmitting laser light and forming a top measurement window for use in the PTV technique. It can be said that the PIV technique was followed by the measurement of ice movement using the PTV technique from the transparent section. The noted measurement window in Figure 3- 9, refers to that of the PIV technique. An anemometer device (MiniWater20 Micro by Omni Instruments) with a cylindrical shape and a 0.011 m propeller diameter was used to verify the wind measurement with the PIV technique (Figure 3- 10). After the PIV measurement was performed for measuring both wind and water velocity fields, the PIV measurement was verified by using the anemometer device. An opening was created in the plexiglass cover for the intrusion of the anemometer device to the flume. The anemometer device was placed in the wind field to measure the wind velocity. In Figure 3- 10, the crossing of the anemometer device rod through the flume ceiling is shown. The wind velocity profiles for the three velocity fields were recorded by moving the anemometer rod along the height of the wind fields. All of the devices used in the experimental set up are presented in Figure 3- 9 as schematic objects, although they were not utilized simultaneously. Adrian and Westerweel, (2011) mentioned, for the PIV measurement and related seeding particle provision in the gas fields, regular injection of the seeding material is needed. Also, to obtain uniform concentration of the seeding particles in the gas fields, a boost in lateral dispersion by stirring devices, e.g., fans, can be performed (Adrian and Westerweel, 2011). In this study, spray nozzles were used to provide uniform seeding particles in the wind field. Existing fans in the experimental setup could enhance the lateral dispersion of the water particles in the wind field.

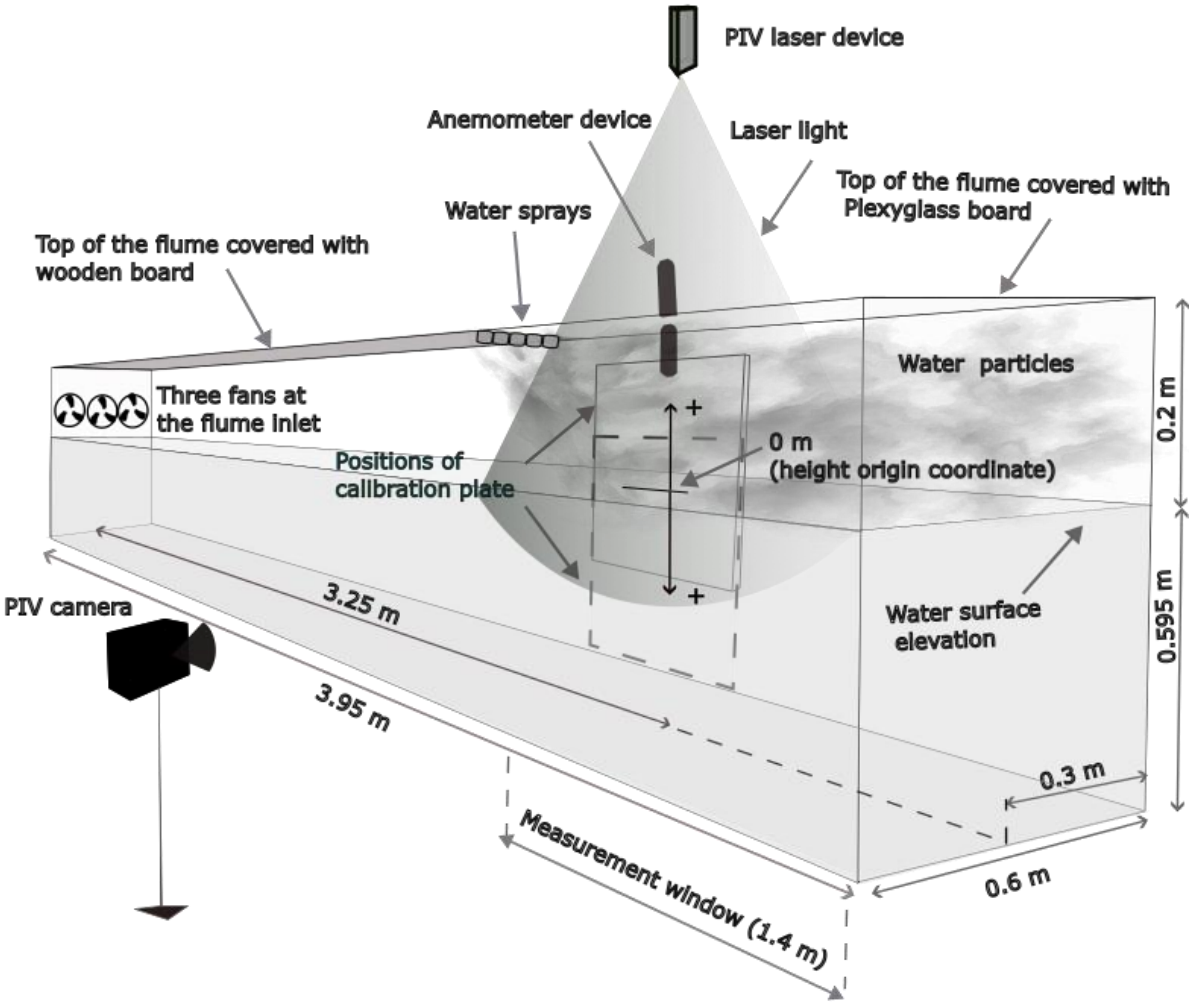

Figure 3- 9. Schematic view of the experimental set up for wind and water fields (out of scale).

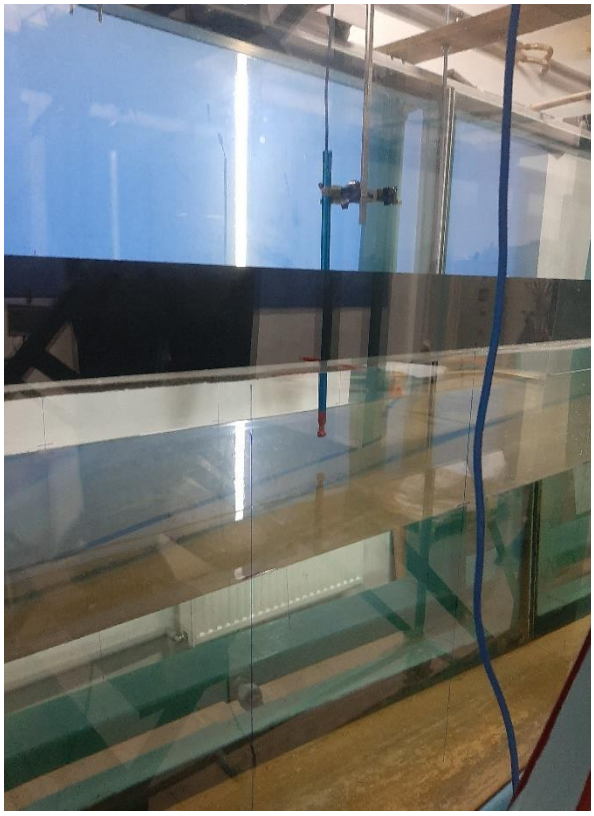

(a)

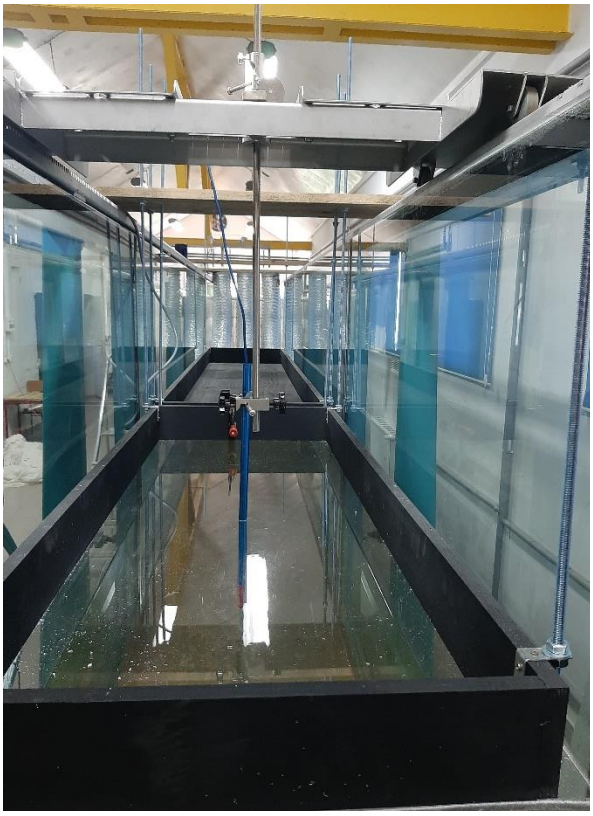

(b)

(c)

Figure 3- 10. The placement of the anemometer device rod in the wind field (a) and (b) as well as a picture from the anemometer device (c).

The experiments and related parameters for describing each experiment are provided in the Table 3- 1. The number of working fans for each wind field generation is given. Additionally, the relation of the experiments to wind or water field is identified. Furthermore, the applied devices, number of repeating experiments and time duration for performing the experiments are provided. Based on the table, the order of performing the experiments can be understood. The first experiment is related to the PIV measurement on water particles from one spray nozzle; the aim of this experiment is to capture velocity of sprayed water. Then the next three experiments (2^{nd} to 4^{th}) were dedicated to the wind fields from low to high wind velocities. For these experiments water particles were used for seeding the wind field. The

next three experiments (5th to 7th) were contributed to water velocity measurements with hollow spherical glass as the seeding material. Experiments 8th to 10th were dedicated to the verification of PIV technique results of the wind velocity measurements for different wind fields. These three experiments were conducted by utilizing the anemometer device.

Table 3- 1. Experiment numbers and descriptions.

Number	Wind field	Water field	PIV	anemometer	fans			Repetition	time (s)
					1	2	3		
1			✓					6	15
2	✓		✓		✓			9	15
3	✓		✓			✓		9	15
4	✓		✓				✓	9	15
5		✓	✓		✓			4	15
6		✓	✓			✓		4	15
7		✓	✓				✓	4	15
8	✓			✓	✓			3	90
9	✓			✓		✓		3	90
10	✓			✓			✓	3	90

For setting the calibration plate for the PIV measurement, each measurement section for PIV technique in the measurement field is an object plane. The imaging system can be considered as a thin lens. The relation between the position of the object and the image plane is known as image mapping. At each distance from the lens of the camera (that an object plane forms), there is a respective image plane at that specific image distance. The lens of the camera maps each point from the object plane to the image plane. So that the object plane collides with the laser sheet, its location needs to be set. To this aim, the image plane, or the image plane together with the focal length can be moved. The image mapping was performed by adjusting a plate which contains a regular grid of markers (Adrian and Westerweel, 2011). This process

was done for the wind and water fields, as well as velocity measurement of the water particles. A black plate covered with metal points (markers) was used for this study. These points need to be adjusted in the paired software (DAVIS) with the camera. The metal points should cover the view field of the camera; therefore, the plate should be large enough to fully cover it. This process ensures the origin and orientation of the enclosed plane related to the measurement field (object plane), and counteract the effect of windows, imaging optics distortions, etc. (Adrian and Westerweel, 2011). In Figure 3- 11, the calibration plate locations in front of the PIV camera for the wind and water velocity measurements are shown. It should be noted that the ceiling of the wind flume is removed momentarily to install the plate and calibrate the camera view. Once, the installation of the plate was done, the ceiling is put back to the place to ensure the provision of wind field for the experiments.

(a) (b)

Figure 3- 11. The levelled and installed PIV calibration plate for wind (a) and water (b) velocity field measurements.

At the beginning of the calibration process, it was needed to ensure that the calibration plate was levelled horizontally and vertically, in front of the camera. This is the basic level, known as coarse calibration of the image mapping. Additionally, it was needed to be ensured that x and y-axes of the calibration plate and those of the image plane lie in a common plane (Adrian and Westerweel, 2011). More information related to the image mapping can be found in Adrian and Westerweel (2011). In Figure 3- 12, the used calibration plate and the attributed x and y-axes are provided. In this figure a PIV measurement set up for velocity measurement of the water particles right after spraying is depicted. This experiment refers to the experiment

number 1 in Table 3- 1. This experiment was performed to find the velocities of the water particles without the effect of wind. The aim was to find the velocities of water particles using the PIV technique, and to compare them with the velocity of water particles coming out of a nozzle, right at the nozzle outlet. The velocity of water particles existing directly out of a nozzle was obtained from the water discharge. The discharge for the water particles in this experiment and all the PIV technique measurements in this study were 1.6×10^{-6} m^3/s for each spray nozzle (which was calculated by classic volumetric method). The velocity of water particles existing directly from a nozzle was 1.25 m/s.

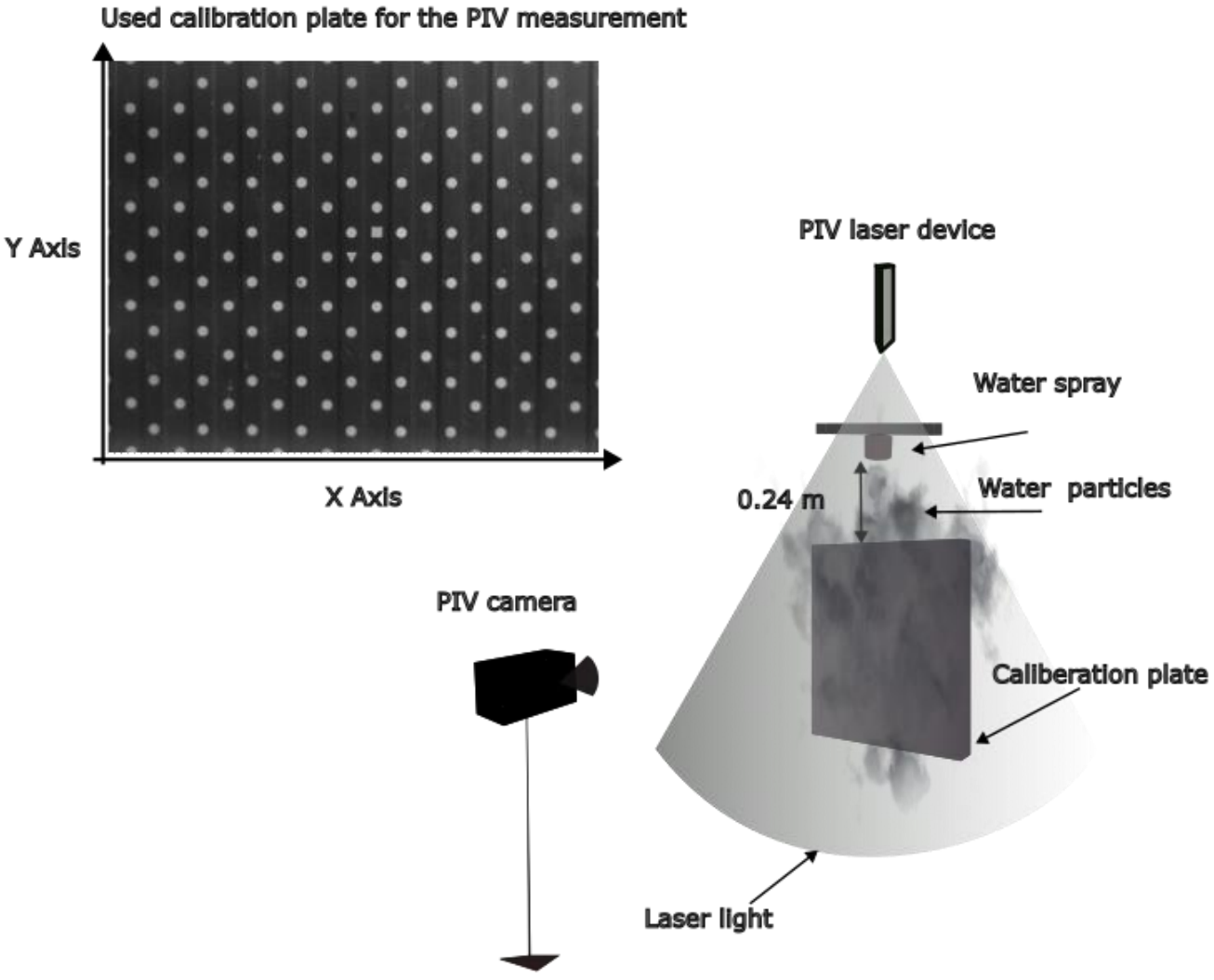

Figure 3- 12. PIV setting for velocity measurement of the water particles right after spraying, and the illustration of the calibration plate.

After the calibration of the view of the camera was performed, the calibration plate was removed to empty the field for velocity measurement. This provided velocity field as a calibration target could be translated into the related measurement domain at various heights (Adrian and Westerweel, 2011). In Figure 3- 13, pictures related to the measurement of the water particles velocity, under the influence of gravitational effect (experiment 1 in Table 3- 1) are provided.

(a) (b)

(c)

Figure 3- 13. Setting for water particle velocity measurement right after spraying (a), to level the calibration plate in front of the camera (b) and a picture taken during the experiment.

The seeding particle materials for the PIV measurement are used to illuminate the velocity fields under the laser pulse. Since homogenous seeding of a wind field was required, a large amount of seeding material was needed in each wind field. If the chosen material for the seeding is pollutive or corrosive, this large quantity can cause pollution, corrosion, etc., particularly at the experimental setup (Stanislas et al., 2013). Materials such as, microballoon, Al_2O_3, olive oil, etc. were considered for application (Melling, 1997). However, these materials were excluded from testing as they could cause health hazards upon inhalation or damage the water in the flume. For instance, olive oil as the seeding material could affect water quality, due to the long required duration to run the experiments (Stanislas et al., 2013). In this study, although the flume's ceiling was movable, it was inconvenient and inefficient to repeatedly remove and replace the ceiling and clean the flume for using olive oil. the entire process could result in technical difficulties.

Based on the above considerations, other types of benign materials for wind field reflection were explored. Firstly, a humidifier device was used to produce water vapour to see if the water vapor may be detected by the camera. The results did not provide sufficient spatial resolution (light reflection by the seeding particles), and the seeding particles were not successfully detected by the PIV camera. It means that the water vapour could not reflect the laser light properly to make the wind field visible. Even when detection occurred, it was rare and only in random areas of the wind field. It could be due to small concentration of the water vapour in the wind field. For this experimental set up, it was not easy to achieve high concentration of the water vapour. The next testing material were burning aromatic sticks. The aim of the test was to ensure that the produced smoke could be detectable by the camera. The material was found to be ineffective due to insufficient particulate content. This means that the produced particles tended to cluster together and did not cover a large part of the wind field. Lastly, water particles were tested and seemed to be functioning. Water particles are advantageous due to not harming the laboratory environment, thereby a healthy environment would be created. On the other hand, water particles may menace the flume by corrosion and condensation (Stanislas et al., 2013). Although, the mentioned threads were not considered as problematic for this study. A sufficient and constant seeding of the particles in a gas field (wind field in this study) must be ensured (Melling, 1997). Therefore, in the wind

velocity field, a section for a set of spray nozzles connected to a water tab was added to the experimental set up.

It was mentioned in Husted et al., (2009) that better velocity measurement results by PIV technique can be obtained, farther from the spray nozzles (Husted et al., 2009). Seeding a field can be classified in two types of local and general seedings. Melling (1997), mentioned to ensure that the seeding particles are spread over an entire measurement field, general seeding with the introduction of the seeding particles (locating the source of seeding particles) well upstream of the measuring velocity field is preferable. Additionally, it was preferable to use general seeding to eliminate the effect of the wake in the wind field related to the seeding device (outlined shape of the cone nozzles), at the location of the measurement (Stanislas et al., 2013). Furthermore, Stanislas et al., (2013) mentioned for the low velocities in comparison to the transonic speeds, general seeding is more advantageous (Stanislas et al., 2013). Therefore, in this study the location of the spray nozzles was considered not at an instant vicinity of the measuring velocity field (0.7 m from the centre of the velocity field). Also, the density of the water particles sufficed for the whole wind field in the PIV measurement.

In experiment number 1, the velocity of water particles from one spray nozzle, used as seeding material was measured both in vertical and horizontal directions right after spraying at a discharge rate of 1.6×10^{6} m^3/s (discharge used for seeding the experiments). The results are provided in Figure 3- 14. The aim was to find the velocity of supplying seeding particles. Figure 3- 14 shows the velocity profile (in 0.12 m height of the field) under no wind effect. The resultant profiles in this experiment are produced by image processing in MATLAB. 6 trials (trial refers to the repeating experiments) for this experiment were conducted. A total 5400 of snapshots of the velocity fields were captured for these 6 trials (experiment 1 in Table 3- 1) (900 images of the evolving velocity fields in each trial). Each velocity field was captured by the pulses of the laser light that illuminated the velocity field during the experiments. For every PIV experiment, the obtained velocity vectors along the x-axis (horizontal direction) of the target plane (Figure 3- 12) were taken. The averaging along the x-axis was calculated by considering the velocity data at each height level and taking the average. Therefore, averaged velocity values along the y-axis (vertical direction) of the target plane were calculated. More detailed description of the plots is provided in section 4.1. The averaged horizontal water

velocities from a nozzle (red markers) are close to zero. This shows the water particles do not move significantly in the horizontal direction. As mentioned before, the velocity of water particles existing directly from a nozzle was 1.25 m/s (obtained from the water discharge from a nozzle), which shows closeness to the averaged values (red markers) in Figure 3- 14 (b) for vertical velocities. The difference is due to the velocity field measurement of the PIV technique being taken at a slight distance from the nozzle outlet. It should be mentioned that the outlet of the cone nozzle was set at vertical direction for this experiment. The closeness of the averaged vertical water particle velocities to the averaged velocities from the PIV technique (red markers in Figure 3- 14 (b)) shows the velocity of water particles are mainly under the influence of water discharge, at short distances from the nozzle. Based on the obtained velocity profiles, averaged velocity values are mainly around 1 m/s.

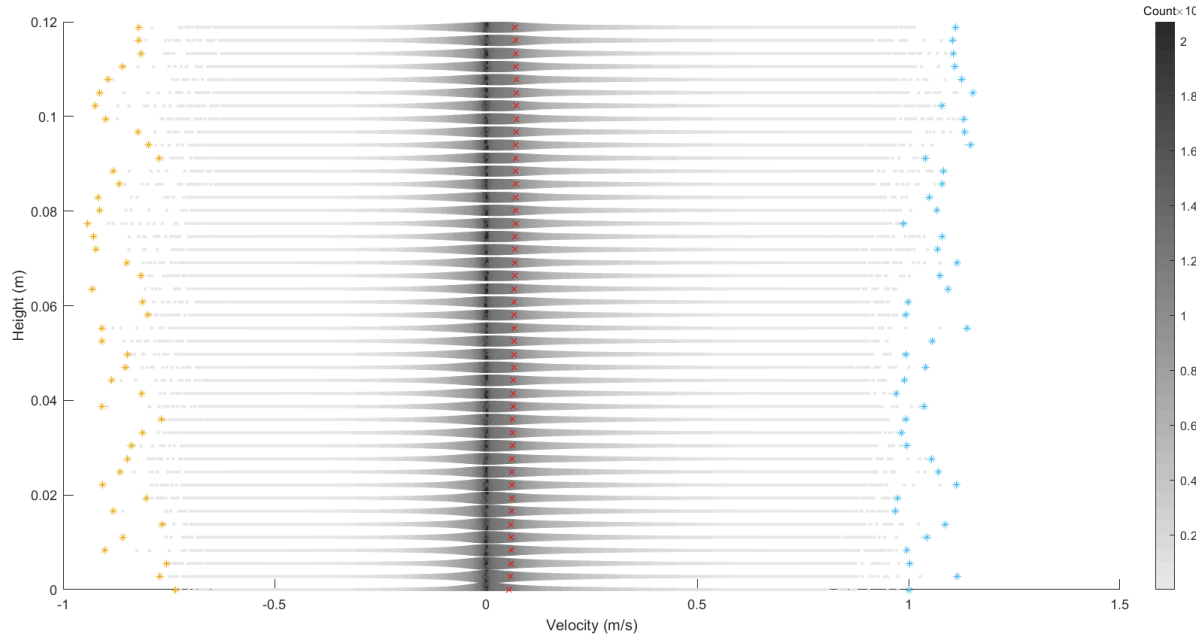

(a)

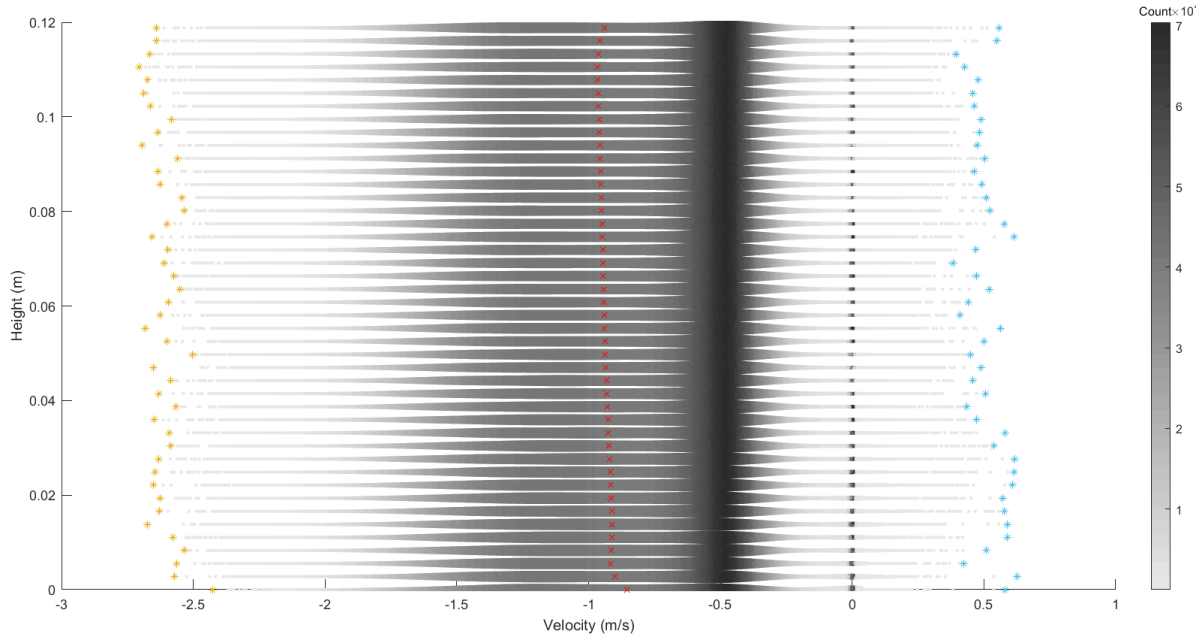

(b)

Figure 3- 14. The velocities of water particles from one nozzle, in horizontal (a) and vertical (b) directions for a discharge of 1.6×10^{6} m3/s. The red markers show the average of the velocity range at each height level, while the yellow and blue markers show the minimum and maximum of the ranges, respectively.

Hollow glass spheres (water-soluble field) were used as the seeding particle material for water velocity field measurement. This material made the water field non-transparent and absorbed the laser light, which was advantageous for the PIV measurement. The concentration of the seeding particle in water was higher than the air. More consistency was

observed in reflection of the spheres in the water fields than that of the water particles in the wind fields. This can be related to the density ratio of the spheres to that of water (1.05), to let seeding particles uniformly distribute in water field (Pu et al., 2013). This uniform distribution of water particles was not observed in the wind field. Inconsistent seeding of the wind field (due to varying densities of the water particles and overlapping particles) could create voids in the calculated velocity vectors (areas with low densities of seeding), in each measurement window. It can be problematic for finding the centroid of the particles in subareas (interrogation areas), for calculating the velocity vectors. Although, the erroneous calculated centroids could be discarded by the DAVIS software. Using hollow particles with lower density ratios in liquid fields (hollow glass spheres in this study), causes larger scattering cross section. Unit particle-fluid density ratio, so called "perfect tracking" is nearly feasible in liquid flows (Melling, 1997). In Figure 3- 15, the reflecting of the seeding particles in wind and water velocity fields are presented. The measurement for water and wind velocity fields were performed separately. It should be noted that the output velocity vectors of the PIV measurements were converted to readable files using MATLAB.

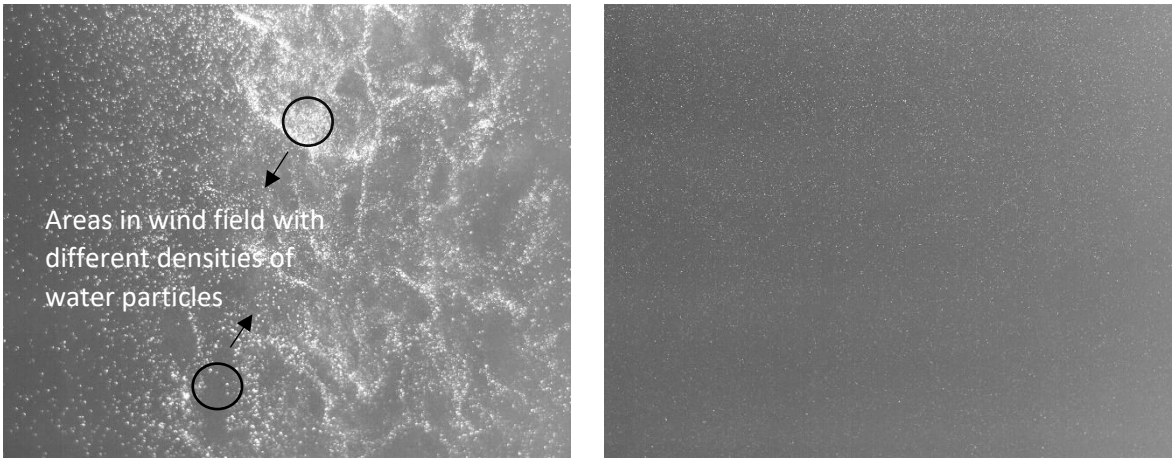

(a) (b)

Figure 3- 15. Reflection of the water particles (a) and reflection of the hollow glass spheres (b) as seeding materials under the pulsing laser for wind and water velocity measurements.

The two-dimensional wind and water velocity measurement was performed by a 2D flowmaster PIV system. The illumination of the fields was carried out by a pulsing dual laser-head system with maximum energy of 50 MJ/pulse, and a maximum laser beam repetition of 50 Hz was used. This device produces a green-coloured laser. The seeding material in PIV

measurement system is implemented to reflect the velocity field, which is illuminated by the laser light. The PIV system software (La Vision type 31) as an optical system that was used to transform the light beam to a 2D sheet (1 mm thickness) by a light-sheet semicylinder lens directly attached to the head of the laser (Pu et al., 2013; Reyes et al., 2015; Timgren et al., 2008). The software also controls the PIV system hardware, and calculates the velocity field (Thomas Jr et al., 2004).

The device was paired with a double-framed charge coupled device CCD (Flow Sense M2/E) camera with zero-degree angle to the measurement field (perpendicular to the laser sheet) (Figure 3- 9). The resolution of this camera was 1280×1024 pixels for taking pictures of the seeding particle materials. The reflections of the seeding particles were captured and used as coupled single-exposed frames in image processing algorithm. Each exposure of the reflecting particles to the camera were captured with a time interval of 0.0018 s, considering the coherence of the seeding particles between consecutive images. Traces of the displacements of the seeding particles were recorded in a view field with the area of 0.369×0.295 m^2. Knowing the time interval between successive frames, and the displacement of the seeding particles, the velocity vectors were defined in so called “interrogation windows”, which are selected as subareas (interrogation areas) for each vector (Biegowski et al., 2020). For processing of the velocity vectors, multi pass cross correlation with decreasing size of the interrogation windows was considered (to find the correlation between windows). It could identify the adjustable parts of two pictures, one after another. For iteration of the sequenced interrogation windows, 25% of their overlap (window offset interrogation) was used. Window offset interrogation could be used to enhance the quality of interrogation results, by reducing the number of vectors that slip the acceptable velocity domain (Adrian and Westerweel, 2011). The size of the interrogation window must be small enough to consider the scale of the flow, and large enough to not miss small-scale flow and recognize the tracer flow pattern (Creutin et al., 2003). For considering the window deformation method, the size of starting and resulting windows were 0.128×0.128 and 32×32 pixels, respectively. 900 images captured the changing velocity field in 15 seconds in each trial (the total time of each trial). The parameters attributed to the PIV setting for the study are summarized in Table 3- 2. PIV settings used in this study are based on (Adrian, 2005, 1991). Some more tests were made, which showed that the results are stable, regardless of the used settings.

Table 3- 2. Applied PIV setting parameters for this study.

PIV software	La Vision type 31
Process type	Post-processing, with local median filter
Resolution of the camera	1280×1024 pixels
Laser system	50 mJ dual laser-head
Maximum repetition rate	50 Hz
View field area	0.369×0.295
Overlap between interrogation windows (Window offset interrogation)	25%
Size of starting windows	0.128×0.128 pixels
Size of resulting windows	32×32 pixels
Number of images for each trial	900
Pulse duration	0.0018s
Measurement time period for each trial	15s

The wind velocity measurement with the PIV technique and the calibration of the view of the camera were performed at the side view of the measurement window, with location of the camera in front of the measurement window (Figure 3- 9). The calibration plate in Figure 3- 12, was positioned in the wind and water fields in terms of calibrating the view of the camera. Firstly, the view of the camera was calibrated for the wind field measurements. Next, measurements related to the wind fields were performed (experiments number 2, 3 and 4 in Table 3- 1). Then the calibration plate was located in the measurement section for the water fields and the view of the camera was calibrated based on this section. It was followed by performing the experiments number 5, 6 and 7. For the wind velocity measurement with PIV technique, the water particles released to the wind field and illuminated under the pulses of the laser (Figure 3- 9). Three different wind velocity fields were set by using one, two and three working fans. For each wind field, nine experimental trials were performed as repeating experiments. In the gas fields (wind field in this study), for higher velocities more seeding particles are required for an interrogation size, in comparison to the lower velocities (Melling, 1997). The nozzle for producing water particles would continuously produce seeding material during the experiments with a constant discharge for different wind velocities. Although, with

increasing the wind velocity, more water particles would carry along the wind tunnel. Because, as number of working fans increased more particles were exposed to and carried out with wind. This could satisfy the need for larger amounts of seeding particles in larger wind velocities.

The PIV digital recordings of movements of the water particles were captured by the camera in each time step (0.0018 s) as raw data. During the process of velocity data extraction from DAVIS software, the velocity vectors of the water particles in each time step were obtained in interrogation windows. An example of wind velocity vector field is provided in Figure 3- 16. The instantaneous wind velocity was captured by calculating the consecutive velocity vectors.

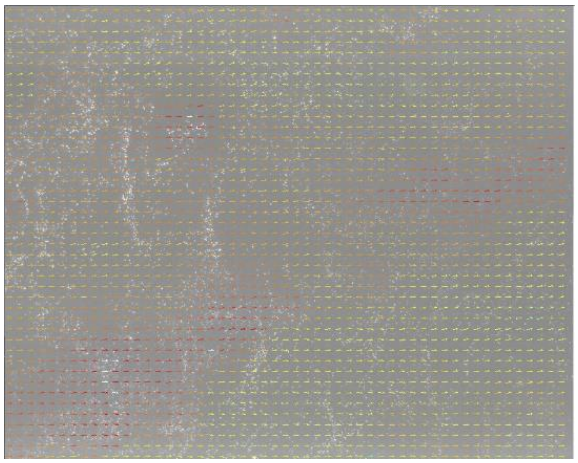

Figure 3- 16. An example of wind velocity vector field measured by PIV technique serving as an example.

Stationary water was considered in the flume, although, the water velocity was measured to observe the effect of wind velocity changes on the water velocity. For this PIV measurement, hollow glass spheres (seeding particle material) were soluble in the water field. It was done based on a method for mixing the seeding particles in liquid which is called “the generation of scattering particles”. Since seeding for PIV technique in liquid fields is usually performed in a closed-circuit loop, it is applicable to introduce and gradually dilute a high suspension into the measurement filed, before the experiment (Melling, 1997). Same procedure was done for diluting the hollow glass spheres in the water field for this study. A homogenized field for the velocity measurement as a result of solubility of hollow glass spheres in the water field was observed. Considering the effect of wind field on water velocity changes, for each wind field, six water velocity measurements were performed. The larger velocity vectors close to the

immediate surface of water were observed compared to the higher depths. And marginal water velocity values for the entire depths were obtained.

Experiments concerning PTV (particle tracking velocimetry) measurement were related to the movement of the ice under the influence of different wind fields. A view field on top of the flume was considered, for measuring the ice movements (Figure 3- 17). As can be seen in Figure 3- 17, measurement scales were installed on the plexiglass cover, at the aim of gradation of the camera's view field. The gradation was also used for distance calibration, later for the analysis of PTV results. The camera for the PTV measurement was located on top of the flume. First, the velocity of the ice pieces (with dimensions of 10×10×1 cm) was measured, followed by the velocity of the ice covers (with dimensions of 50×40×1 cm). The velocities of the ice pieces and covers under the wind generated by one, two and three fans were recorded. The duration of each experiment varied from 3 to 5 minutes. For measuring the velocity of the ice cover, a constant concentration was used, as the ice covers generated a concentration of 1. For the ice pieces, however, varying concentration ranges were considered; 0 to 0.35, 0.35 to 0.7 and 0.7 to 1.

Concentration was calculated based on the number of pieces within a 1-meter length of the view field (0.6 m^2 of view field).

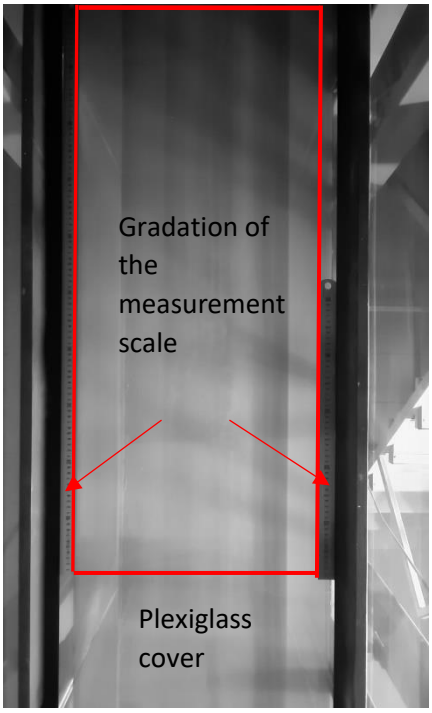

Figure 3- 17. View field of the camera for PTV measurement. The red line shows the border of the view field.

For each wind field, three separate repeating experiments for ice pieces and covers were accomplished. For the small ice pieces that the concentration of ice was important, the three mentioned ranges of the ice concentration (considered for ranging of ice concentration in PTV technique) were collected from the experiments. In other words, three ranges of concentration were obtained within the duration of each experimental run. In Figure 3- 18, samples for each three ranges of concentration are provided. The ice velocity field computation was performed using the free source PTVlab software (Brevis et al., 2011). To calculate ice velocity fields, the maximum time duration of 60 minutes for each range of ice concentration and for each repeating experiment was used. This time duration was the most efficient time expansion in terms of application as an input data in PTVlab software, based on trial and error for obtaining the velocity fields.

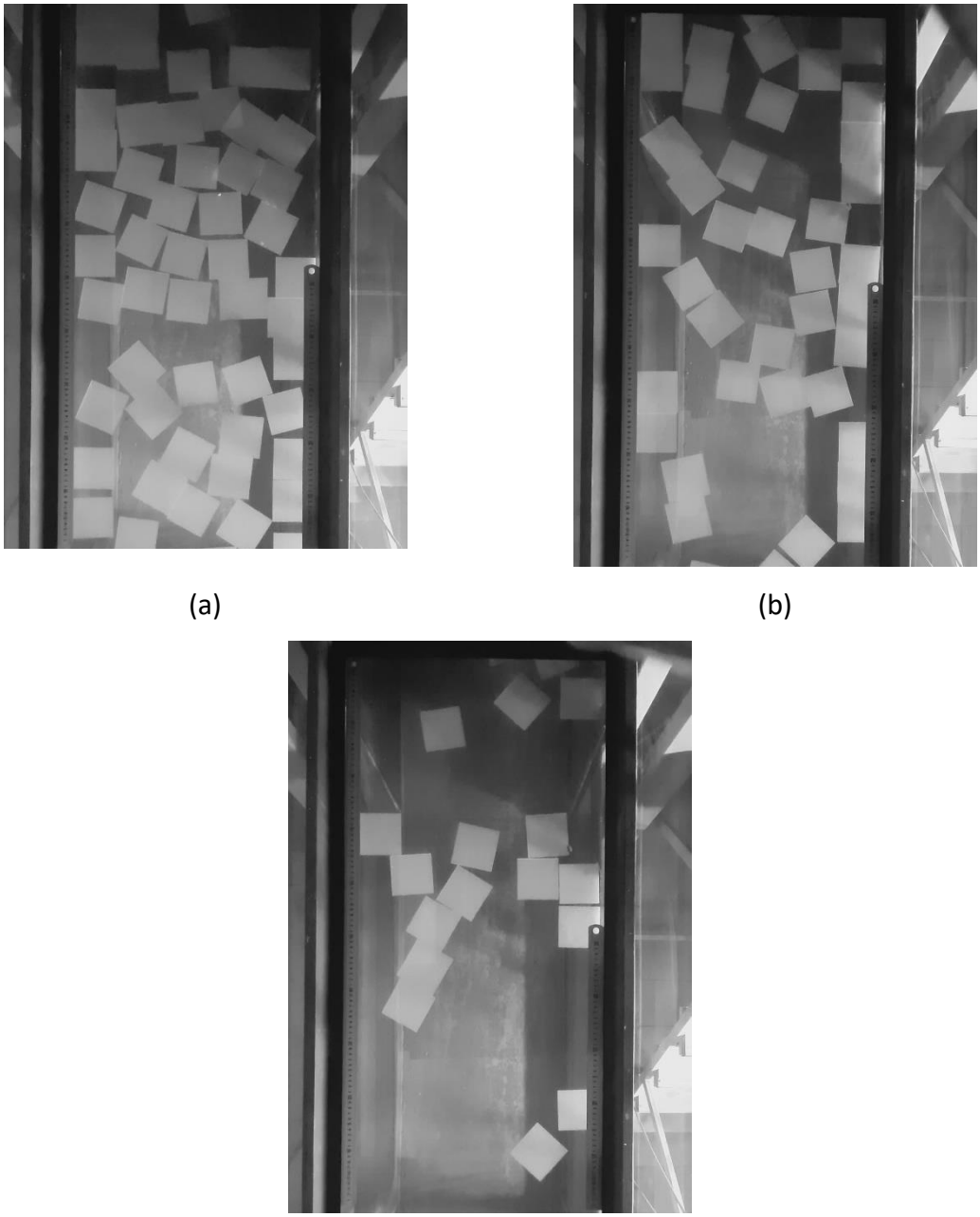

(a) (b)

(c)

Figure 3- 18. Sample of snapshots for low (0-0.35) (a), medium (0.35-0.7) (b) and high (0.7-1) (c) ranges of concentration of ice.

For the cover velocity computation in different experimental setups, the covers were initially marked, to make them detectable by the PTVlab software. However, during the velocity field computations, the painted marks could not be identified by the software. It was then noticed that the surface of the cover itself could be detected by the PTVlab software. In Figure 3- 19, a picture of the covers in an experiment is shown.

Figure 3- 19. picture of the covers in the flume.

In Table 3- 3, the given numbers to each experiment for the PTV measurement are provided. Duration of the experiments depended on the time extension for the entire pieces and covers to pass the view field of the camera. For the experiments related to the ice cover, under the influence of one working fan, lack of ice movement was observed. Therefore, the related experiments were terminated once after starting.

Table 3- 3. Numbering of experiments for the PTV calculation.

Number	Fans			Ice cover	Ice piece	Repetition	Run time (s)	Applied time (s)
	1	2	3					
1	✓			✓		3	780	60
2		✓		✓		3	270	60
3			✓	✓		3	230	60
4	✓				✓	3	-	60
5		✓			✓	3	150	60
6			✓		✓	3	150	60

PTVlab is the software used for the PTV measurement of this study (Patalano et al., 2017b). To perform the computations, the video which captured the velocity field had to be converted to snapshots. To this aim, PTVlab software could produce snapshots by itself. For each 60 s of video with Audio Video Interleave (AVI) format, 1772 snapshots were created. This could be done by introducing a new session for each computation to the software. Before taking the PTV computation runs, required settings should change. It included exclusion mask, image pre-processing, particle detection and PTV setting. Firstly, applying a mask considers the areas of the view field of camera that are not implemented for the PTV computation. Therefore, by applying a mask, every unnecessary part of the view field of the camera for the PTV computation can be blocked. An example of the applied mask (red colour) for the PTV computation in PTVlab software is provided in Figure 3- 20.

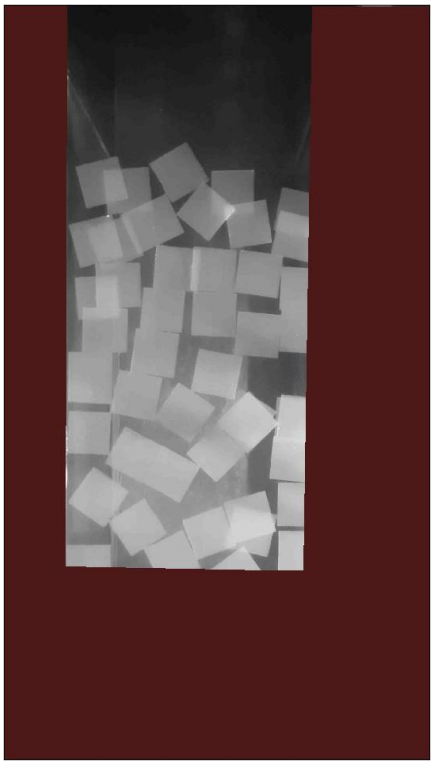

Figure 3- 20. An example of the applied mask on the view field of the camera.

Additionally, for the image pre-processing by "Enable subtract mean" option, it is possible to remove the image background. By activating this option, the background of the picture turns dark. As can be noticed in Figure 3- 21, the ice pieces contrast with the dark background. This

ability of the software allows only the ice pieces to be detected in a subsequent step, which is particle detection (where 'particle' is synonyms as 'ice particle' for this study).

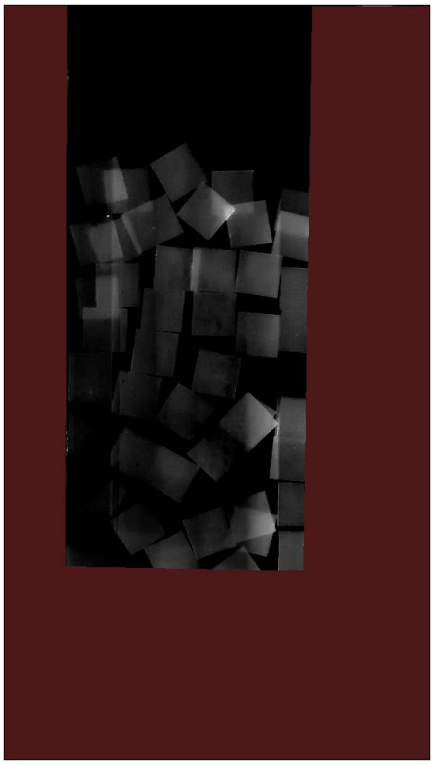

Figure 3- 21. Dark background in PTVlab software.

In the step for particle detection, the density of the detected particles is introduced to the software by correlation and intensity thresholds as well as distance (pixel) of the particles. For these three parameteres 0.5 and 20 as well as 5 pixels were used as the input numbers, respectively. These numbers were chosen, based on trial and error. The factor to be considered was the time duration of the runs. It means high density of the particles would result in enourmous time duration of a run. It also would not change the results to a noticeable extent. The detected pieces would be targetted and marked by red on their surfaces (the surface of the ice pieces). An example of the particle detection on a picture is provided in Figure 3- 22. As can be seen in this figure, pieces that are not in contrast with the background are not detected by the software. This could cause negiligible effect on velocity measurement. In the areas of the flume with the light reflection on the plexiglass cover, it was more probable that the software could not detect the pieces. This defect was more observed in the particle detection for the ice covers. It stems from the fact that the plane of

the ice covers was cohesively distributed along the camera's view field. This means the ice cover did not create much contrast with the background. For the step of PTV settings, the cross correlation algorithm by interogation area of 10 px was used. An example of the software window during a run is provided in Figure 3- 23. The velocity vectors of ice can be seen in this figure.

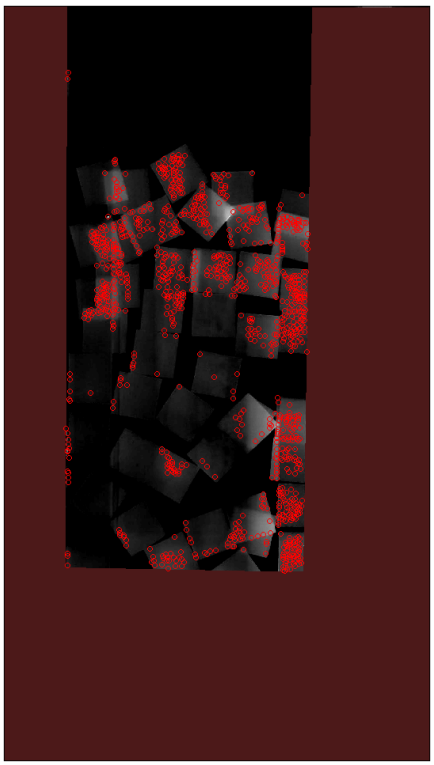

Figure 3- 22. An example of the particle detection in PTVlab software.

Figure 3- 23. An example of the PTVlab software window during a run.

The calibration of the distance was done based on the provided gradation of the measurement scale in the view field of the camera. As can be seen in Figure 3- 24, the gradation could help to find the reference distnace in reality and introduce it to the PTVlab software. At the calibration step of the runs, the time step of the images was also introduced to the software. After the software produces velocity fields, it is feasible to extract velocities from specific areas and points. An example of the velocity field with the collected area for the velocity computation and the location of the PIV measurement are provided in Figure 3- 25. It should be noted that the provided velocity field is related to the high concentration of ice. For the lower concentration of the ice pieces, software could not locate ice pieces at an entire veloity field. Therefore, it was not possible to calculate the velocity field with the same area, in terms of size and location. Therefore, in case of devoid velocity field, the closest size and location of the area to the one provided in Figure 3- 25 was considered.

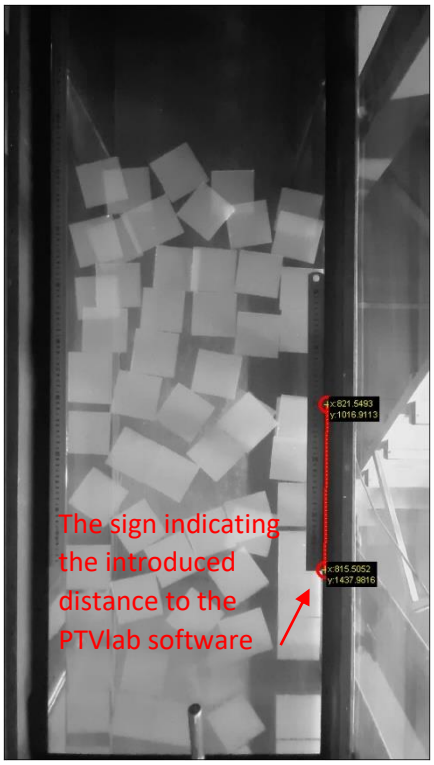

Figure 3- 24. An example of the calibration of distance for a PTVlab run.

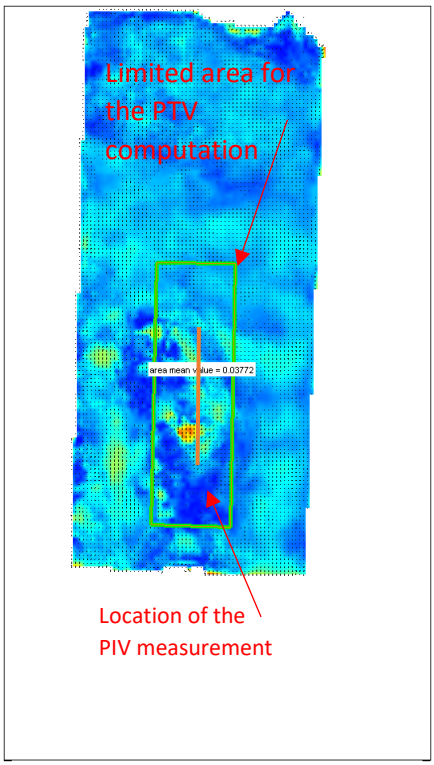

Figure 3- 25. An example of the ice velocity field with the collected area for the velocity computation.

3.2 Mathematical model of wind to ice interaction

Mathematical model is an important complementary tool for field and experimental studies in river ice processes. It revolves around analytical and numerical models, bringing about useful insight in river ice condition (Shen, 2010). The difficulty in physical modelling is the scaling effect, and in field studies, it is isolating the environment from unwanted physical processes within the measurement field. This is where a mathematical model comes in handy, overcoming these challenges while providing additional details (Shen, 2010).

Wu developed wind-stress formulations in sea ice. The formulations were later extended to the DynaRice model for river ice processes (Shen, 2005; Wu, 1973, 1969). Wu extracted the formulation based on 12 laboratory studies and 30 field observations and derived profiles of wind-stress coefficient versus wind velocity (Wu, 1969).

This presented study is a comparison between physical model and numerical simulation, and is based on the latest updated formulation in the DynaRICE model.

3.2.1 Formulation of the wind to ice interaction used in DynaRICE

Ice modelling normally involves two basic simulations; one is ice transport (hydraulics), while the other is ice-load modelling. In hydraulic modelling, similarity between water flow and ice movement, as well as ice jamming are of importance; while, in ice-load modelling, equivalence of forces in ice-structure interaction, ice movement along the banks and around the pier, ice strength, friction among ice parcels, and parcel size are consequential (Zufelt and Ettema, 1996).

Static binary interaction means that the internal interaction of the two bodies does not include the internal forces. The wind effect on ice progressing towards an offshore structure, and a steady advance of a ship in consolidated ice are the examples of static or quasi-static interactions, despite of the cyclicity of the imposed loads (Jones et al., 2012). Wind can have several impacts on the water and ice flow, i.e. increasing water level, and breaking up the ice cover which is more anticipated in the beginning of ice formation (Shen et al., 1997).

CRISSP 2D implement the Discrete Parcel Method on the basis of Smoothed Parcel Hydrodynamics (SPH) at the aim of ice dynamic and the interaction of the ice pieces. Regarding this method, noticeable number of parcels are considered as a continuum, with

specific energy, mass and momentum, consisting of open water areas and ice pieces at the surface area (Wazney et al., 2019). The ice mass elements are defined by particles in this model which represent ice mass parcels (Knack and Shen, 2017). SPH simulation is used to calculate the velocity and placement of each parcel at each time step; Furthermore, the mass density and mass of ice in each parcel, thereby ice concentration can be obtained which has a direct correlation with the convergence of the ice parcel (Shen et al., 2000).

The surface concentration and thickness of each parcel are updated as the ice parcel moves in the domain and interacts with other parcels (the maximum ice concentration is limited by the user) (Shen, 2005). In SPH simulation and at each time step, the ice pass per unit area of measuring domain (ice density) as well as ice parcel velocity and location are calculated (Shen et al., 2000). The surface ice concentration can be calculated based on the mass density and mass of each parcel. As the convergence of the parcels increases, the mass density increases accordingly. The convergence of the ice parcels is limited to the maximum concentration, therefore, once the limitation value is approached, the thickness of the parcels increases (mechanical thickening) (Shen, 2010).

The formulation for internal stresses is based on viscoelastic-plastic (VEP) constitutive law in DynaRICE model. A Lagrangian Discrete Parcel method, set up on smoothed particle hydrodynamics for the simulation of surface ice run is used in this model. The particles (ice mass elements) stand for parcels of ice mass. The parameter that characterises the boom submergence, is the Froude number, related to the flow depth. In the case of considering large Froud number, ice will be stopped and the boom considered as a stop for the ice (0.09) (Kolerski et al., 2013).

Horizontal forces applied on an ice boom are calculated as followed (Crissman et al., 1995):

$$F_H = F_{current} + F_{wind} \qquad \textit{Eq. 3- 1}$$

In Eq. 3-1, F_H, $F_{current}$ and F_{wind} are horizontal, current and wind forces.

The momentum equation related to the surface ice in the Lagrangian form can be written as below (Liu and Shen, 2000):

$$M_i \frac{d\vec{V}_i}{dt} = \vec{R} + \vec{F}_a + \vec{F}_w + \vec{G} \qquad \textit{Eq. 3- 2}$$

In Eq. 3-2, $M_i = \rho_i N t_i$, where ρ_i, N, and t_i represent density, concentration, and thickness of ice, respectively. Additionally, $\frac{d\vec{V}_i}{dt}$, $\vec{R}$, $\vec{F}_a$, $\vec{F}_w$, and $\vec{G}$ are acceleration of ice, internal ice resistance, wind drag, water drag, and gravitational force associated with water surface elevation. The forces in this equation can be written in two-dimensional form (Liu and Shen, 2000).

$$\vec{F}_a = [\rho_a C_a |\overrightarrow{W}|(W_x)N]\vec{\imath} + [\rho_a C_a |\overrightarrow{W}|(W_y)N]\vec{\jmath} \qquad \textit{Eq. 3- 3}$$

$$\vec{F}_w = [-\rho C_w |\vec{V}_i - \vec{V}_w|(u - u_w)N]\vec{\imath} + [-\rho C_w |\vec{V}_i - \vec{V}_w|(v - v_w)\,N]\vec{\jmath} \qquad \textit{Eq. 3- 4}$$

$$\vec{R} = \left[\frac{\partial}{\partial x}(\sigma_{xx} N t_i) + \frac{\partial}{\partial y}(\sigma_{xy} N t_i)\right]\vec{\imath} + \left[\frac{\partial}{\partial x}(\sigma_{yx} N t_i) + \frac{\partial}{\partial y}(\sigma_{yy} N t_i)\right]\vec{\jmath} \qquad \textit{Eq. 3- 5}$$

$$\vec{G} = -M_i g\left(\frac{\partial \eta}{\partial x}\right)\vec{\imath} - M_i g\left(\frac{\partial \eta}{\partial y}\right)\vec{\jmath} \qquad \textit{Eq. 3- 6}$$

In Eq. 3-3, ρ_a, C_a, and $\overrightarrow{W}$ represent the air density, the wind drag on ice coefficient, and the wind speed vector at 10-m level above the water surface, respectively. In Eq. 3-4, ρ, C_w, $\vec{V}_i$, $\vec{V}_w$, u, v, u_w , and v_w denote the water density, the water-on-ice drag coefficient, the ice velocity vector, the depth-averaged water velocity at the lower level of the ice, the ice velocity component in the x direction, the ice velocity component in the y direction, the water velocity component in the x direction, and the water velocity component in the y direction, respectively. In Eq. 3-5, σ_{xx} and σ_{yy} are the normal stress components, while σ_{xy}=σ_{yx}, are the shear stress components. In Eq. 3-6, η represents the water surface elevation.

In the DynaRICE model, the internal resistance between parcels is calculated based on a viscous-plastic constitutive law, while the hydrostatic pressure is calculated using a modified constitutive law (Shen et al., 2000). For low and high ice concentrations, parcels interactions are primarily due to the binary and group interactions, respectively (Shen et al., 1990). Figure 3- 26 provides a view of ice rubble, showing both submerged and non-submerged parts. Here, t_i and t_2 refer to the thickness and submerged thickness of the rubble, respectively. For single-layer floating parcels, the entire length of the rubble can be represented by a single

parcel, which may include both submerged and non-submerged parts. Taking into account the ice porosity (e) and the distance from the water (z), formulations for the pressures on the non-submerged and submerged parts of the parcels in the DynaRICE model are provided in Eq. 3-7 and Eq. 3-8. In these formulations, g is the gravitational acceleration.

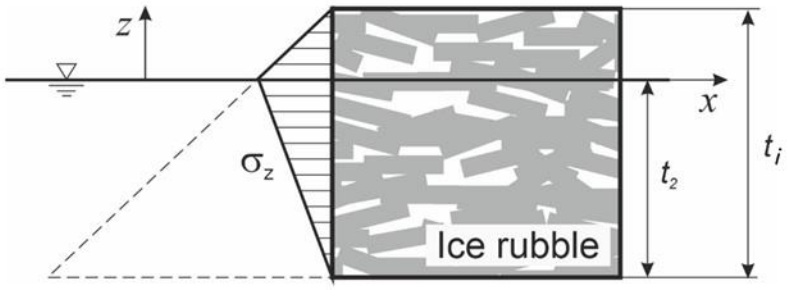

Figure 3- 26. Schematic view of an ice rubble with hydrostatic pressure distribution.

$$(\sigma_z)_{(z>0)} = \rho_i g(t_i - t_2 - z)(1 - e) \qquad \text{Eq. 3- 7}$$

$$(\sigma_z)_{(z<0)} = \rho g(t_2 + z)(1 - e) - \rho_i g(t_2 + z)(1 - e) \qquad \text{Eq. 3- 8}$$

To demonstrate that both equations calculate the same pressure (maximum value) at the water surface ($z = 0$), the following proof is provided in Eq. 3-9 and Eq. 3-10. ($t_2 = \frac{\rho_i}{\rho}$).

$$(\sigma_z)_{(z=0)} = \rho_i g(t_i - t_2)(1 - e) = \rho_i g t_i \left(1 - \frac{\rho_i}{\rho}\right)(1 - e) \qquad \text{Eq. 3- 9}$$

$$\begin{aligned}(\sigma_z)_{(z=0)} &= \rho g(t_2)(1 - e) - \rho_i g(t_2)(1 - e) \\ &= \rho g\left(\frac{\rho_i}{\rho} t_i\right)(1 - e) - \rho_i g(t_2)(1 - e) \\ &= \rho_i g(t_i - t_2)(1 - e) = \rho_i g t_i \left(1 - \frac{\rho_i}{\rho}\right)(1 - e)\end{aligned} \qquad \text{Eq. 3- 10}$$

Taking into account the linear pressure distribution over the ice thickness, the average value is obtained as shown in Eq. 3-11.

$$\overline{\sigma_z} = \rho_i g(t_i - t_2)(1-e) \cdot \frac{t_i}{2} = \rho_i g \left(1 - \frac{\rho_i}{\rho}\right)(1-e)\frac{{t_i}^2}{2} \qquad \textit{Eq. 3- 11}$$

In flow is slow, the hydrostatic pressure over the thickness can be assumed uniform. Additionally, simplifying Eq. 3-11 in 2D leads to Eq. 3-12 (Liu and Shen, 2005; Shen et al., 1990).

$$\sigma_z = \rho_i g t_i \left(1 - \frac{\rho_i}{\rho}\right)(1-e)\frac{t_i}{2} \qquad \textit{Eq. 3- 12}$$

In Mohr's theory, the relationship between normal and shear stresses on a failure plane is given by Eq. 3-13 (Das and Sobhan, 2012).

$$\tau_f = c + \sigma \tan \emptyset \qquad \textit{Eq. 3- 13}$$

In Eq. 3-13, τ_f, σ and c denote the shear stress, normal stress and cohesion all specifically on the failure plane. $\emptyset$ represents the internal friction angle of the failed material (°). In Figure 3-27, θ corresponds to the failure angle of (EF) plane. The planes AB and BC are the maximum and minimum principal planes, indicated by σ_3 and σ_1 stresses, which are located on the Mohr's circle perimeter in section (b) of Figure 3- 27 (Das and Sobhan, 2012). Figure 3- 27 (b) provides an illustrative relationship between minimum and maximum stresses, the internal friction angle of an element, and the failure angle, based on Das and Sobhan, (2012) and Ji et al., (2020). The formulation corresponds to Eq. 3-14.

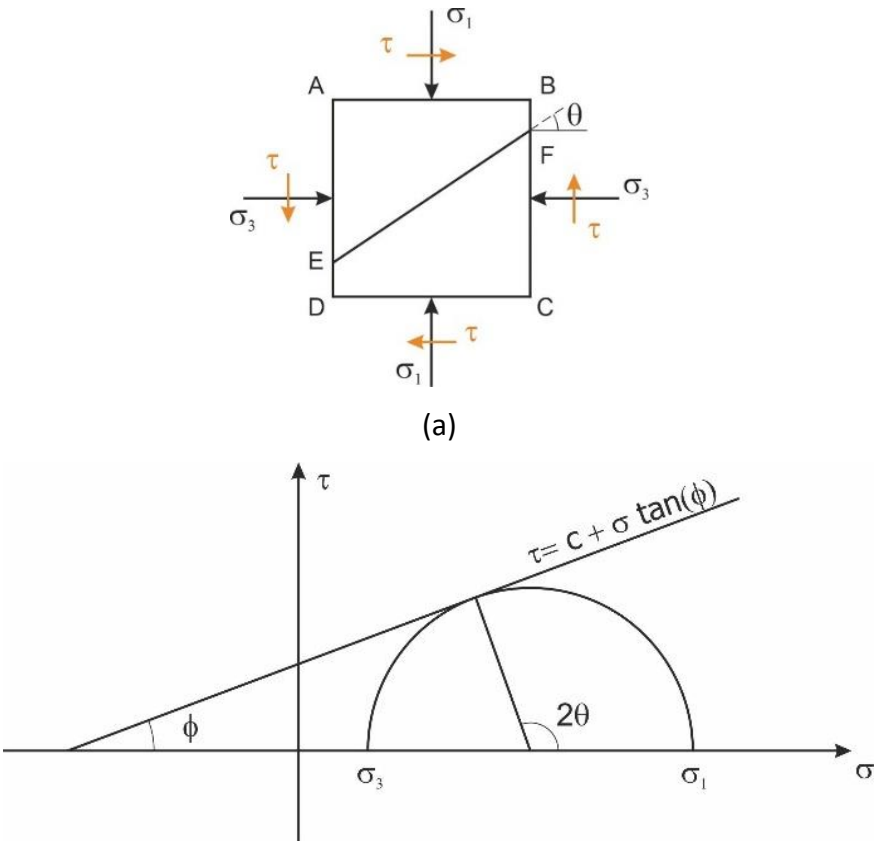

Figure 3- 27. Failure plane of an element (a), and Mohr's circle with a failure envelop (b).

(b)

$$\sigma_1 = \sigma_3 \tan^2\left(45 + \frac{\emptyset}{2}\right) + 2c\tan\left(45 + \frac{\emptyset}{2}\right) \qquad \textit{Eq. 3- 14}$$

If $c = 0$ for ice, then Eq. 3-15 can be derived from Eq. 3-14.

$$\emptyset = \arctan\left(\frac{\tau_f}{\sigma}\right) \qquad \textit{Eq. 3- 15}$$

From Figure 3- 27 (b), and Mohr's circle, the relationship between principal normal stresses and the internal friction angle can be rewritten in Eq. 3-16 (Das and Sobhan, 2012).

$$\emptyset = \arcsin\left(\frac{\sigma_1 - \sigma_3}{\sigma_1 + \sigma_3}\right) \qquad \textit{Eq. 3- 16}$$

If the ice element is in static equilibrium at a depth of (z) in Figure 3- 26, it experiences horizontal and vertical effective pressures, denoted by σ_h and σ_o, respectively. Therefore, the at-rest coefficient of lateral pressure, k_o, can be expressed as follows.

$$k = k_o = \frac{\sigma_h}{\sigma_o} = 1 - \sin \emptyset \qquad \textit{Eq. 3- 17}$$

$$k_0 \sigma_o = \sigma_h \qquad \textit{Eq. 3- 18}$$

σ_h represents horizontal hydrostatic pressure on the ice in its at-rest state, as shown in Figure 3- 27. In addition to the at-rest horizontal hydrostatic pressure, horizontal hydrostatic pressures can also act on the ice when it is in passive and active modes. If the ice is pushed towards another ice piece or parcel, it may enter the passive mode; if it is pushed away, it may enter the active mode.

These modes are illustrated in Figure 3- 28. In both figures, the detached parts in the failure zone of the ice in passive and active pressure states are shown. These parts move in the directions indicated in Figure 3- 28. The forces acting on the ice in active and passive modes are considered to represent the bottom and top of the force range.

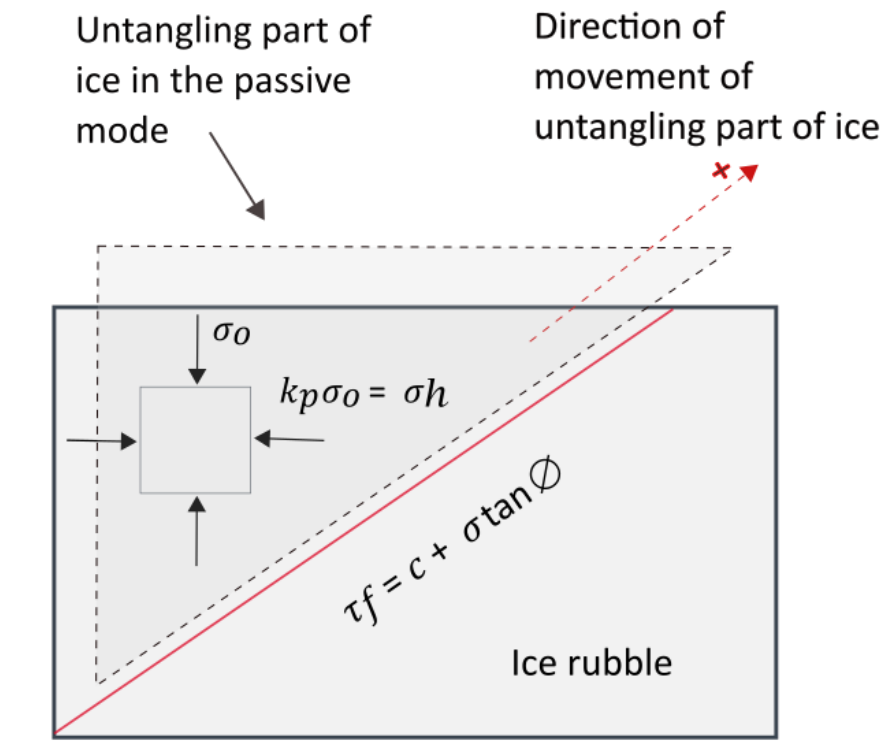

(a)

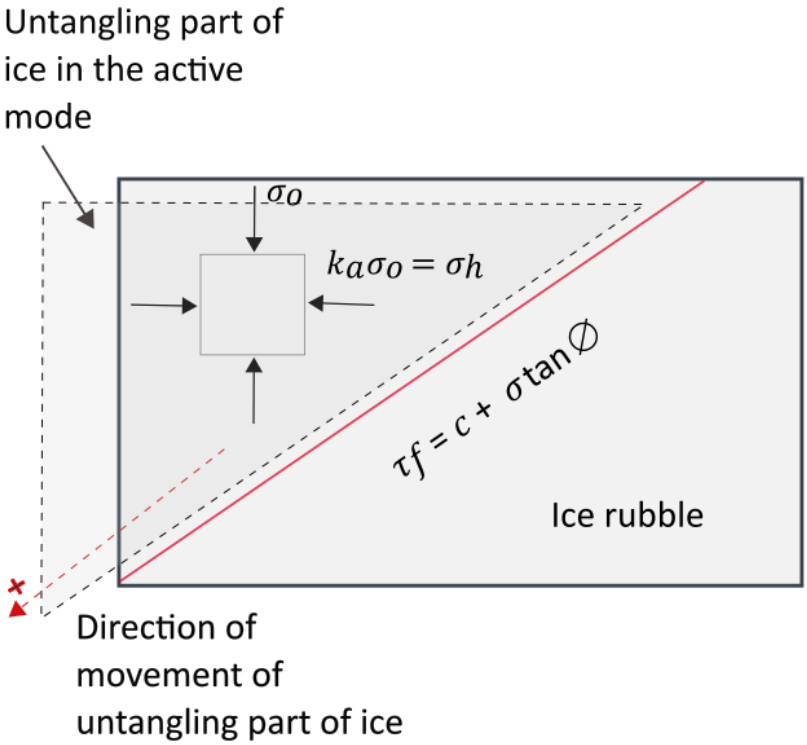

(b)

Figure 3- 28. Schematic view of an ice rubble in the passive (a) and active (b) modes.

The active and passive pressure coefficients, k_a and k_p, are formulated as follows.

$$k_a = \frac{\sigma_a}{\sigma_o} = \tan^2\left(45 - \frac{\emptyset}{2}\right) \quad \text{Eq. 3- 19}$$

$$k_p = \frac{\sigma_p}{\sigma_o} = \tan^2\left(45 + \frac{\emptyset}{2}\right) \quad \text{Eq. 3- 20}$$

The horizontal active and passive hydrostatic pressures are calculated from Eq. 3-19 Eq. 3-20, and finalized in Eq. 3-21 and Eq. 3-22.

$$\sigma_{p/a} = -k_{p/a}\sigma_o \quad \text{Eq. 3- 21}$$

$$\sigma_{p/a} = -\tan^2\left(45 \pm \frac{\emptyset}{2}\right)\left(1 - \frac{\rho_i}{\rho_w}\right)\frac{\rho_i g t_i}{2}\left(\frac{N}{N_{max}}\right)^j \quad \text{Eq. 3- 22}$$

In Eq. 3-22, j is an empirical constant. For static load calculations, the ice load in the passive mode is considered in the DynaRICE model. N and N_{max} represent ice concentration and the maximum ice concentration, respectively. For the numerical simulation, N_{max}, $\emptyset$ and j were set to 0.6, 54° and 15, respectively.

3.2.2 DynaRICE simulation of the ice process related to the wind velocity on ice

Single-layer ice and user-specified parcels are used in this study. The parcels are moved downstream, and the internal forces within the ice cover increase due to imposed external forces, primarily from water and wind. However, if the inter-parcel stress gradient rises, the velocity of the ice parcels decreases. The wind-shear stress formulation in the DynaRICE model accounts for wind and water velocities, but does not consider ice size and concentration. The surface shear stress (τ_s) formulations used in the DynaRICE model are presented in Eq. 3-23 (Shen et al., 1997).

$$\tau_s^{(i-a)} = \rho_a C_a |\overrightarrow{v_i} - \overrightarrow{v_a}| (\overrightarrow{v_i} - \overrightarrow{v_a})$$ *Eq. 3- 23*

In the equations, ρ_a represents air density, C_a is the wind drag coefficient on ice, $\overrightarrow{v_a}$ is the wind velocity, and $\overrightarrow{v_i}$ is the ice velocity.

This study compares the DynaRICE model simulation with a recreated experimental model. To implement the numerical simulation using the DynaRICE model, the study domain geometry first had to be meshed. A 2D finite element mesh was created in a horizontal water flow plane (Shen, 2008). Several runs were conducted as trial and error to the final cell size. The resulting mesh for this study is shown in Figure 3- 29.

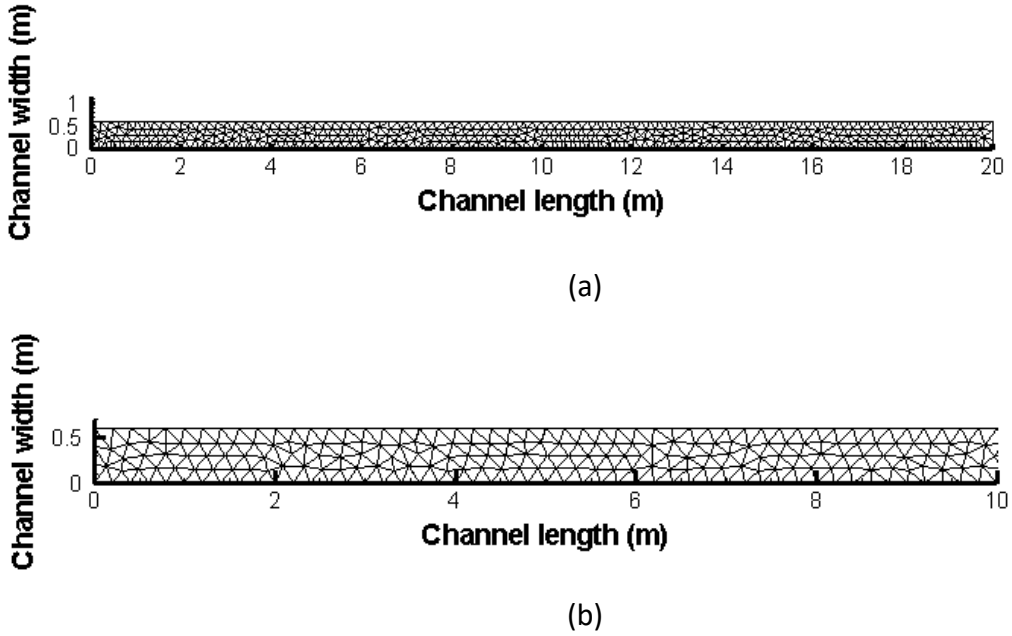

Figure 3- 29. Generated mesh in the model (a) and its magnified view (b).

Figure 3- 29 provides a schematic view of the generated mesh within the domain. The model's dimensions are consistent with those of the experimental model, though, the domain length is extended beyond the experimental model's 3.9 m to a length of 20 m. This additional length was chosen to minimize the effects of the downstream boundary. An Eulerian finite element model (FEM) is used for the hydrodynamic simulation, employing triangular elements with a size of 0.1 m. These FEM triangular elements in the DynaRICE model accommodate irregularities in river domain geometries (Shen, 2008). As previously noted, the cell size was chosen based on the computational run times in the DynaRICE model.

In the DynaRICE model, ice dynamics are solved using the smoothed particle hydrodynamics (SPH) method, in which numerous particles (ice parcels, each containing a number of ice pieces) carry momentum, mass and energy. Properties of neighbouring particles are interpolated, and parcel sizes are tailored for small rivers, rather than the specific dimensions of the study flume. The initial, or lagrangian parcel size is determined by the smoothing length, which defines the interpolation's influential range. A partial-slip boundary condition is implemented with the method of images for the solid boundaries (Kolerski et al., 2013; Liu and Shen, 2005). In this method, an imaginary parcel is positioned on the opposite side of the boundary at twice the smoothing length's distance. The smoothing length varies with temporal and spatial distributions in parcel density, adjusting to achieve optimal accuracy and efficiency (Liu and Shen, 2005). The formulation for the smoothing length (l) in the DynaRICE model is shown in Eq. 3-24, which is an evolution equation for the smoothing length and Eq. 3-25 (Liu and Shen, 2005).

$$l^{n+1} = {l_*}^{n+1} + \frac{\Delta t}{2} {l_*}^{n+1} (\nabla . \vec{v})^n \qquad \textit{Eq. 3- 24}$$

$${l_*}^{n+1} = l_0 (\frac{M_0}{M^n})^{\frac{1}{2}} \qquad \textit{Eq. 3- 25}$$

In Eq. 3-24, $\vec{v}$ is the parcel velocity vector, and Δt is the time step. In Eq. 3-25, M_0 and l_0 are the initial mass density and initial smoothing length, respectively. The ice parcels search area must be selected to ensure simulation stability and accuracy, as well as efficient run times (Liu and Shen, 2005). In the DynaRICE model, the search area is estimated as a uniformly distributed ice field with parcels of equal mass, as shown in Eq.3-26 and Eq.3-27 (Liu and Shen, 2005).

$$m = \Delta A M \qquad \textit{Eq. 3- 26}$$

$$M = \rho_i N t_i \qquad \textit{Eq. 3- 27}$$

In Eq. 3-26 m is the mass of each parcel in the search area, ΔA is the parcel size and M is the parcel density. In Eq. 3-27, ρ_i, N and t_i represent ice density, concentration and thickness, respectively. The smoothing length of the ice parcel in the DynaRICE model is determined by the Eq. 3-28 and Eq. 3-29 (Liu and Shen, 2005).

$$\Delta A = \Delta x \times \Delta y \qquad \textit{Eq. 3- 28}$$

$$l = l_x = l_y = \Delta x = \Delta y \qquad \textit{Eq. 3- 29}$$

In Eq. 3-28, Δx and Δy are parcel dimensions in x and y directions. In Eq. 3-29, l_x and l_y are the smoothing lengths of the ice parcels. A square search area, cantered on each parcel, spans $4l \times 4l$, encompassing 5×5 parcel grid (Liu and Shen, 2005).

As noted, the DynaRICE model applies the method of images for the boundary conditions. Thus, an imaginary parcel is placed at a distance of $2l$ from the boundary for each parcel positioned at the same distance within the domain. Each of imaginary parcel shares equivalent concentration, mass, pressure and tangential velocity with the corresponding real parcel (Liu and Shen, 2005). However, while the normal internal stress of an imaginary parcel matches the real parcel's value and direction, its normal velocity and shear stress are directed oppositely (Liu and Shen, 2005).

In the DynaRICE model, upstream boundary conditions include ice thickness, concentration and velocity; ice velocity at the upstream boundary is generally reduced to free drift, as it is typically unknown (Liu and Shen, 2005). For hydrodynamic boundary conditions under sub-critical flow, different combinations of water discharge and water level are assigned to the upstream and downstream boundaries, respectively (Liu and Shen, 2005). Figure 3- 30 illustrates the upstream and downstream boundary locations on the generated mesh, with boundaries identified in the DynaRICE model via the boundary nodes of the mesh.

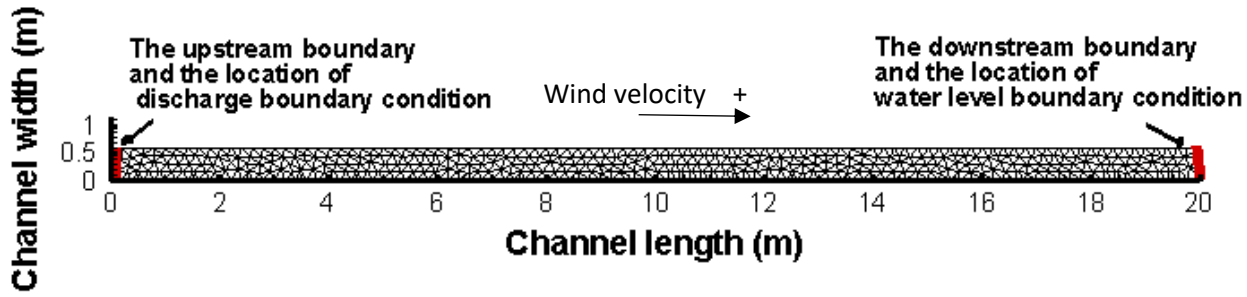

Figure 3- 30. The location of boundaries and the placement of boundary conditions on a generated mesh.

To stablish the initial hydraulic conditions for the ice simulations, a cold start run is conducted using the DynaRICE model (Liu and Shen, 2005). The cold start run provides stable hydraulic conditions (initial conditions) necessary for starting the ice simulations. The hydrodynamic initial conditions include the discharge and water level at each finite element node (Shen, 2008). For a cold start run, the initial boundary conditions (previously discussed) at the beginning of the simulation (t=0) are input into the model, which then generates the hydrodynamic initial conditions to be used in a hot start run. The ice initial conditions—comprising the ice velocity, concentration, thickness and internal ice stresses—can also be obtained from a previous run (either hot or cold) (Shen, 2008).

Since replicating the physical model with numerical simulation is not a straightforward, single simulation process, the numerical experiments were conducted in three stages.

1- **First step (Cold start):** In this phase, only hydraulic simulation was conducted, with ice and wind simulation excluded.
2- **Second step (Hot start):** Ice was introduced into the domain from the upstream boundary, with high-water velocity considered to achieve the desired ice accumulation. Wind simulation was not performed during this stage.
3- **Third Step (Hot Start)**: The ice was positioned in the domain using the ice concentration from the previous step, with zero initial ice velocity. No water velocity was applied, but wind simulation was conducted.

An infinitesimal discharge of 0.0001 m^3/s was applied at the upstream boundary. Though zero discharge was the intended approach, trial-and-error methods indicated that a very small

discharge value would better achieve the free-drift condition of the ice. The water level was specified at the downstream boundary (at 0.595 m), as shown in Figure 3- 30.

To incorporate wind effects into the simulations, the initial ice concentration was generated via a hot start run following the setup of initial hydrodynamic conditions. These simulated ice concentrations were calibrated to experimental observations and classified into three types: low, medium, and high concentration. To simulate the wind effect on the ice, the final run was conducted with a hot start using initial conditions based on the selected ice concentration (output from the previous hot start), wind velocity, an infinitesimal water discharge, and zero ice velocity (ice velocity from the prior step set to zero). Wind velocities were averaged from experimental study values.

To achieve appropriate ice concentration for each final hot start run, a combination of water and input ice discharges was tested as initial conditions. High ice concentrations could not be obtained solely by varying water and ice discharge combinations. To simulate breakup conditions, a hot start run was performed after obtaining a steady hydraulic state to establish an ice cover as the initial condition. In the final run, this cover was fragmented into desired ice piece sizes (Shen, 2008). In this breakup simulation, a high ice concentration was achieved by fragmenting the ice cover at the beginning of the final run, with wind applied as an initial condition. Among various potential breakup conditions (e.g., specified breakup time and location, water level fluctuations, or water level limits), the breakup was set to occur at the start of the final run (Liu and Shen, 2005).

Once an ideal concentration based on experimental simulations was achieved, the ice condition served as the initial condition for the final run. For this run, initial conditions included an infinitesimal water discharge, zero ice discharge, and the specified wind velocities (0.514695, 1.165798, and 1.499304 m/s). Based on the descriptions above, three sets of runs were established for the simulations: (1) hydrodynamic initial conditions, (2) initial ice concentration conditions, and (3) a final run combining hydrodynamic and ice initial conditions with wind influence. The initial conditions for simulations using the DynaRICE model are outlined in Table 3- 4 and Table 3- 5.

Table 3- 4. The hydrodynamic initial conditions (cold start).

Ice concentration	Input ice discharge	Water level	Input water discharge	Wind velocity
$(-)$	$\left(m^3/s\right)$	(m)	$\left(m^3/s\right)$	(m/s)
0	0	0.595	0.0001	0

Table 3- 5. The hydrodynamic initial condition for producing ice concentration (hot start).

Numerical model Type	Ice initial concentration	Upstream Input ice discharge	Water level	Input water discharge	Wind velocity
	$(-)$	$\left(m^3/s\right)$	(m)	$\left(m^3/s\right)$	(m/s)
Ice concentration= 0.125	0	0.2	0.595	0.1	0
Ice concentration= 0.325	0	0.4	0.595	0.1	0
Ice concentration= 0.525	0	0.5	0.595	0.1	0
Ice concentration= 0.65	0	0.6	0.595	0.1	0
Final runs	0.125	0	0.595	0.0001	0.514695 1.165798 1.499304
Final runs	0.325	0	0.595	0.0001	0.514695 1.165798 1.499304
Final runs	0.525	0	0.595	0.0001	0.514695 1.165798 1.499304
Final runs	0.65	0	0.595	0.0001	0.514695 1.165798 1.499304

4 Analysis of the physical model study results

In this section, the Analysis and results related to PIV and PTV techniques are provided. The verification of the results related to the PIV technique, carried out by comparing them with those from an anemometer device, as well as the outcomes of various attempts to present the results are also provided in this chapter. For the PTV measurement, two approaches were considered, based on the selection of the area for the PTV measurement. For one approach, a limited, confined area within the measurement field (the limited area referred to in Figure 3- 25) is considered, while for the other approach, the entire measurement field (referred to in Figure 3- 17) is taken into account. The two approaches were tested to see which one can more accurately measure ice velocity.

4.1 PIV measurements (related to the wind and water velocity)

In PIV technique, the velocity vectors of seeding particles (water particles in the wind field and hollow glass spheres in water field) were captured in a fraction of a second (0.0018 s). Therefore, for each PIV trial measurement, 900 images are produced. A MATLAB code was developed to handling the obtained data. The velocity vectors relate to time and distance in x and y directions. The velocity vectors were derived at each time instance (0.0018 s) and for the whole captured seeding particles by the camera, with different x and y coordinates. Different attempts were made to determine the most suitable approach for capturing the overall velocity of the wind and water fields. It should be mentioned that, for this study, the location of the particles in the x direction (x-axis, in Figure 3- 9 and Figure 3- 12) was of no concern. It was because the measurement field was considered representative of the entire length of the flume.

The averaged velocity of each trial along the height of the wind flume (height level of the field and y coordinate) was calculated. In Figure 4- 1, the calculated velocity for each trial along the height of the flume is presented. The average velocities from nine trials at each height level are also calculated and indicated by the red lines. The colours of the lines get lighter moving from the first to the ninth trial, producing a grey hue. As can be seen in Figure 4- 1, for the wind field with three working fans, excluding the 20 cm close to the ceiling of the wind flume, symmetry is observed on the either side of the stagnation point. This is not observed in the wind velocity profiles for the two and three working fans. It also can be noticed, at the

adjacent of the ceiling (as the coordinate origin can be seen in Figure 3- 9), the most effects are observed for the wind fields with one and two working fans. Same profiles were produced for water, although, they are not presented.

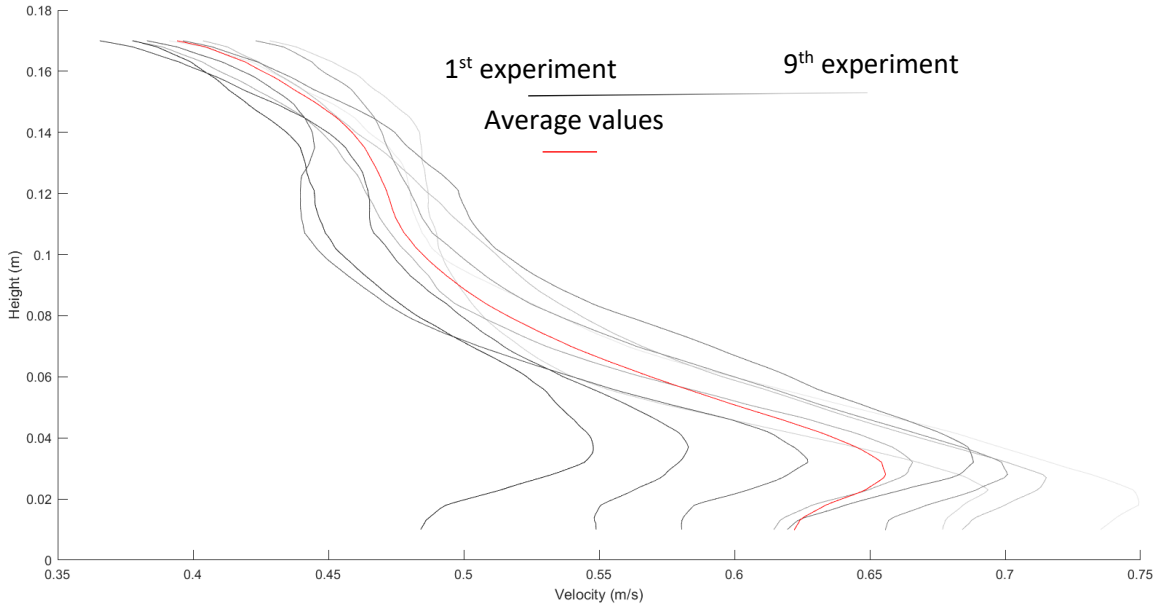

(a)

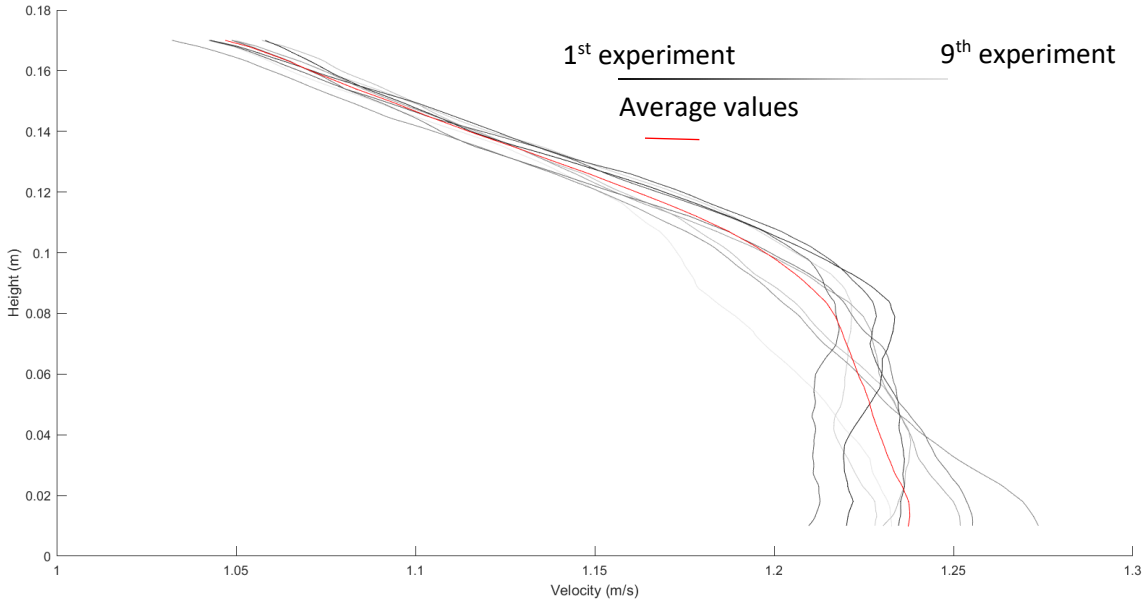

(b)

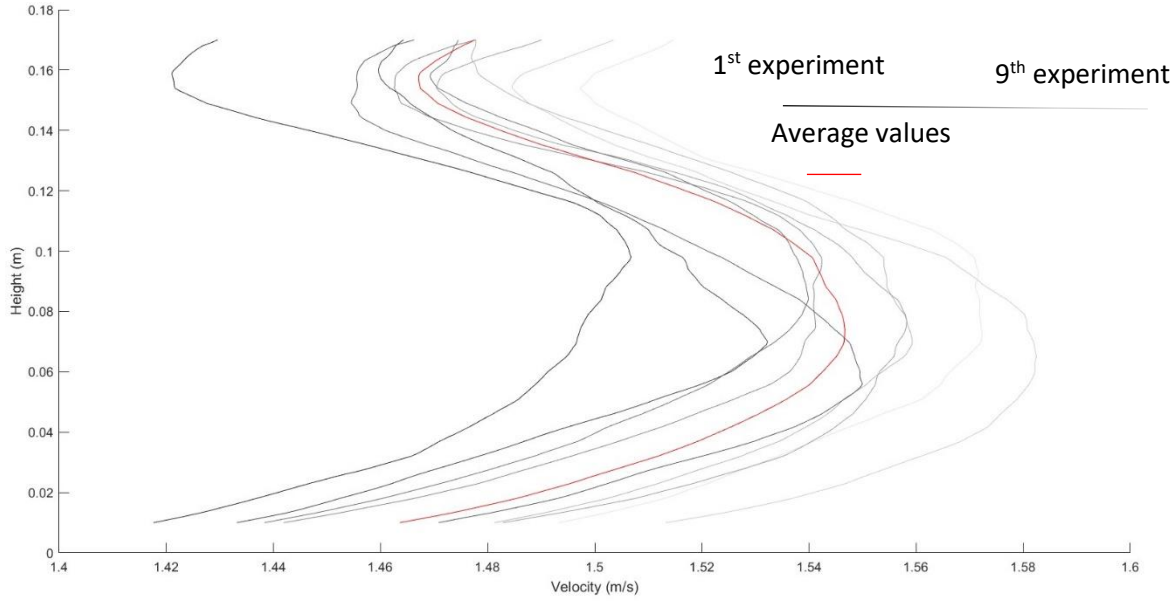

(c)

Figure 4- 1. Wind velocity profiles for one (a), two (b), and three (c) working fans (the grey hue indicates changes from the first to the nineth experimental trials, becoming lighter in colour). The velocity of each trial at each height level were averaged, using MATLAB. The averaged velocity values of all trials are shown along the height level of the wind field with a red line.

Figure 4- 2 shows the standard deviation errors of the wind velocities. The averaged values in Figure 4- 1 are shown as red circles in Figure 4- 2. For each height level, the calculated error involves all the related velocity values. The used formula for the Standard deviation (STDE), is provided in Eq. 4-1.

$$\mathrm{STDE} = \frac{\sqrt{\frac{1}{\mathrm{Q}-1}\Sigma_1^{\mathrm{Q}}(\mathrm{lU}-\overline{\mathrm{lU}})^2}}{\sqrt{\mathrm{Q}}} \qquad \textit{Eq. 4- 1}$$

In this equation, lU is the longitudinal velocity vectors in each field, and Q is the number of vectors. $\overline{\mathrm{lU}}$ is the averaged value of the longitudinal velocities. The relative results in Figure 4- 2 give low values for the error calculation that indicates the accuracy of the calculation.

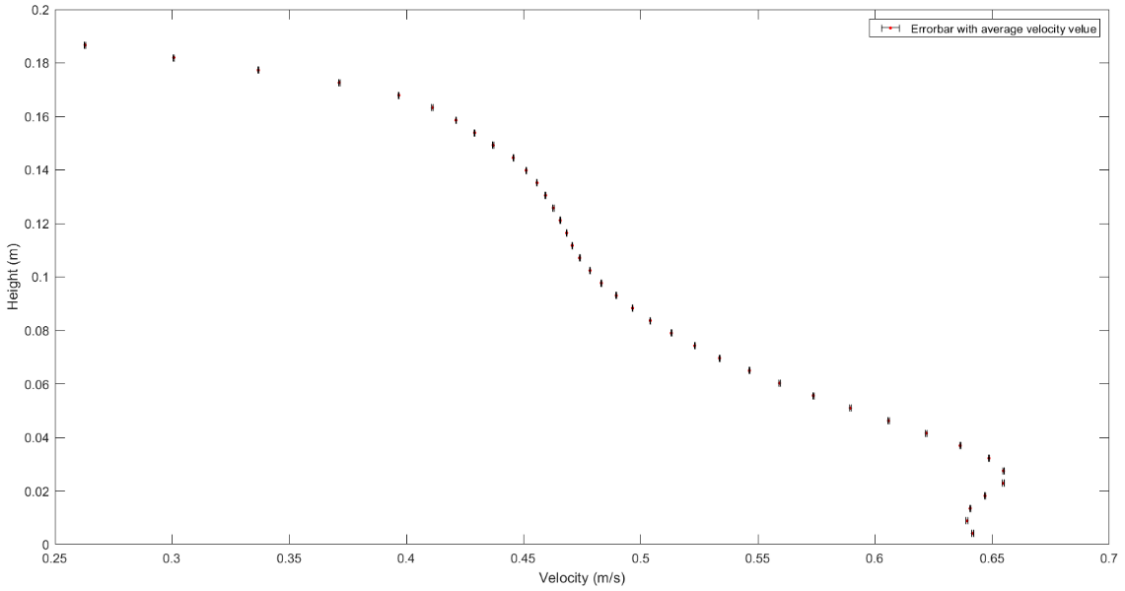
Errorbar with average velocity velue
Height (m)
Velocity (m/s)
0.2
0.18
0.16
0.14
0.12
0.1
0.08
0.06
0.04
0.02
0
0.25
0.3
0.35
0.4
0.45
0.5
0.55
0.6
0.65
0.7

(a)

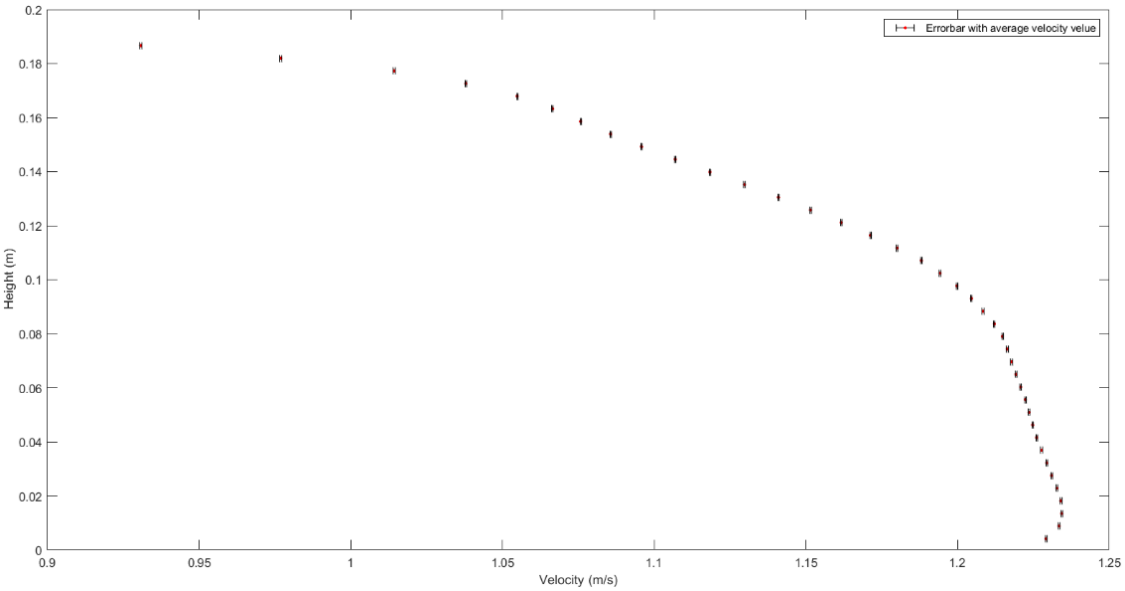
Errorbar with average velocity velue
Height (m)
Velocity (m/s)
0.2
0.18
0.16
0.14
0.12
0.1
0.08
0.06
0.04
0.02
0
0.9
0.95
1
1.05
1.1
1.15
1.2
1.25

(b)

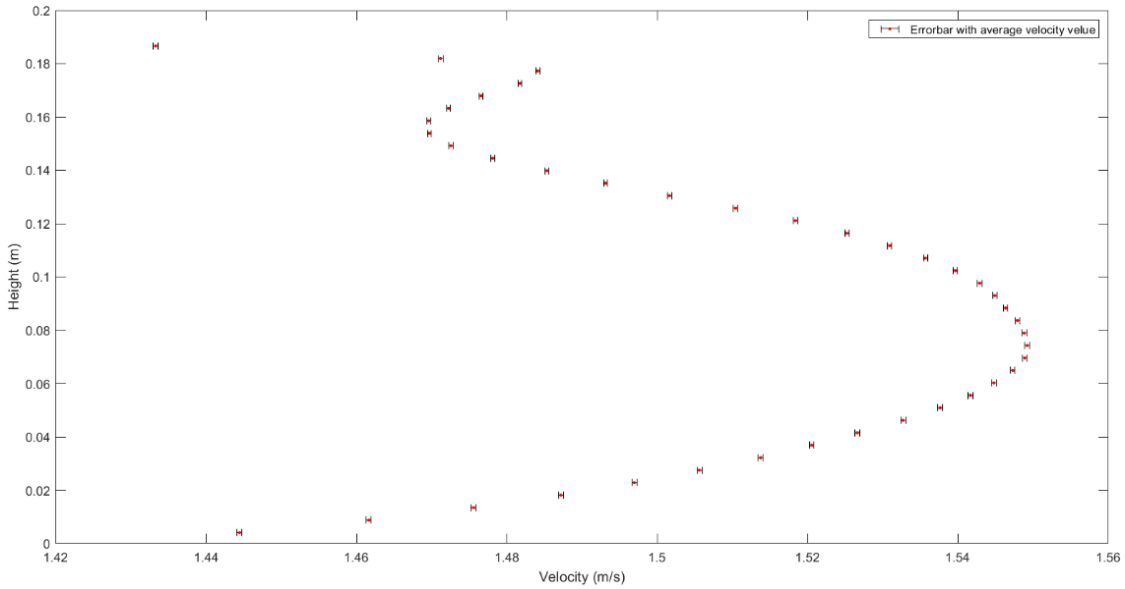

(c)

Figure 4- 2. Standard deviation error of wind velocity values along the height levels of the flume for the wind fields with one (a), two (b) and three (c) working fans.

To have a better understanding of the PIV measurement results, a statistical analysis was performed by gathering the data from all the trials in one table to exclude the averaging effect. This means that for the further processing, the velocities were not averaged along the x direction nor over time. In this way, after the analysis, just one set of data would be obtained showing varying velocity values along the y direction (along height of the flume). The purpose of this approach was to minimize the influence of time (during each experimental trial) and the x-coordinate of the water particles (the position of the seeding material along the x-axis). Although, the entire data related to different x-coordinate for each height level were taken into account. Therefore, raw velocity data could be classified by changing the distance along the height levels of the flume. It can be noted that this method of classification is well-suited for organizing the data, given the primary goal of the analysis, which is to achieve a specific data range. This could show all the velocities captured at each height level of the flume.

In Figure 4- 3, the distribution of the wind velocity along the height of the flume is provided (the origin coordinate for the wind flume height is provided in Figure 3- 9). These results refer to experiments 2, 3 and 4. Three lines indicating minimum, maximum and average velocities along the height of the flume are shown.

Negative values for the wind velocities were observed. The negative values can relate to the turbulence at the wind field and the water particles moving backwards. Also finding particle centroid in interrogation areas with overlapping particles may calculate erroneous velocity vectors. It has been suggested that the accuracy of the velocity vector measurement is highly related to finding the particle centroid that can be problematic in interrogation areas with overlapping particles (miss-track particles) (Okamoto et al., 2000). This can cause bias in the PIV correlation. Miss-track particles are not a matter of concern in this study, because the algorithm used for PIV, would remove miss-track particles, automatically. Besides, variety of velocity vectors were checked accurately, and movements of the particles in negative direction were observed. It showed that negative velocities of the particles were correctly calculated by the DAVIS software, and they cannot be considered as erroneous values.

In the wind field with three working fans, smaller negative velocity values were observed. The wind generator was covering the entire width of the wind flume intake with the blowing wind. The larger velocities with negative direction were observed in the wind field with one working fan. In Figure 4- 3, the lines for maximum and minimum values are the calculated velocities along the height of the flume. The calculated velocity values between maximum and minimum lines are filled with grey areas. The averaged values are obtained for each height level, shaping the average line. Considering the average line for the wind field with three working fans, the most unified distributed values along the height of the flume were observed. Although, no drastic changes were indicated for the other wind fields, as well. The maximum averaged values for the wind velocity for the three, two and one working fans were 1.5, 1.25 and 0.6 m/s, respectively.

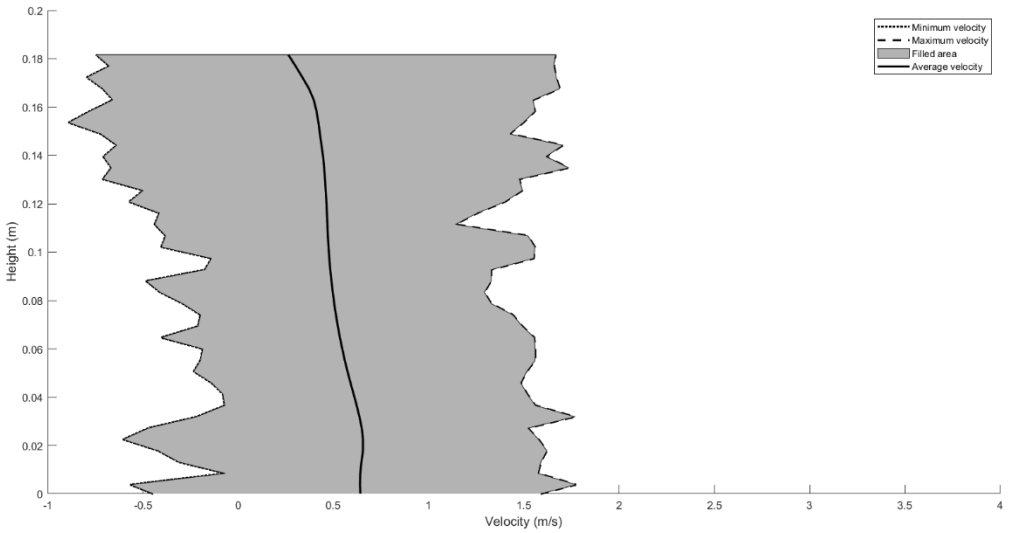

(a)

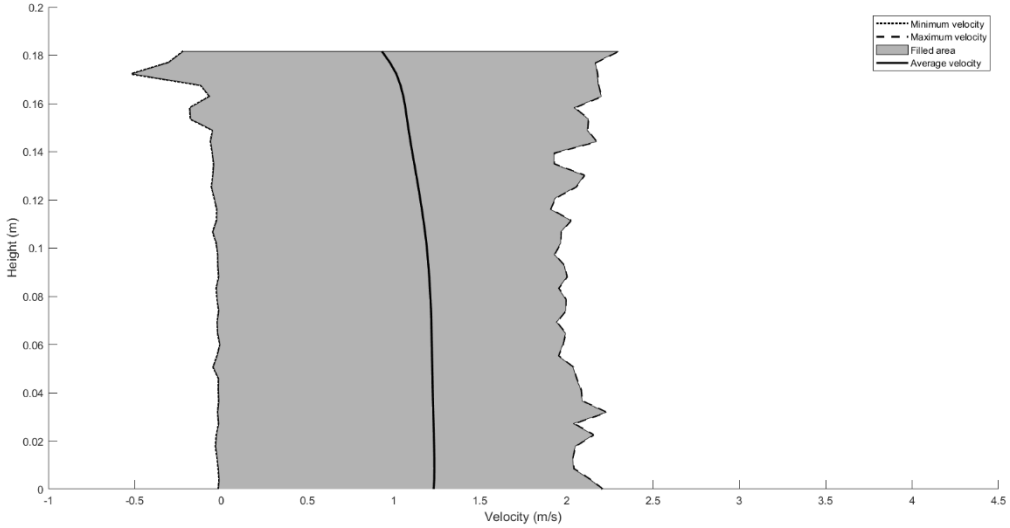

(b)

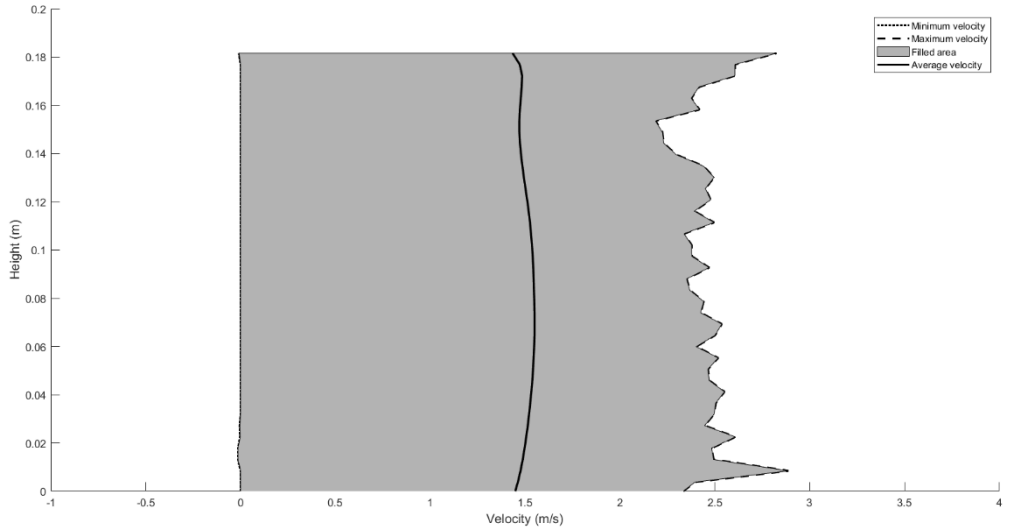

(c)

Figure 4- 3. Wind velocity profiles along the height of the flume, for the wind fields with one (a), two (b) and three (c) working fans.

To enhance analysis of the collected data, swarm plots were created, incorporating histogram counts at each height level (Figure 4- 4). This approach offered more insight into distribution of velocity values per height level. Swarm plot thickness is in accordance with the empirical density function at each height level. The grey shade conforms to the absolute data count from all measurements, with darker colour indicating higher repetitions. The averaged values are in red, minimum in yellow and maximum in blue. Green dashed lines indicate the maximum fan discharge velocity. The results comply well with the steady and uniform flow assumption. The reason is the proximity of the mean values with the maximum fan discharge velocity. Fan discharge lines are within the darkest and most prominent part of the swarm chart. There is an exception for the plot related to the wind field with one working fan, where highly replicated data is close to zero, suggesting limited wind field influence due to a small transactional area affected by the fan's inlet area.

The distributions in the swarm plots are limited to a velocity percentile range of 2.5 to 97.5. The range of the maximum count coincides well with the averaged values indicated by the red markers at the major levels in the most cases. The spread of the data can be attributed to irregularities in the airflow, as a few vortices were spotted in the PIV velocity maps during visual inspections. Vortices also caused the appearance of the minimal velocity values in the negative direction. Although, the observed increased data count at zero velocity is related to the inhomogeneous seeding and decreased particles in subregions resulting to an erroneous PIV calculation (the blind spot of the camera). This is the most problematic for the low wind velocity (Figure 4- 4 (a)) and less critical it becomes with the increase in wind velocity from one to three working fans. Therefore, the rearrangement of the nozzles into an array to enhance the coverage of the wind field should improve the accuracy of the results.

Averaged values of the data indicated by the red markers in Figure 4- 4 were obtained over the depth of the wind field. The results showed velocities of 0.514, 1.165 and 1.499 m/s for the wind fields with one, two and three working fans, respectively. The errors represent the differences between the averaged wind velocity values from the PIV technique (red markers) and the velocities produced by the fans (green dashed lines). The corresponding calculated errors were 1%, 11% and 4%. These ranges of errors seem to be promising for a low-budget experimental set up.

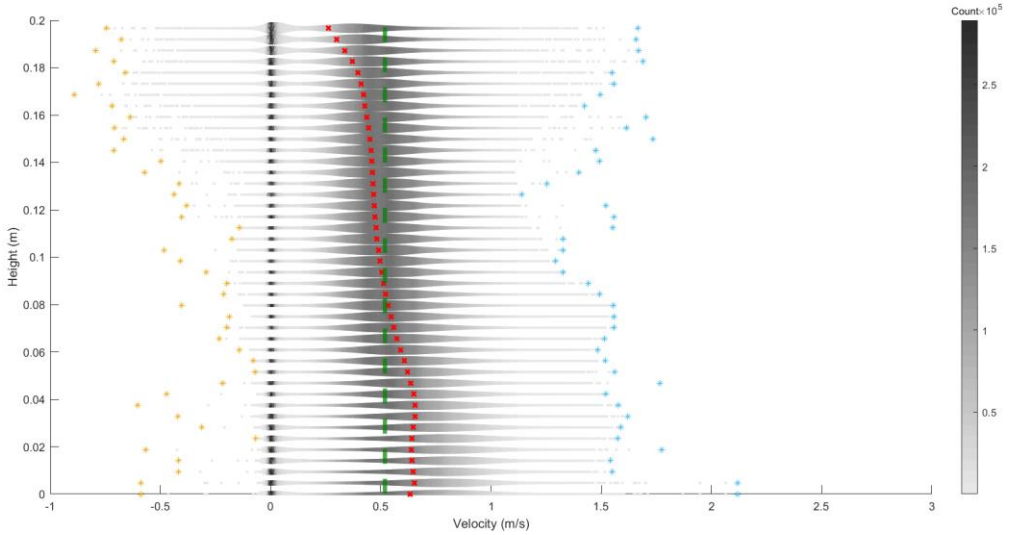
Count ×10^5
2.5
2
1.5
1
0.5
Height (m)
0.2
0.18
0.16
0.14
0.12
0.1
0.08
0.06
0.04
0.02
0
-1
-0.5
0
0.5
1
1.5
2
2.5
3
Velocity (m/s)

(a)

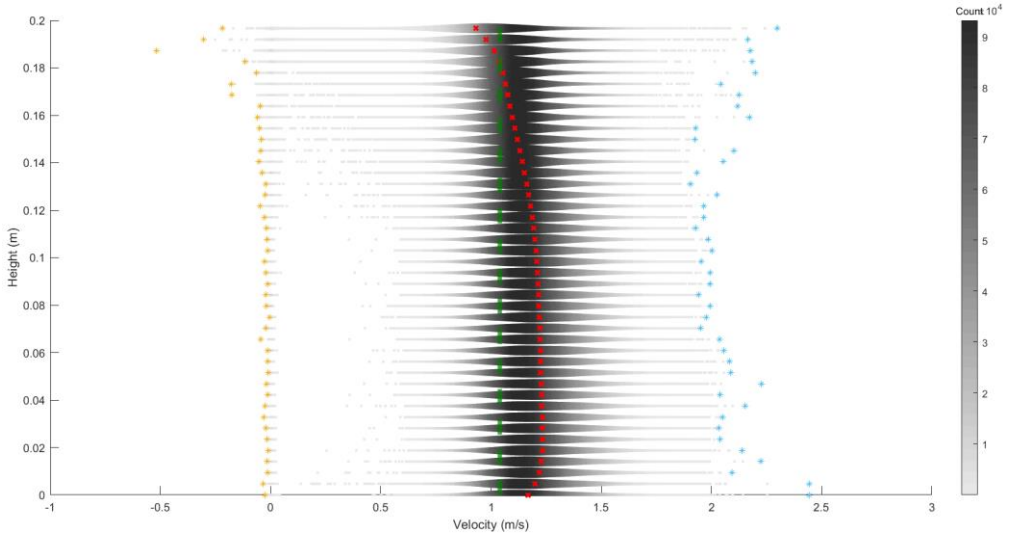
Count 10^4
9
8
7
6
5
4
3
2
1
Height (m)
0.2
0.18
0.16
0.14
0.12
0.1
0.08
0.06
0.04
0.02
0
-1
-0.5
0
0.5
1
1.5
2
2.5
3
Velocity (m/s)

(b)

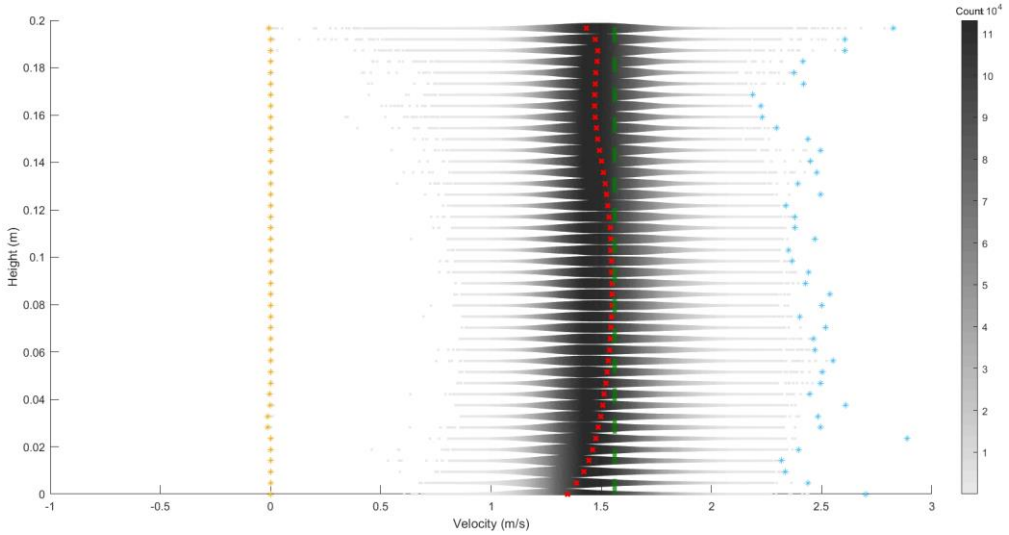

(c)

Figure 4- 4. Swarm plot with histogram counts of the velocity data for the one (a), two (b) and three (c) working fans. Yellow, blue and red markers indicate minimum, maximum and averaged values of each height level, respectively. The dashed green lines show the wind velocities produced by the wind generator, calculated based on the specifications of the fans.

In Figure 4- 5, related swarm plots to the PIV measurement data of water velocity are provided. These profiles refer to the experiments 5, 6 and 7 in Table 3- 1. The origin coordinate for the water field is shown in Figure 3- 9. The water surface level is located at 0 m, and the negative values represent the distance from water surface elevation. Description of the plots is the same as that presented for Figure 4- 4. For the three wind fields, small water velocity values were observed that shows the water fields were under marginal effects of the wind fields. Although, the increasing number of working fans, increases the velocity values to a marginal extent. The maximum averaged values for the three, two and one working fans were 0.035, 0.0052 and 0.0049 m/s, respectively. The negative velocity results in water fields shows the effect of negative wind velocity values on the water fields.

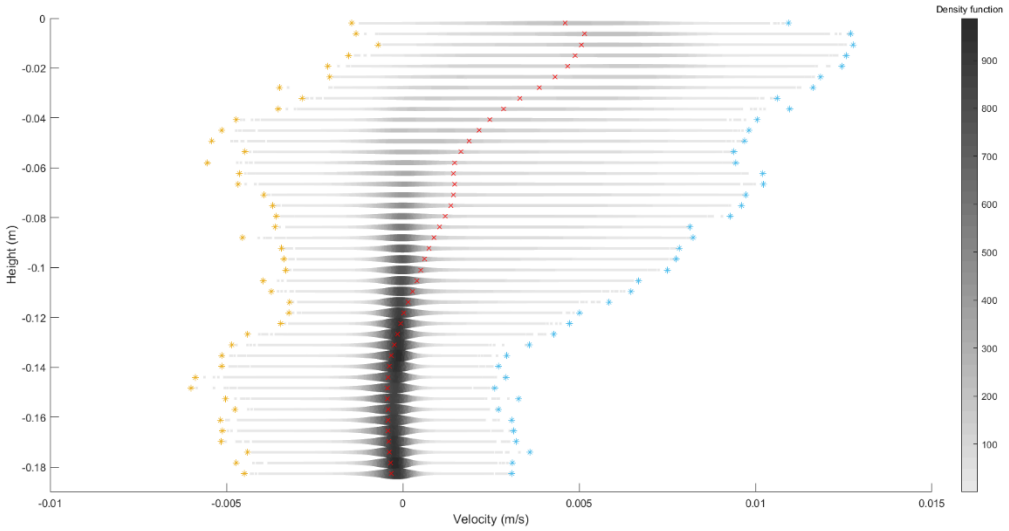
Density function
Height (m)
Velocity (m/s)

(a)

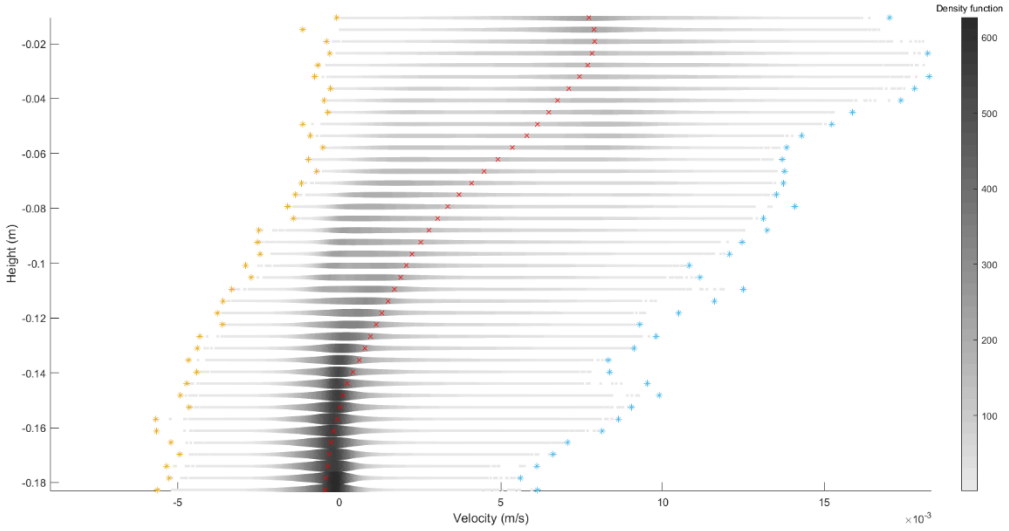
Density function
Height (m)
Velocity (m/s)

(b)

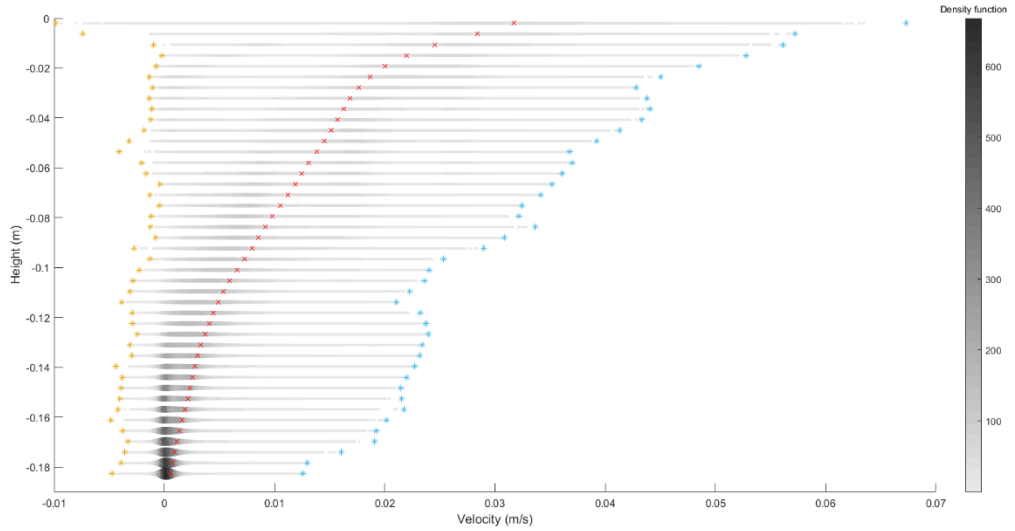

(c)

Figure 4- 5. Water velocity profiles along the height of the flume, for the one (a), two (b) and three (c) working fans.

Figure 4- 6 shows the standard deviation for the calculated velocities in the three water fields. The same description of the plots is provided for Figure 4- 2, and Eq.4-1 is used for the error calculation in Figure 4- 6. The calculated errors for the average velocities show marginal values which indicate accuracy in the calculation.

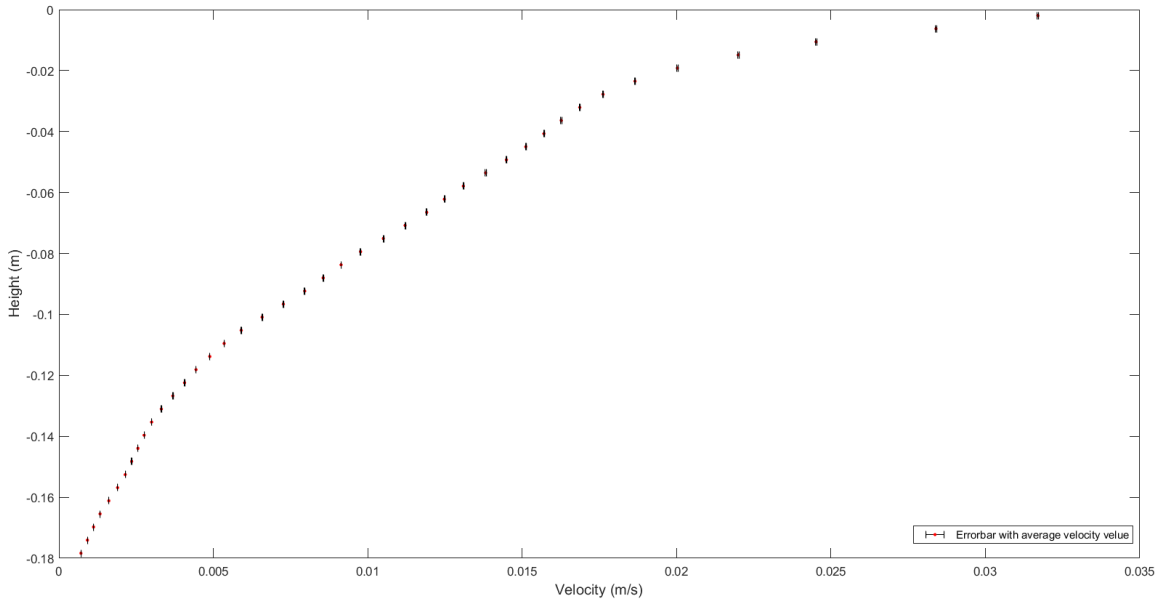

(a)

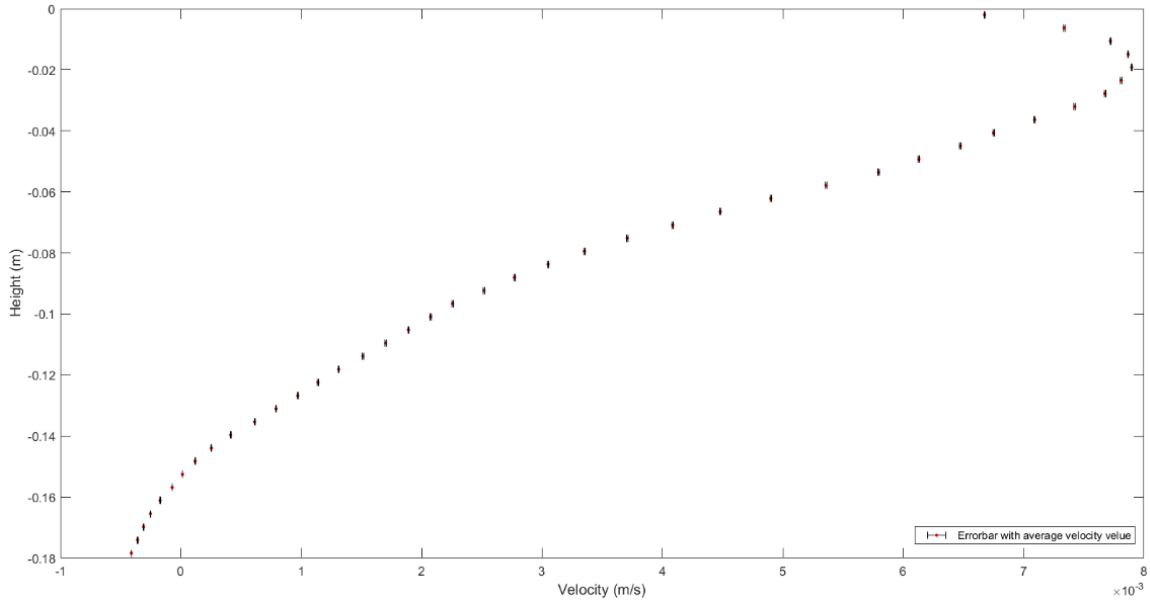

(b)

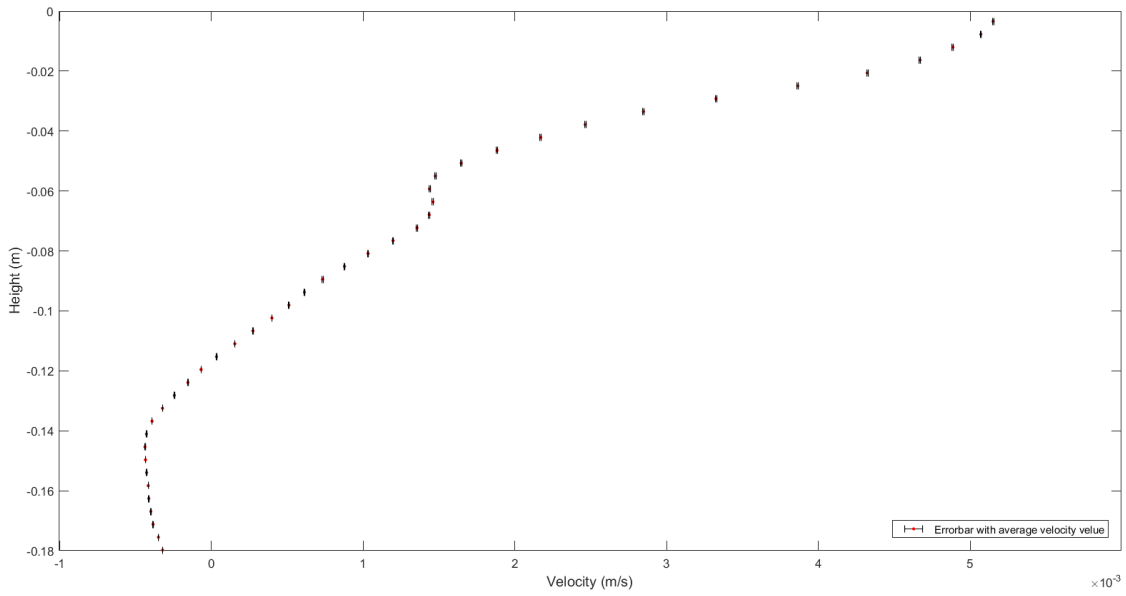

(c)

Figure 4- 6. The standard deviation of water velocity values along the height of the flume for the one (a), two (b) and three (c) working fans.

4.2 Verification of the PIV wind field velocity measurement with the anemometer device

For verification of the wind velocity measurement with the PIV technique, using water particles as the seeding material, wind velocity was measured with an intrusive device (the device was located in the wind field), specifically MiniWater20 Micro anemometer by Omni Instruments. Vertical profiles were recorded at the midsection of the measurement window

and half-width of the flume (Figure 3- 9). These experiments which were performed using the anemometer device, are numbered 8, 9 and 10 in Table 3- 1. The same measurements were not performed for the water fields, due to the marginal water velocity values which were not possible to record with the anemometer device. The applied prob for intrusive velocimetry should not occupy a large volume of the test field, which seemed satisfactory for this study. To this aim, vertical velocity profiles were obtained for different wind fields.

The dedicated measurement point was at the centre of the measurement window, 0.7 m from the spray nozzles. Figure 4- 7 shows the obtained wind velocity profiles with the anemometer device. The maximum values for the average velocities generated by the three, two and one working fans were 1.27, 0.92 and 0.52 m/s, respectively. By changing the wind field and increasing the wind velocity from one fan to three fans, the maximum average value occurs at a higher distance from the coordinate origin (Figure 3- 9). The three graphs in this figure show curved shapes with minimum values near the ceiling of the flume and relatively higher values close to the water surface.

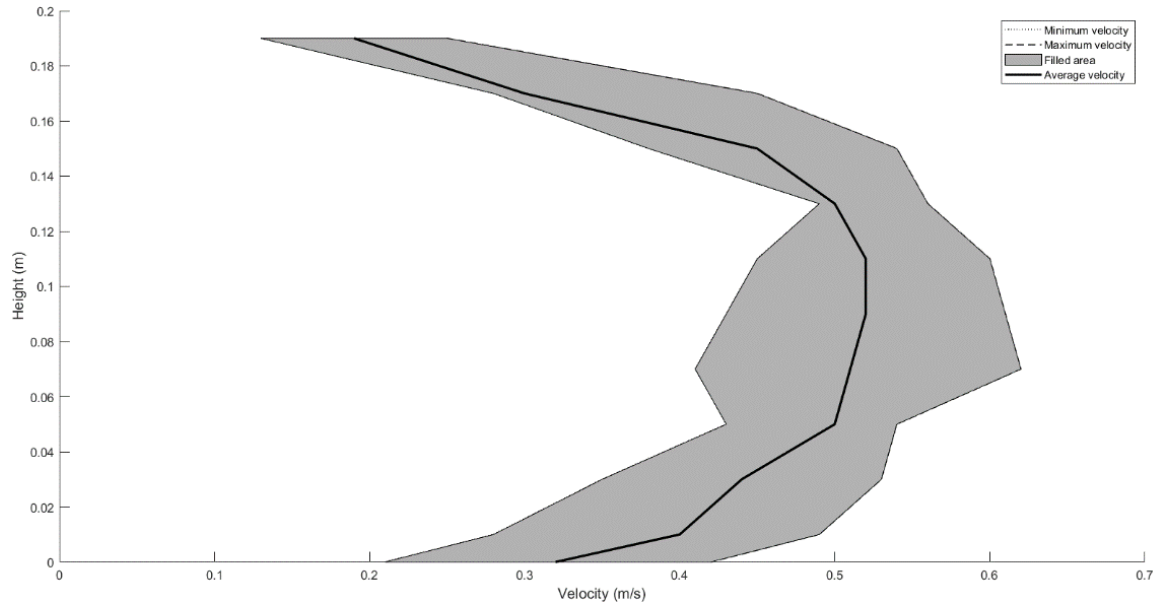

(a)

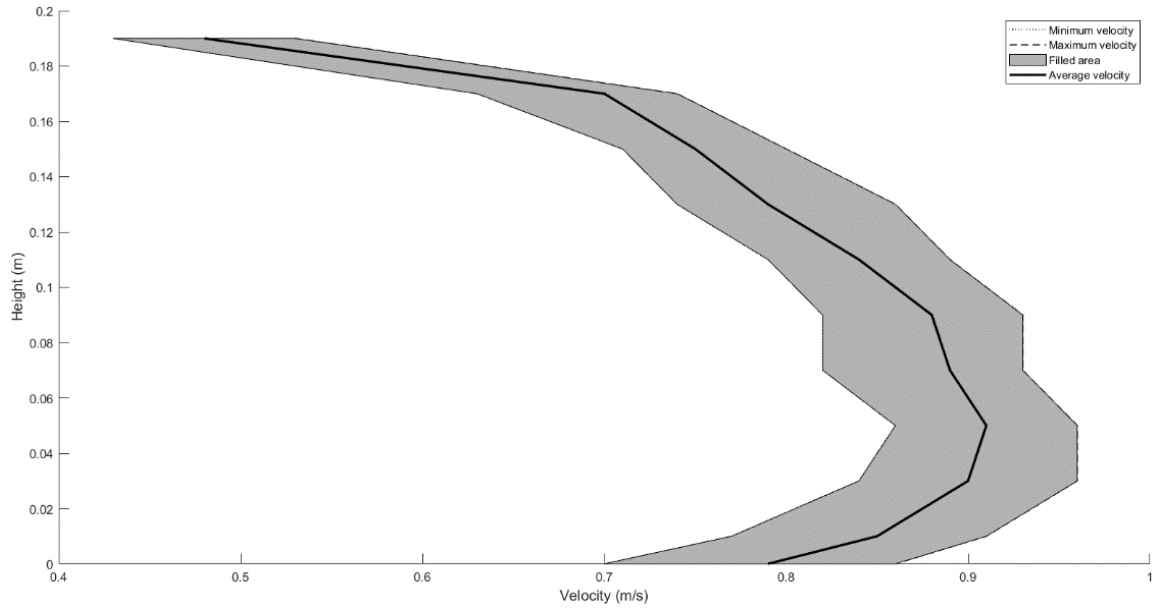

(b)

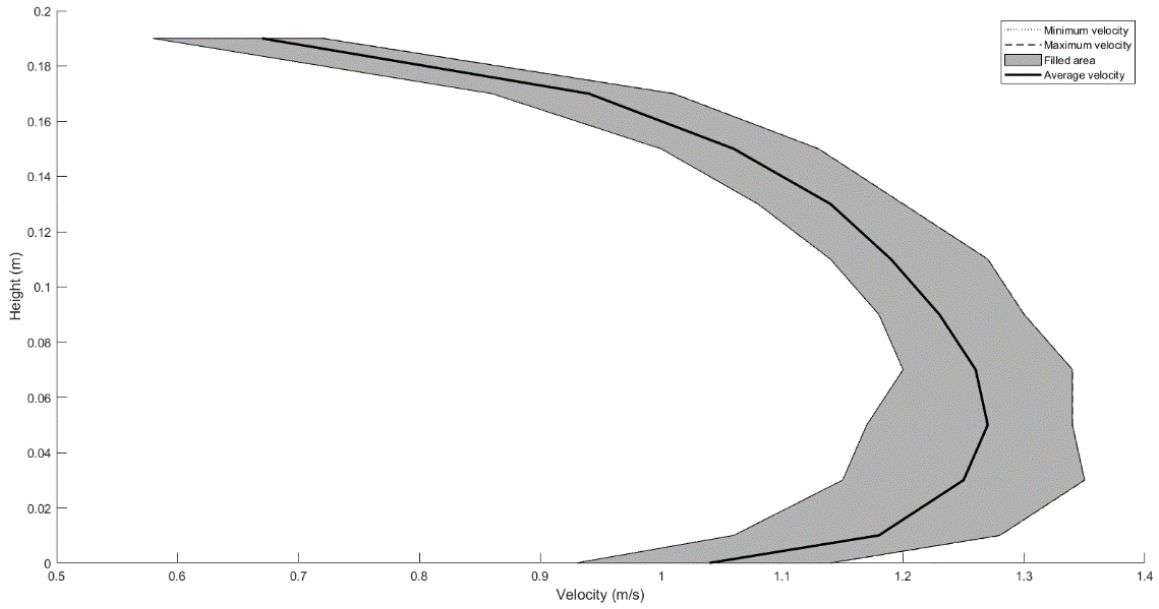

(c)

Figure 4- 7. Averaged wind velocity profiles along the height of the flume, obtained from measurement with the MiniWater20 Micro anemometer device, for one (a), two (b) and three (c) working fans.

The comparison between the wind velocity measurements using PIV technique and MiniWater20 Micro anemometer device can be seen in Figure 4- 4 and Figure 4- 7. The anemometer device outputs a range of measurement values, including minimum, maximum and average velocities for each measuring point (height level) of a velocity profile. However, the PIV technique's velocity profiles for each measuring height level are based on a large number of measurements in the x direction. The average velocity profile from the PIV technique measurement (red markers in Figure 4- 4) shows less variations across the height of the wind field compared to the average velocity profile from anemometer device.

Additionally, wider ranges of velocity values were obtained from PIV technique at each height level. The averaged values of the velocity profiles from the PIV technique are 0.514, 1.165 and 1.499 m/s for one, two and three working fans, respectively. The averaged values from the anemometer device are 0.422, 0.798 and 1.111 m/s, respectively. This indicates that, the obtained results from both invasive and non-invasive methods are closed to each other.

4.3 PTV measurement related to the ice velocity

To begin with, for the analysis of PTV measurement results, two approaches based on the selection of the measuring section are considered. The first approach confines the measurement area to the vicinity of the PIV measurement location, considering only the adjacent area around the section for PIV measurement. The second approach considers the entire measurement field.

Based on the Table 3- 3, the velocity measurements for ice pieces and covers correspond to the experiments 1 to 3 and 4 to 6, respectively. As mentioned earlier, the averaged velocities of the ice pieces and covers were obtained from areas (averaged area velocity) around the location of the PIV measurement (considering the area for PTV calculation of ice velocity at the location of the PIV measurement for wind velocity). The concentration of the ice pieces was determined by counting the pieces in the observation area of one meter length (1×0.6 m area, Figure 3- 25). The number of ice pieces indicates the total area of the ice (the surface area of one piece in the experiments was 0.01 m^2), which was used in the concentration value calculation indicated in Eq. 4-2 The number of pieces relates to the ice concentration type and range used for this study. Three concentration ranges—low, medium and high—were considered and are provided in Table 4- 1. From each experiment (Table 3- 3), the three concentration ranges were extracted, and the velocity of ice was calculated using the PTV technique.

Table 4- 1. Ice concentration ranges used in this study, based on the number of ice pieces.

Ice concentration type	Ice concentration Value	The number of ice pieces
Low	0-0.35	0-20
Medium	0.35-0.7	21-41
High	0.7-1	41-59

$$concentration\ value = \frac{Total\ area\ of\ the\ ice}{Observation\ area\ of\ water\ surface} = \frac{Total\ area\ of\ the\ ice}{1 \times 0.6\ m^2} \quad \text{Eq.4- 2}$$

The averaged ice area velocities for different ice concentrations (low, medium and high) and each repeating experiment (experimental trial) are shown in Figure 4- 8. As mentioned before and can be seen in Figure 4- 8, there are three trials whose averaged ice area velocities are shown in a red hue (except for the Figure 4- 8 (b), in which there are two repetitions for low and medium ice concentrations). The calculations were also repeated for different wind velocity fields and ice concentrations. A considerable relation between the ice concentration and ice velocity was not observed. However, taking the averaged values of the experimental trials (black bars in Figure 4- 8) into account, the lower concentrations lead to higher velocities. The ranges of average velocities (black bars) for the wind fields of one, two and three working fans are 0.019 to 0.026, 0.029 to 0.035 and 0.035 to 0.041 m/s, respectively. It can be noticed that less variation in the averaged ice area velocities is observed with the wind field of two working fans. Shen et al, (1990) related the interaction of the particles (ice) to their concentration and the time duration of their interaction, and consequently to the ice flow regime (Shen et al., 1990). They mentioned the low and high concentrations typically occur in high and low ice velocity, respectively. Which can be called rapid and slow flow regimes, respectively (Shen et al., 1990). From Figure 4- 8, it can be seen that the averaged ice velocity (black bars) usually decreases with increasing ice concentration.

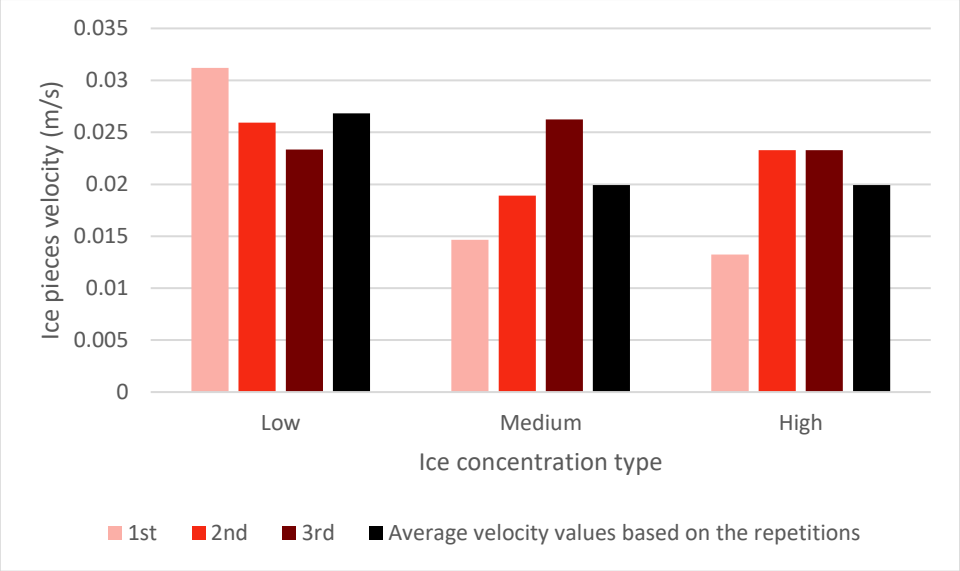
0.035
0.03
0.025
0.02
0.015
0.01
0.005
0
Ice pieces velocity (m/s)
Low
Medium
High
Ice concentration type
1st
2nd
3rd
Average velocity values based on the repetitions

(a)

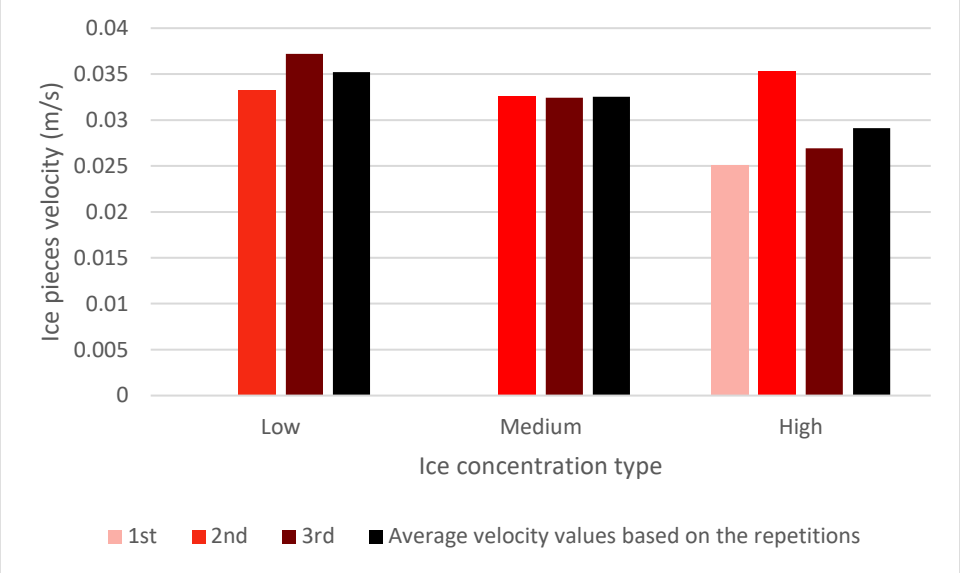
0.04
0.035
0.03
0.025
0.02
0.015
0.01
0.005
0
Ice pieces velocity (m/s)
Low
Medium
High
Ice concentration type
1st
2nd
3rd
Average velocity values based on the repetitions

(b)

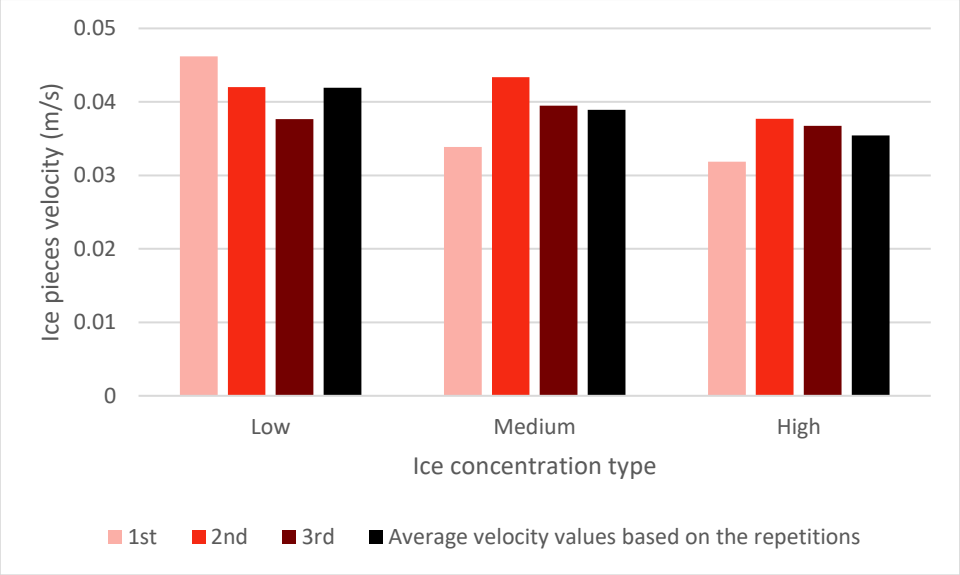

(c)

Figure 4- 8. The averaged ice area velocity for ice pieces under the wind fields with one (a), two (b) and three (c) working fans.

In Figure 4- 9, the averaged ice area velocity for the covers for three experimental trials (in red hue) and their averaged values (black bars) are shown. As mentioned before, the ice covers showed movements under the wind effect of two and three working fans. Therefore, the ice velocities related to these two wind fields are shown. As can be seen in the figure, the average velocities of the three trials related to the two and three working fans are 0.0195 and 0.0265 m/s, respectively. As might be expected, the ice concentration is not relevant for the covers.

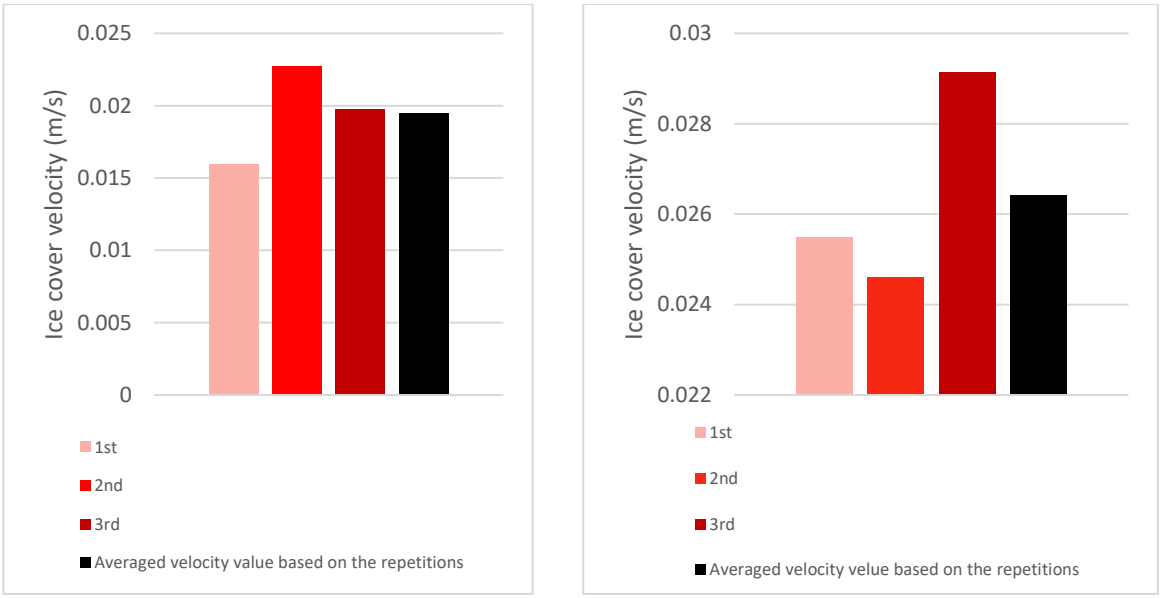

(a) (b)

Figure 4- 9. The averaged ice area velocity for covers under the wind fields with one (a), two (a) and three (b) working fans.

After obtaining the velocity results from PTVlab software, it was decided to perform data analysis (Figure 4- 8 and Figure 4- 9); the test was conducted using the entire measurement field. The aim was to determine whether using a limited area or the entire measurement field provides better ice velocity results.

There were different sets of data which included the number of working fans, repetitions of the experiments (1st, 2nd and 3rd, as mentioned in the description of Figure 4- 8) and the concentration description (low, medium, and high). The ice velocity fields were the output of PTVlab software (ASCII file) and referred to the measurement domain at each time step (snapshot). The snapshots were obtained by extracting images from videos, which would give one set of data.

The videos for each data set (derived videos) were obtained from an extended video relating to one wind velocity field but containing three concentration types (Table 4- 1). Therefore, the three different concentration types were captured from each extended video. As mentioned before, there are three repeating experiments under the influence of each wind velocity field and concentration, each of which indicates a different run (set of data). The timings of the runs started from zero. The formulation for the time step is as follows.

$$Time\ step\ (s) = \frac{The\ time\ extension\ of\ derive\ video}{number\ of\ obtained\ snapsots} \qquad \text{Eq. 4- 3}$$

The time step varied between 33 to 34 ms, based on the time extension of a derived video and the number of snapshots. A MATLAB code was developed to handle the data from ASCII files for different ice concentrations and wind velocities. The ice velocities for different conditions were obtained for all the coordinates of the domain. For each specific ice concentration and wind velocity as well as corresponding repeating experiments, the averaged ice velocities for each coordinate were obtained over the experiment times. Data grouping for the PTV analysis was done to provide access to all the data separately for each wind velocity, ice concentration and order of repeating experiments in an SQLite database.

Examples of ice velocity vector fields are provided in Figure 4- 10. The resulting histograms for longitudinal (u) and transverse (v) velocities are shown in Figure 4- 11 to Figure 4- 19. The velocities are ranged in groups of 0.005 m/s. In these figures the velocity values with the corresponding number of repeating values are illustrated on the z-axis of the histograms. Each Figure relates to one wind field.

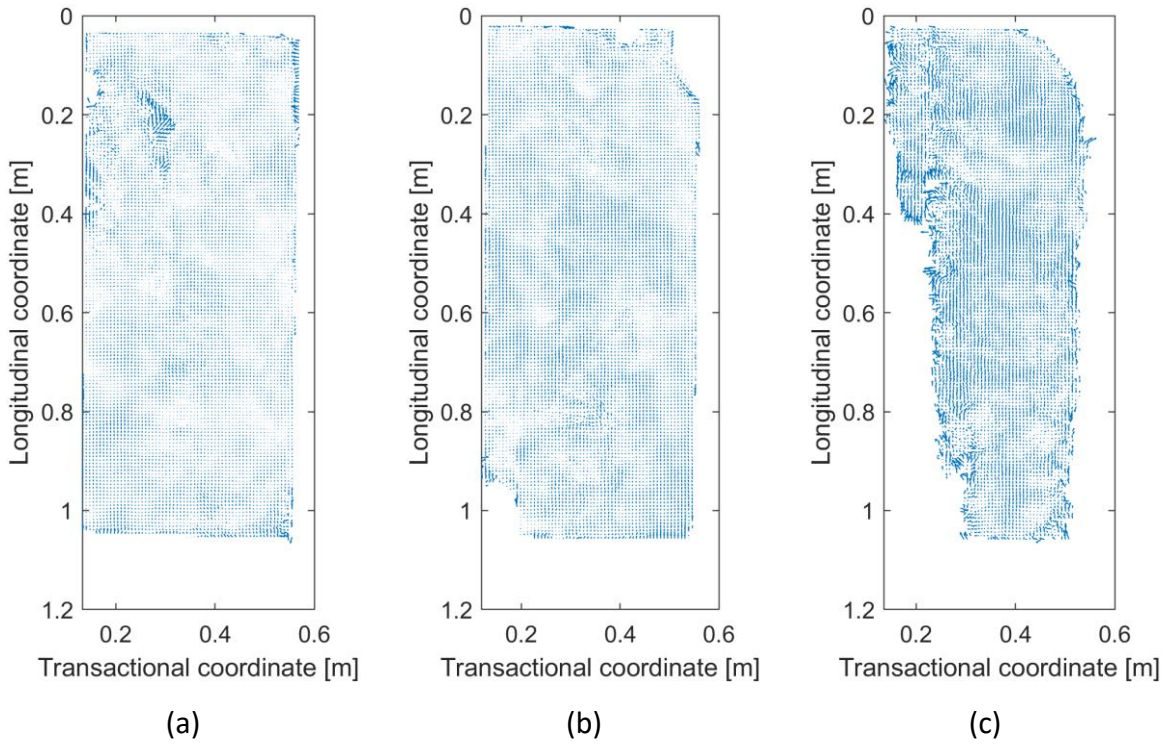

Figure 4- 10. Velocity vector fields for high concentration (a), medium concentration (b) and low concentration (c).

As can be seen in Figure 4- 11 to Figure 4- 13, which relate to the high concentration of ice, the longitudinal (u) and transverse (v) ice velocities are shown. The lengths of the bars in the u and v-axis directions are 0.005 m/s, which represents the sizes of the velocity groups. These graphs correspond to the cases with one, two and three working fans. In this study, the longitudinal velocity of the ice is considered, which defines the movement of the ice along this direction in the flume. This is the same direction used to measure the wind velocity, meaning both ice and wind velocities share the same direction.

Each figure, corresponding to a different wind field, contains subplots (a), (b) and (c) representing the 1st, 2nd and 3rd trials, respectively. The bars in these histograms represent velocity ranges, while the z-axis indicates the frequency or repetition of each range. The maximum frequency range (the bar with the greatest height along the z-axis) was calculated using MATLAB and represent the ice velocity for each wind field and ice concentration.

For high ice concentration, the longitudinal velocity ranges for the wind field generated by one working fan during the 1st, 2nd and 3rd repeating experiments are 0.01-0.015, 0.015-0.02 and 0.02-0.025 m/s. It can be observed that the repeated experiments under the same conditions show slight variations in the ice velocity ranges. The average ice velocity across these ranges is 0.017 m/s, indicating a relatively small effect of low wind velocity (0.515 m/s) on ice pieces. This may be due to the limited influence of low wind velocity and the large mass of ice, which leads to increased interaction between ice pieces in high concentration. In this model, the ice surface is smooth, therefore, the wind tension on ice is reduced to the mutual interaction among ice pieces. The proportion of the wind force imposed on the ice is related to the resistance between the ice pieces and the ice concentration.

Similarly, the ice velocity ranges for two working fans are 0.025-0.03, 0.03-0.035 and 0.025-0.03 m/s, and for three working fans are 0.03-0.035, 0.04-0.045 and 0.035-0.04 m/s.

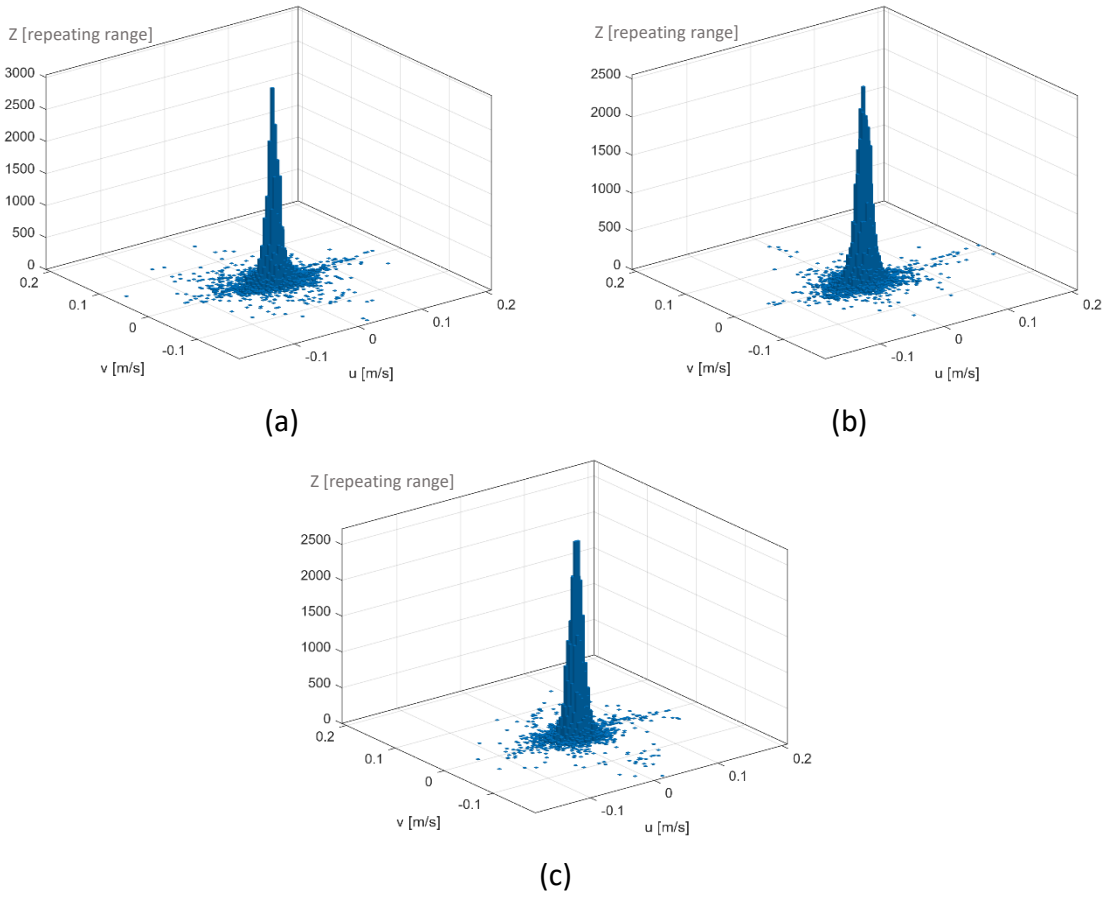

Figure 4- 11. Horizontal (u) and vertical (v) velocities of ice pieces for high ice concentration and wind field with one working fan for the 1st (a), 2nd (b), and 3rd (c) repeated experiments with the counting number (z-axis).

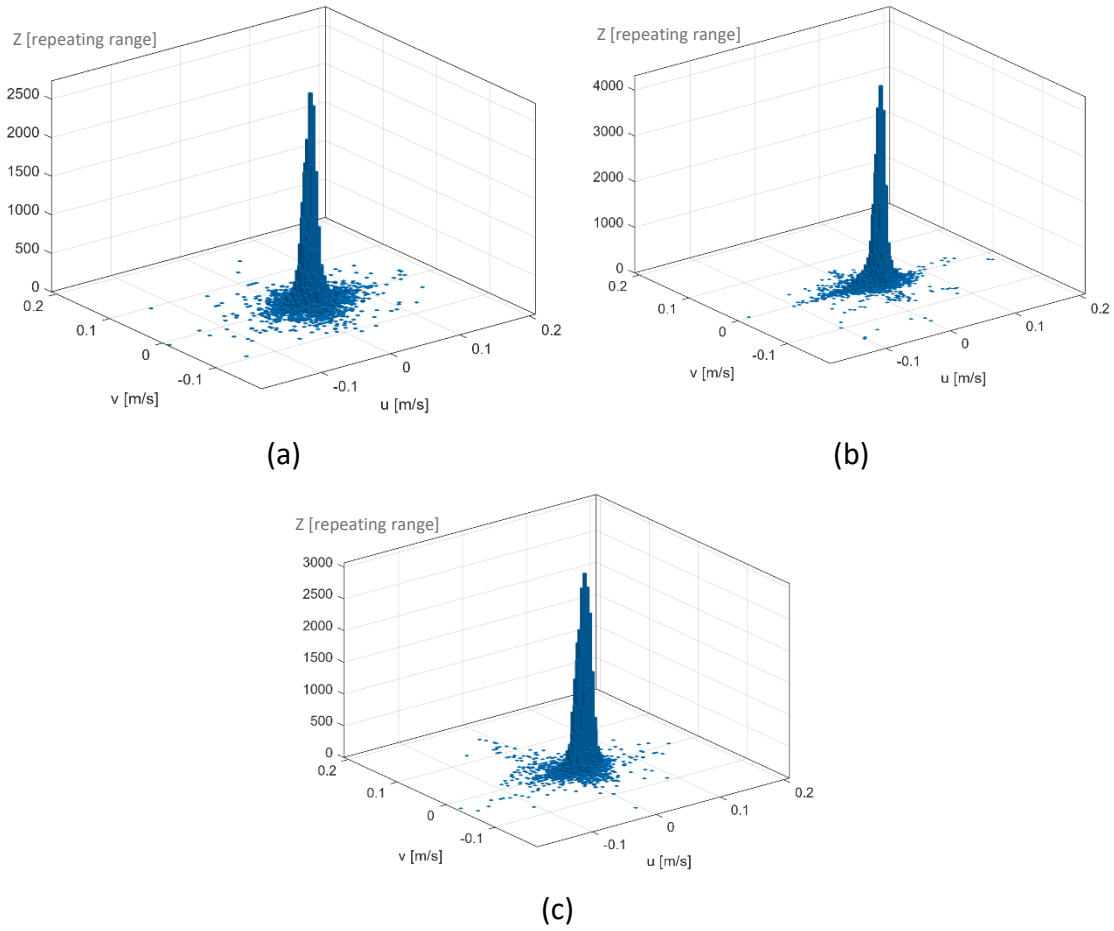

Figure 4- 12. Horizontal (u) and vertical (v) velocities of ice pieces for high ice concentration and wind field with two working fans for the 1st (a), 2nd (b), and 3rd (c) repeated experiments with the counting number (z-axis).

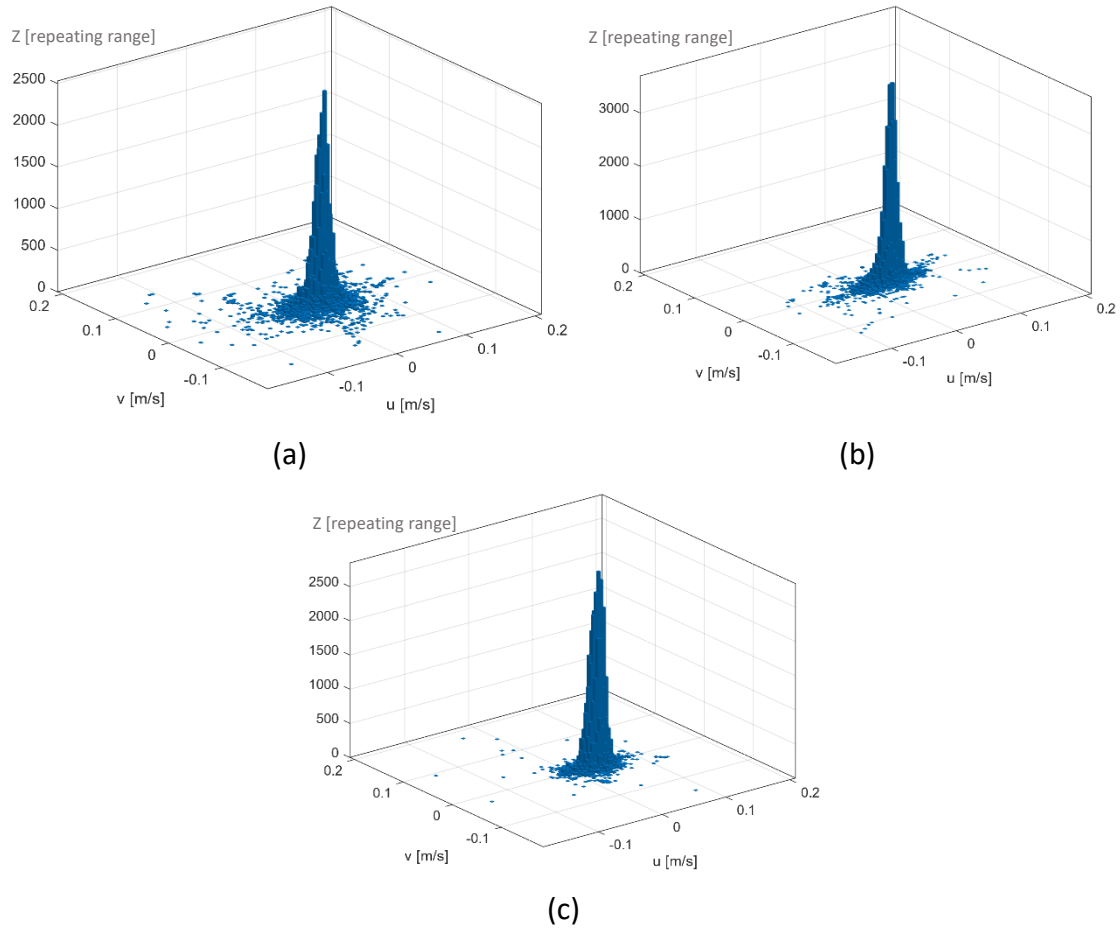

Figure 4- 13. Horizontal (u) and vertical (v) velocities of ice pieces for high ice concentration and wind field with three working fans for the 1st (a), 2nd (b), and 3rd (c) repeated experiments with the counting number (z-axis).

In Figure 4- 14 to Figure 4- 16, the ice velocity histograms related to the medium ice concentration for one, two and three working fans are provided. The same description for Figure 4- 11 to Figure 4- 13 can be applied for these figures, except for the changed concentration. For the medium ice concentration and two working fans two valid experiments were recorded. Generally, for the medium ice concentration, more scattered values for the ice velocity ranges can be observed. The most frequently occurring longitudinal ice velocity ranges for one working fan in the 1st, 2nd and 3rd repeating experiments are 0.01-0.015, 0.01-0.015 and 0.015-0.02 m/s. For two working fans in the 2nd and 3rd repeating experiments, the ranges are 0.02-0.025 and 0.025-0.03 m/s. For three working fans, the velocity ranges for the 1st to 3rd trials are 0.02-0.025, 0.035-0.04 and 0.04-0.045 m/s. As can be observed, with an increase in the number of operating fans, the velocity range also increases. The rise in ice velocity ranges under the influence of two to three working fans is greater than that observed from one to two working fans.

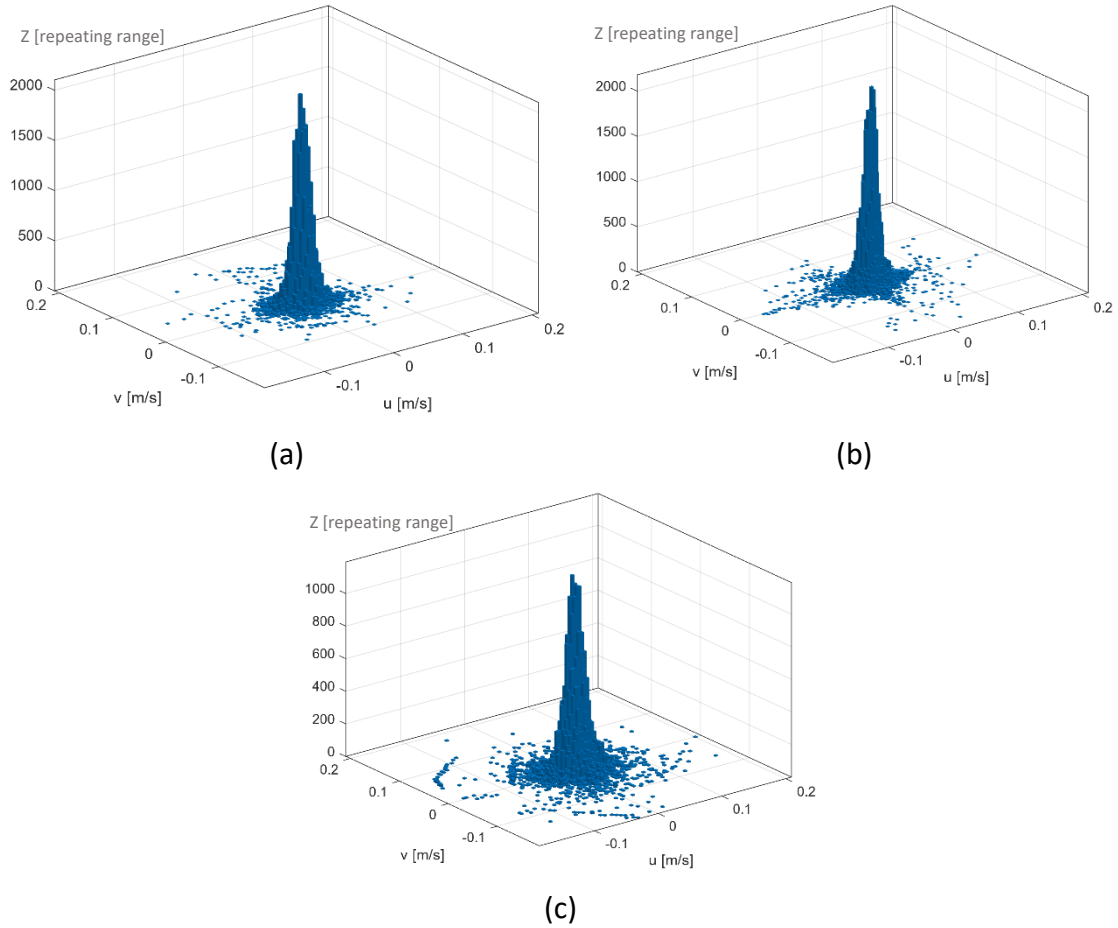

Figure 4- 14. Horizontal (u) and vertical (v) velocities of ice pieces for medium ice concentration and wind field with one working fan for the 1st (a), 2nd (b), and 3rd (c) repeated experiments with the counting number (z-axis).

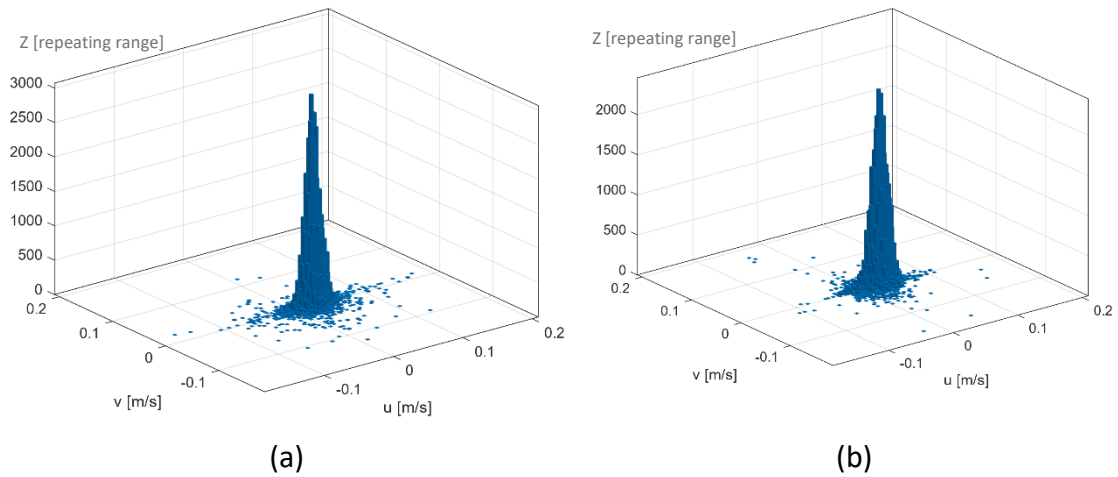

Figure 4- 15. Horizontal (u) and vertical (v) velocities of ice pieces for medium ice concentration and wind field with two working fans for the 2nd (a), and 3rd (b) repeated experiments with the counting number (z- axis).

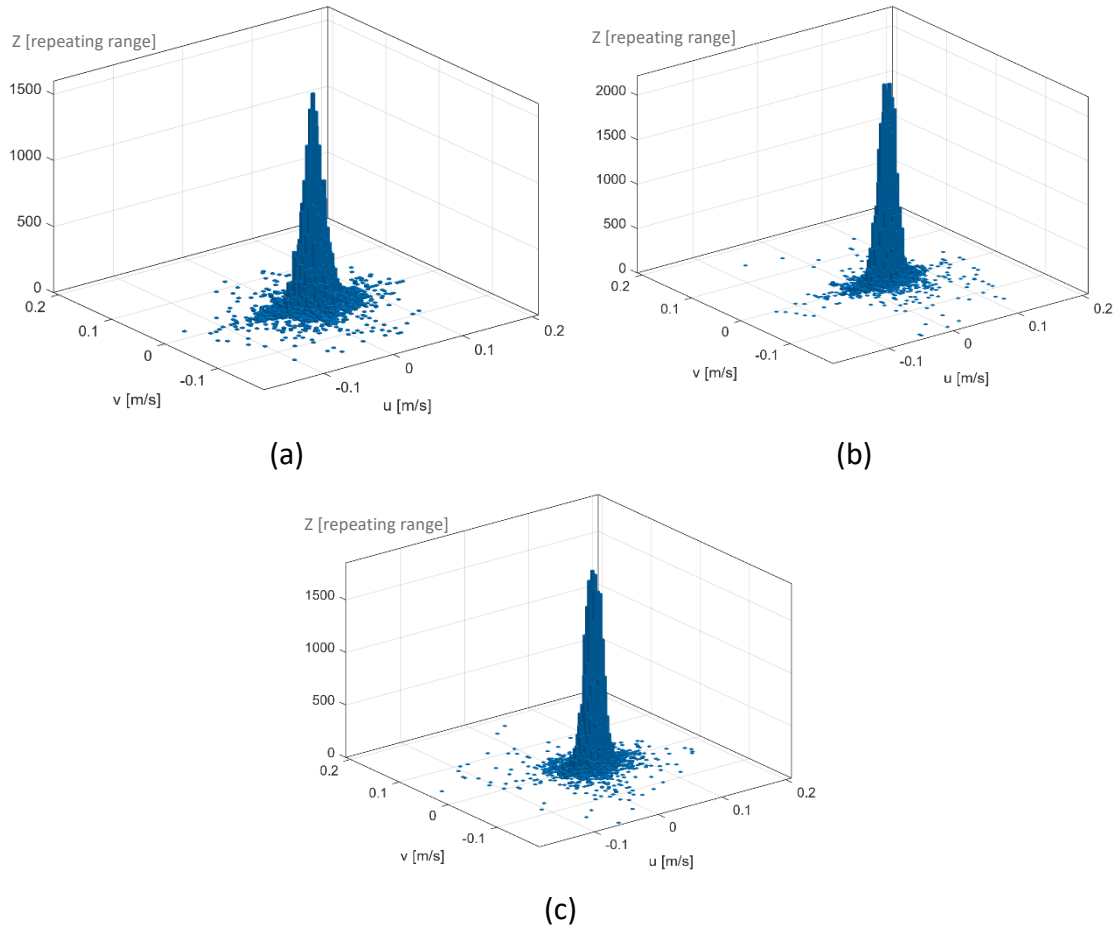

Figure 4- 16. Horizontal (u) and vertical (v) velocities of ice pieces for medium ice concentration and wind field with three working fans for the 1st (a), 2nd (b), and 3rd (c) repeated experiments with the counting number (z-axis).

In Figure 4- 17 to Figure 4- 19, the ice velocity related to the low concentration of ice is shown. Two valid experiments were repeated related to the wind field of two working fans. The longitudinal velocity ranges for the one working fan in 1st, 2nd and 3rd repeating experiments are 0.01-0.015, 0-0.005 and 0.01-0.015 m/s. Following the same order of repeated experiments, the longitudinal velocity ranges for the wind fields generated by two and three working fans are 0.025-0.03 and 0.025-0.03 m/s (for the 2nd and 3rd repetitions for two working fans) and 0.03-0.035, 0.035-0.04 and 0.035-0.04 m/s (in the 2nd and 3rd repetitions for three working fans), respectively. Generally, in each histogram for the low ice concentration, the velocity ranges appear less scattered. This is because the low ice concentration contains fewer ice pieces in the ice velocity field.

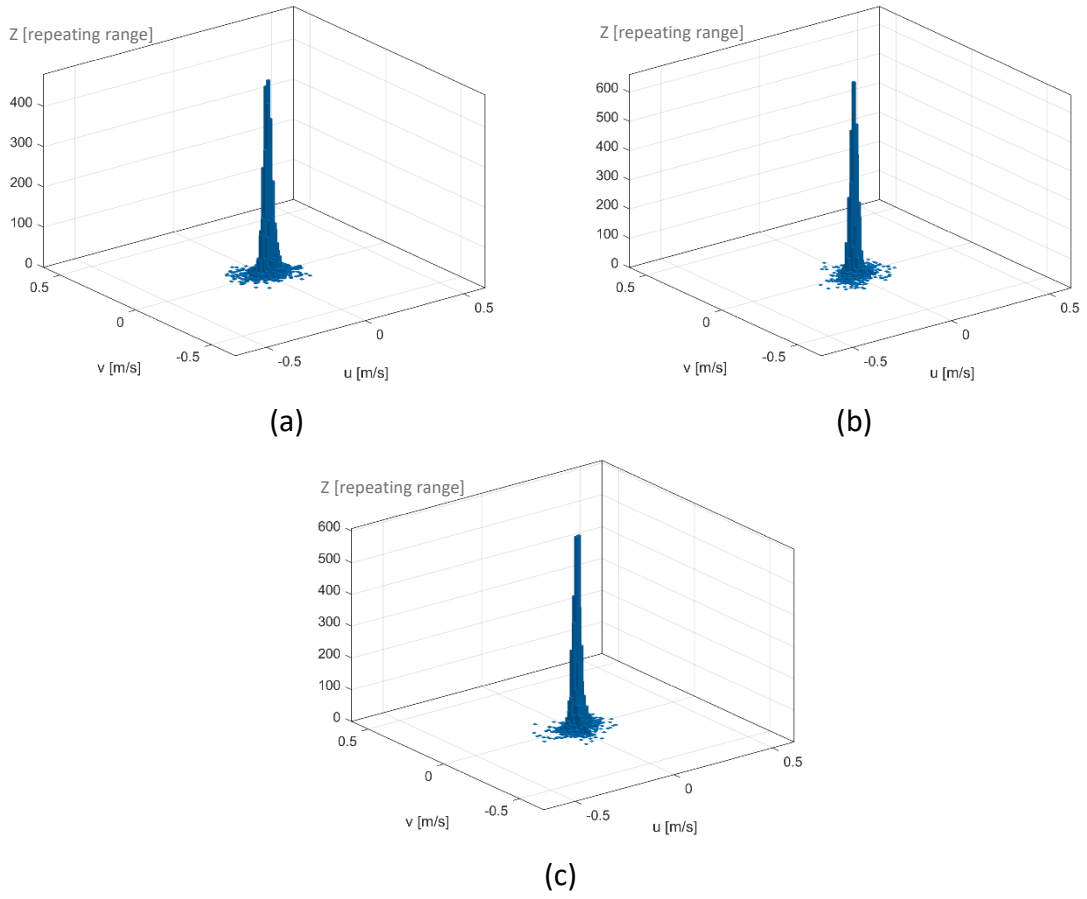

Figure 4- 17. Horizontal (u) and vertical (v) velocities of ice pieces for low ice concentration and wind field with one working fan for the 1st (a), 2nd (b), and 3rd (c) repeated experiments with the counting number (z-axis).

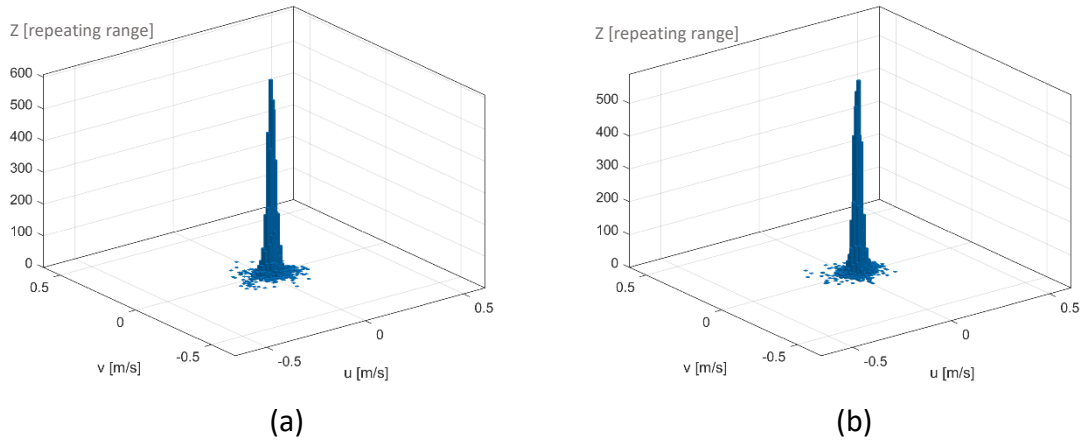

Figure 4- 18. Horizontal (u) and vertical (v) velocities of ice pieces for low ice concentration and wind field with two working fans for the 2nd (a), and 3rd (b) repeated experiments with the counting number (z-axis).

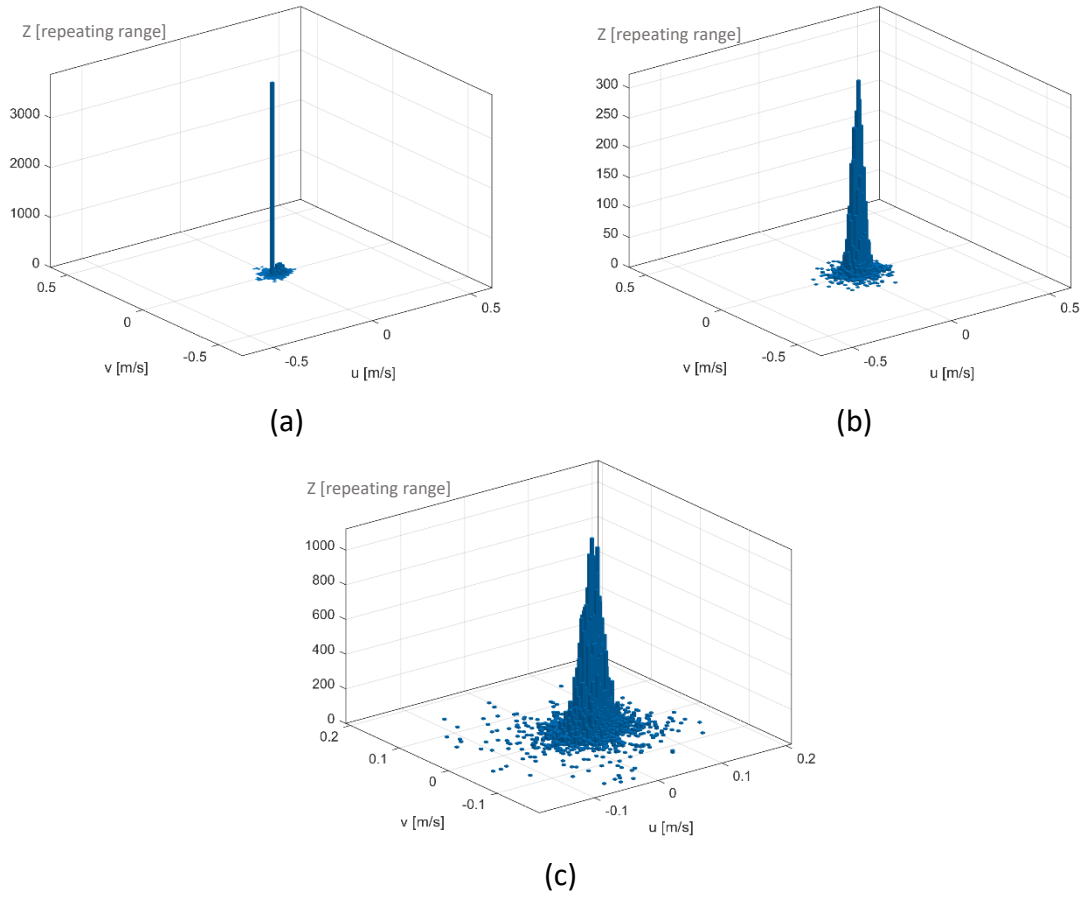

Figure 4- 19. Horizontal (u) and vertical (v) velocities of ice pieces for low ice concentration and wind field with two working fans for the 1st (a), 2nd (b), and 3rd (c) repeated experiments with the counting number (z-axis).

In Table 4- 2, the most repeated longitudinal ice velocity ranges (in 0.005 m/s) for the different experiments related to the ice pieces are presented. The values are related to Figure 4- 11 to Figure 4- 19.

Table 4- 2. The maximum repeating ranges of the longitudinal velocity of ice pieces for different experiments.

Experiment type for ice pieces based on the wind field, ice concentration and repeating experiment	**Maximum repeating range of ice pieces velocity (m/s)**
One working fan, high ice concentration and 1st repeated experiment	0.01-0.015
One working fan, high ice concentration and 2nd repeated experiment	0.015-0.02
One working fan, high ice concentration and 3rd repeated experiment	0.02-0.025
Two working fans, high ice concentration and 1st repeated experiment	0.025-0.03
Two working fans, high ice concentration and 2nd repeated experiment	0.03-0.035
Two working fans, high ice concentration and 3rd repeated experiment	0.025-0.03
Three working fans, high ice concentration and 1st repeated experiment	0.03-0.035
Three working fans, high ice concentration and 2nd repeated experiment	0.04-0.045
Three working fans, high ice concentration and 3rd repeated experiment	0.035-0.04
One working fan, medium ice concentration and 1st repeated experiment	0.01-0.015
One working fan, medium ice concentration and 2nd repeated experiment	0.01-0.015
One working fan, medium ice concentration and 3rd repeated experiment	0.015-0.02
Two working fans, medium ice concentration and 2nd repeated experiment	0.02-0.025
Two working fans, medium ice concentration and 3rd repeated experiment	0.025-0.03
Three working fans, medium ice concentration and 1st repeated experiment	0.02-0.025
Three working fans, medium ice concentration and 2nd repeated experiment	0.035-0.04
Three working fans, medium ice concentration and 3rd repeated experiment	0.04-0.045
One working fan, low ice concentration and 1st repeated experiment	0.01-0.015
One working fan, low ice concentration and 2nd repeated experiment	0-0.005
One working fan, low ice concentration and 3rd repeated experiment	0.01-0.015
Two working fans, low ice concentration and 2nd repeated experiment	0.025-0.03
Two working fans, low ice concentration and 3rd repeated experiment	0.025-0.03
Three working fans, low ice concentration and 1st repeated experiment	0.03-0.035
Three working fans, low ice concentration and 2nd repeated experiment	0.035-0.04
Three working fans, low ice concentration and 3rd repeated experiment	0.035-0.04

Based on the complete velocity data for ice pieces under each wind field, it can be concluded that varying ice concentration did not significantly affect the ice velocity results across the entire measurement field.

The horizontal and transverse velocity values for ice cover, along with the count of the repetitions are provided in Figure 4- 20 and Figure 4- 21. The same description provided for Figure 4- 11 to Figure 4- 13 can be applied for these figures. Table 4- 3 shows the ranges (in 0.005 m/s) for the most frequently occurring values of longitudinal ice cover velocity. For the ice cover under the influence of one working fan, zero velocity was observed. As can be seen, increasing the number of operating fans generally increases the ice velocity, except for one

experiment where the same velocity ranges were observed under the influence of both two and three working fans.

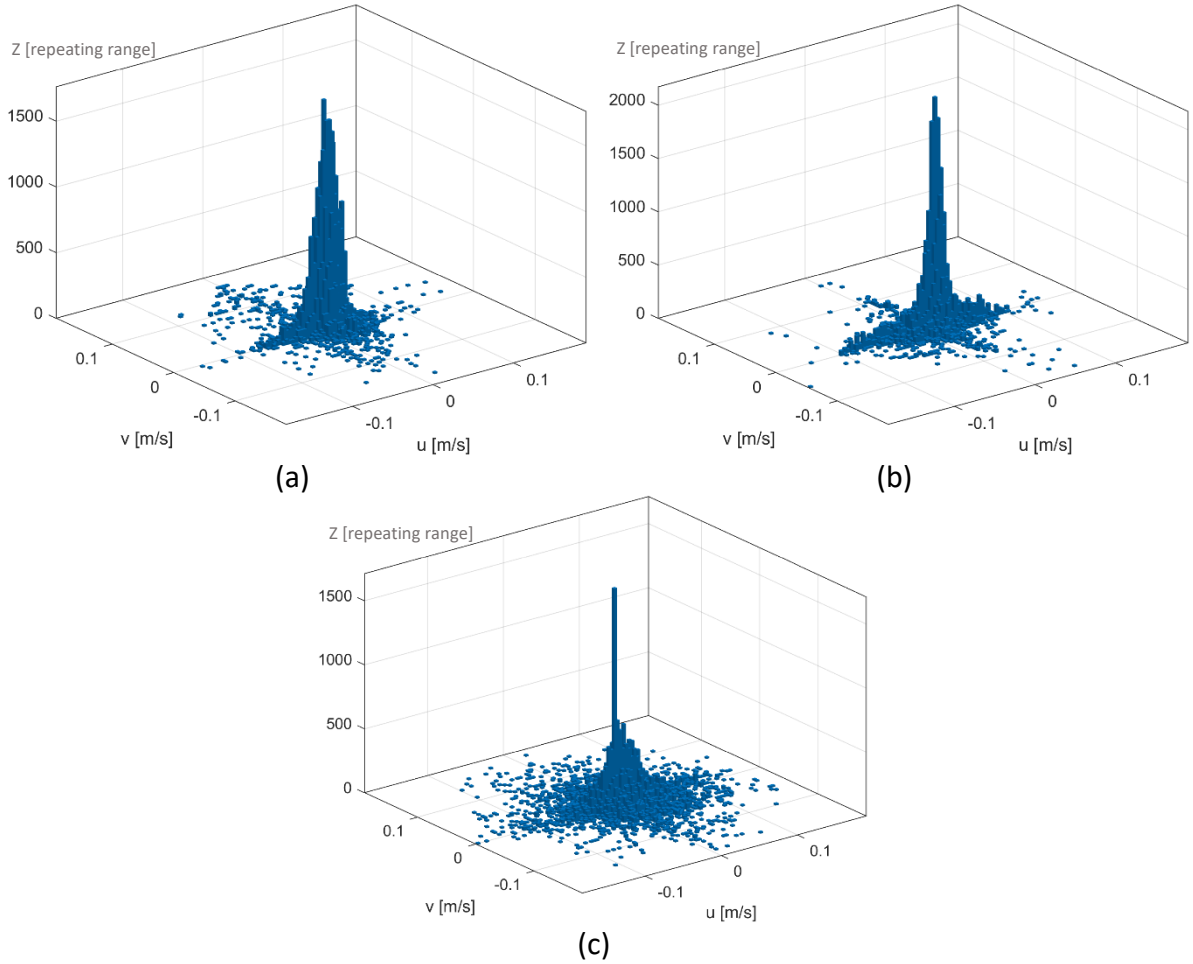

Figure 4- 20. Horizontal (u) and vertical (v) velocities for ice cover and one working fan for the 1st (a), 2nd (b) and 3rd (c) repeated experiments with counting number (z-axis).

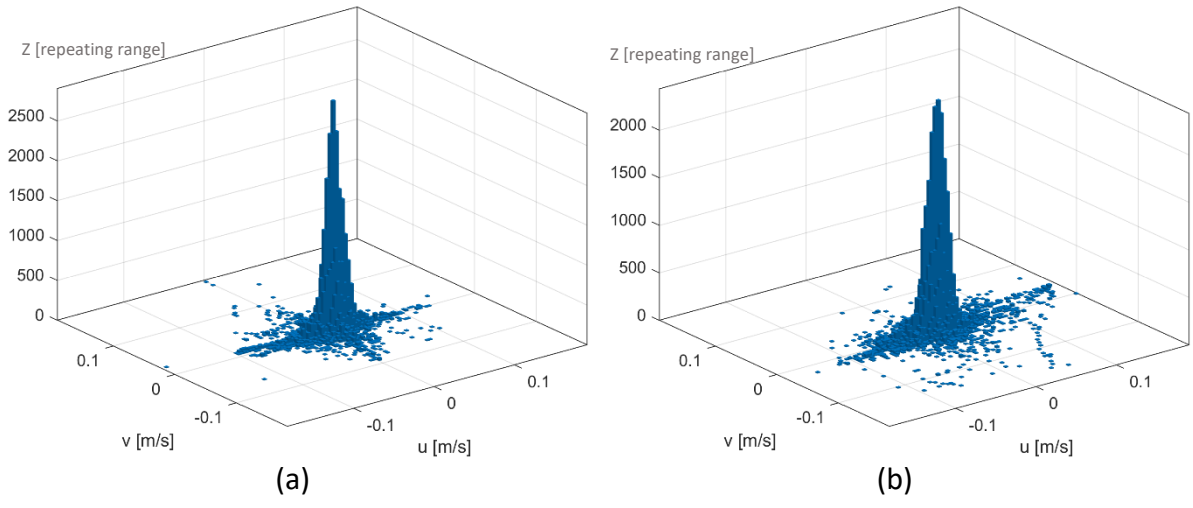

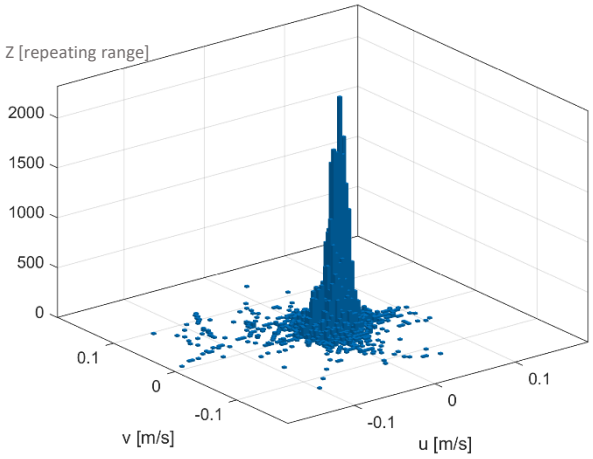

(c)

Figure 4- 21. Horizontal (u) and vertical (v) velocities for ice cover and two working fans for the 1st (a), 2nd (b) and 3rd (c) repeated experiments with counting number (z-axis).

Table 4- 3. The maximum repeating ranges of the longitudinal velocity of ice cover for different experiments.

Experiment type for ice cover based on the wind field and repeating experiment	**Maximum repeating range of ice cover velocity (m/s)**
One working fans and 1st repeated experiment	0.00-0.00
One working fans and 2nd repeated experiment	0.00-0.00
One working fans and 3rd repeated experiment	0.00-0.00
Two working fans and 1st repeated experiment	0.005-0.01
Two working fans and 2nd repeated experiment	0.015-0.02
Two working fans and 3rd repeated experiment	0-0.005
Three working fans and 1st repeated experiment	0.01-0.015
Three working fans and 2nd repeated experiment	0.015-0.02
Three working fans and 3rd repeated experiment	0.01-0.015

5 Implementation of the physical model results into the mathematical model

In this chapter, numerical simulation results related to ice velocity using the DynaRICE model, focusing on ice drift under the influence of different wind velocities, are presented. The ice concentration, size and wind velocities applied in the numerical simulations are based on the observed parameters from the physical modelling.

5.1 Velocity and displacement of the ice

The ice concentration and wind velocity were the experimental model results and used as input values for the numerical simulation with the DynaRICE model. The averaged wind velocity values obtained from the experiments were 0.514695, 1.165798 and 1.499304 m/s. The size of the channel was the same as that of the experimental simulation except for the length, which was considered to be 20 m (Figure 3- 29). After testing the same length of the channel as the experimental simulation, it was decided to choose a longer length to limit the downstream boundary impact on the ice velocity; therefore 20 m was chosen as the length of the channel. Different concentrations of 0.125, 0.325, 0.525 and 0.65 were applied for the numerical simulations which were also observed in the experimental modelling. Different ice concentrations were applied to the DynaRICE model and are provided in Figure 5- 1. The sections were taken from a 1 m length (10^{th} to 11^{th} m) of the channel.

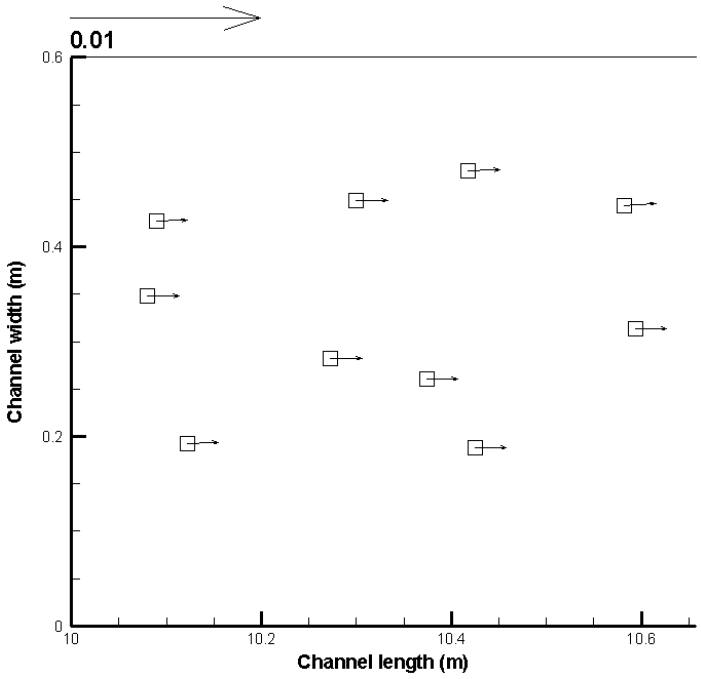
0.01
0.6
0.4
0.2
0
Channel width (m)
10
10.2
10.4
10.6
Channel length (m)

(a)

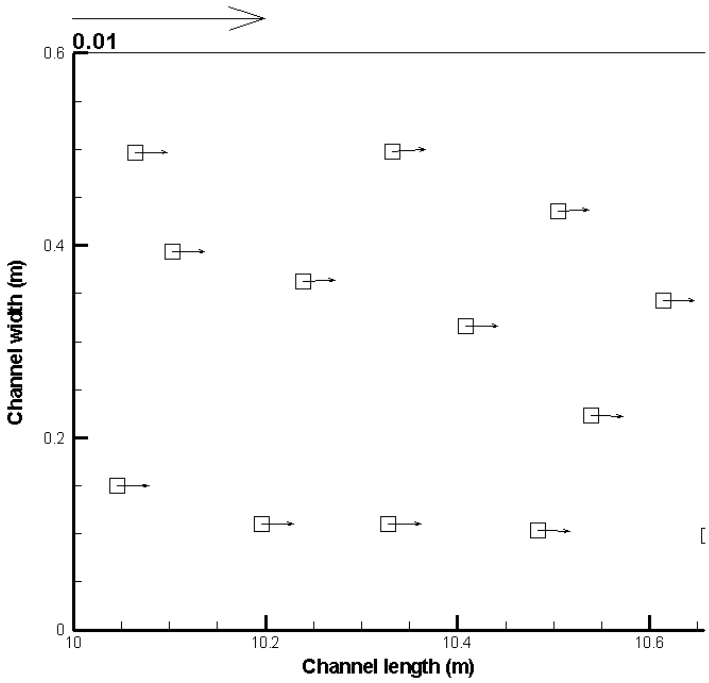
0.01
0.6
0.4
0.2
0
Channel width (m)
10
10.2
10.4
10.6
Channel length (m)

(b)

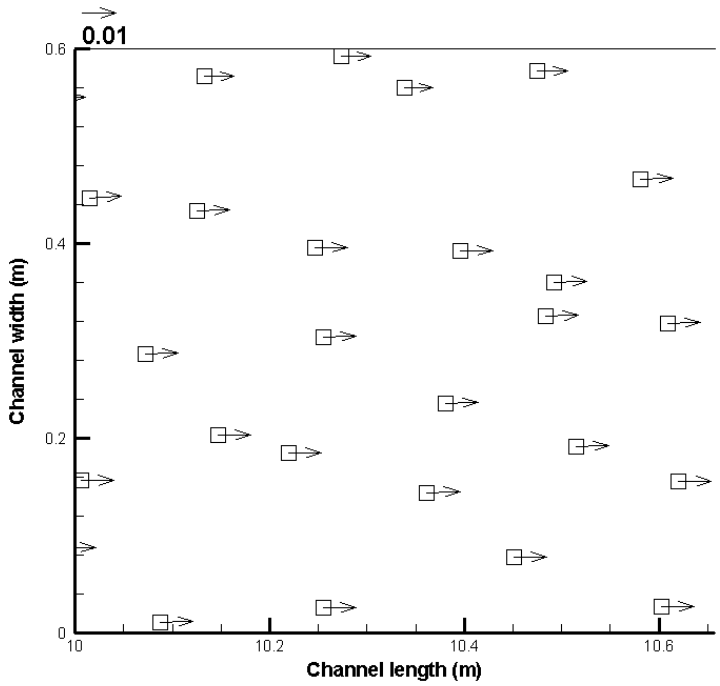

(c)

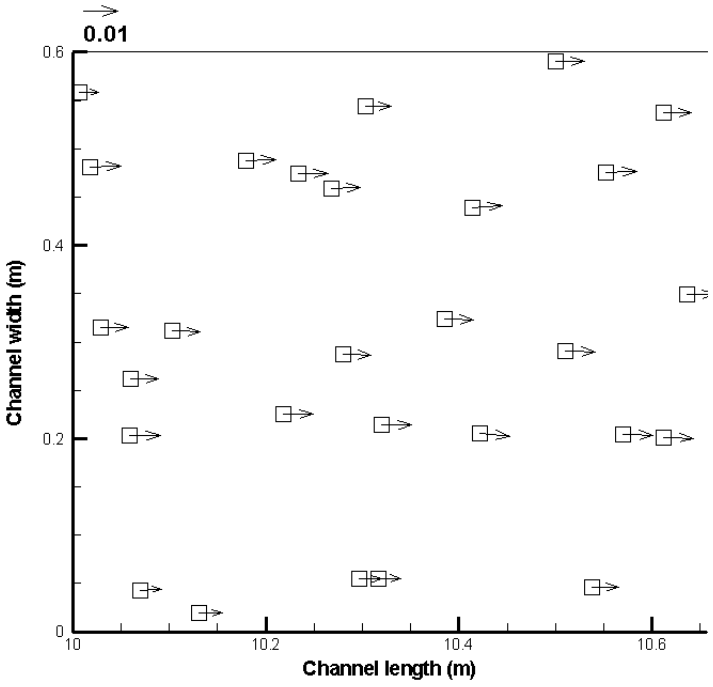

(d)

Figure 5- 1. The simulated ice with different concentrations of 0.125 (a), 0.325 (b), 0.525 (c) and 0.65 (d) in the DynaRICE model.

As can be seen in Figure 5- 1, the number of ice parcels increases with the concentration. The number of parcels fits within the ranges mentioned in Table 4- 1 for each concentration type. The decreasing ice velocity (based on the reference arrows) can be observed with increasing the concentration. The averaged ice velocity for different ice concentrations increases from the beginning of the simulation until 10 to 15 minutes. In Figure 5- 2 to Figure 5- 5, the trends for the averaged velocities versus the simulation time, for different concentrations (0.125, 0.325, 0.525 and 0.65) and wind velocities (0.514, 1.165 and 1.499 m/s) are presented.

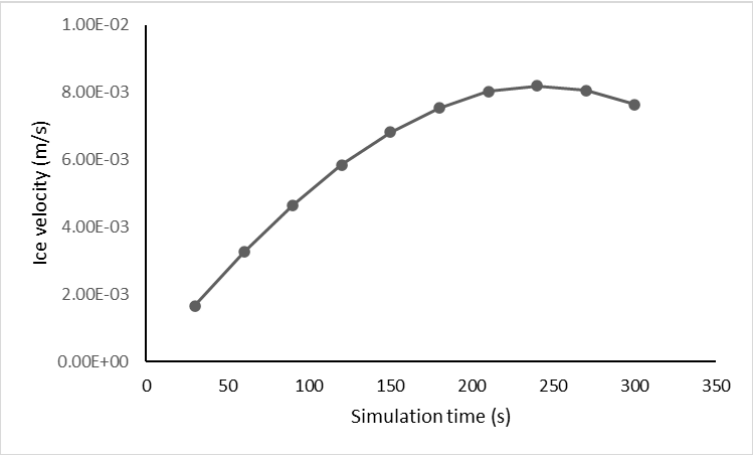

(a)

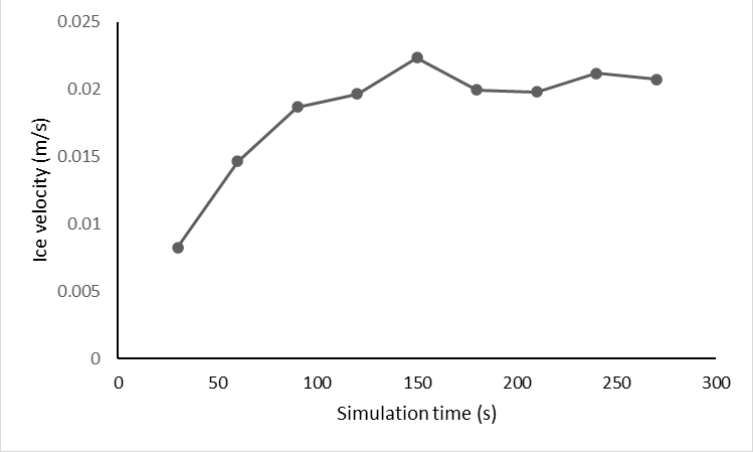

(b)

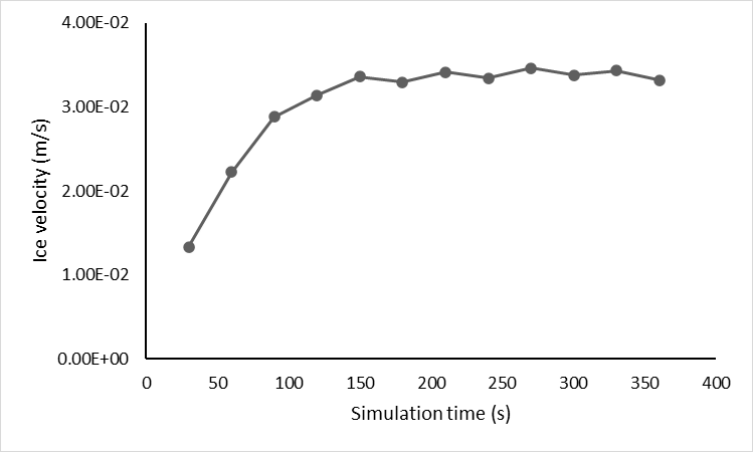

(c)

Figure 5- 2. The velocity results for the ice concentration of 0.125 and for the wind velocities of 0.515 (a), 1.165 (b), and 1.499 (c) m/s.

In Figure 5- 2, the ice velocity results simulated for the concentration of 0.125 under the effect of wind velocities of 0.515, 1.165 and 1.499 m/s using the DynaRICE model are presented. As expected, the increase in wind velocity leads to greater changes in ice velocity from the beginning to the end of the simulation, as shown in Figure 5- 2 (a) to (c). The graphs indicate that ice velocity stabilizes after a certain period of simulation time. However, slight fluctuations in ice velocity are observed near the end of the simulation, particularly at a wind velocity of 1.165 m/s. The averaged velocity values after stabilization for the ice concentration of 0.125 and wind velocities of 0.515, 1.165 and 1.499 are 0.007, 0.019 and 0.033 m/s, respectively.

The ice velocities corresponding to the ice concentration of 0.325 and wind velocities of 0.515, 1.165 and 1.499 m/s are presented in Figure 5- 3. Comparing the graphs in Figure 5- 2 and Figure 5- 3, for the ice concentrations of 0.125 and 0.325, the ice velocity at the start of the simulation is the same for each wind velocity. However, slight fluctuations are observed after the stabilization of ice velocity for wind velocities of 1.165 and 1.499 m/s. For the ice concentration of 0.325 and the three wind velocities, the average velocity values after stabilization are 0.008, 0.021 and 0.034 m/s.

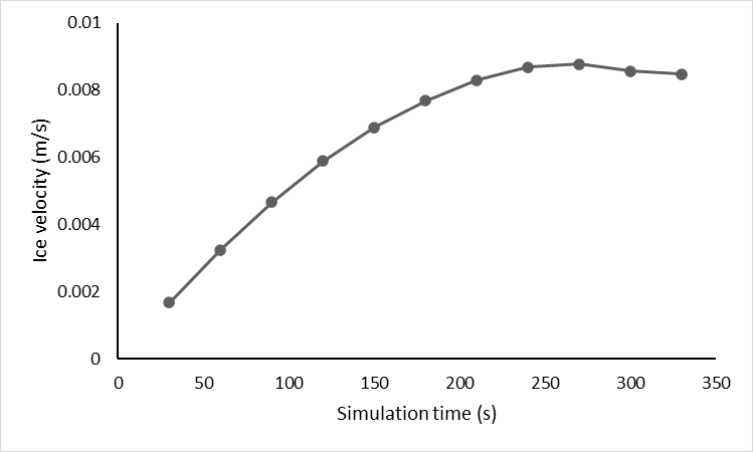

(a)

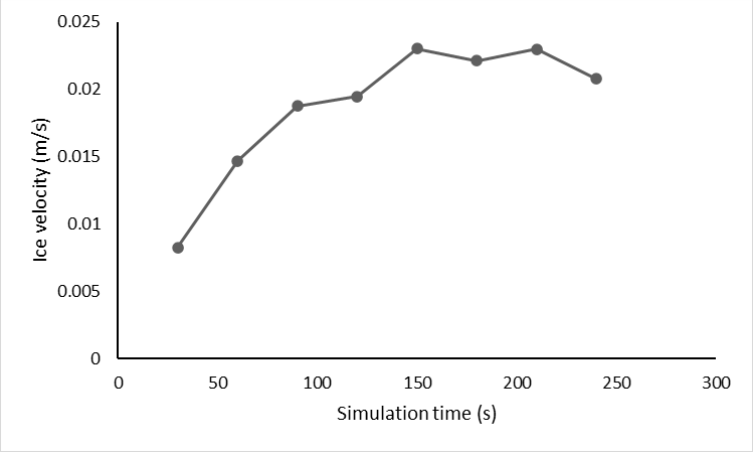

(b)

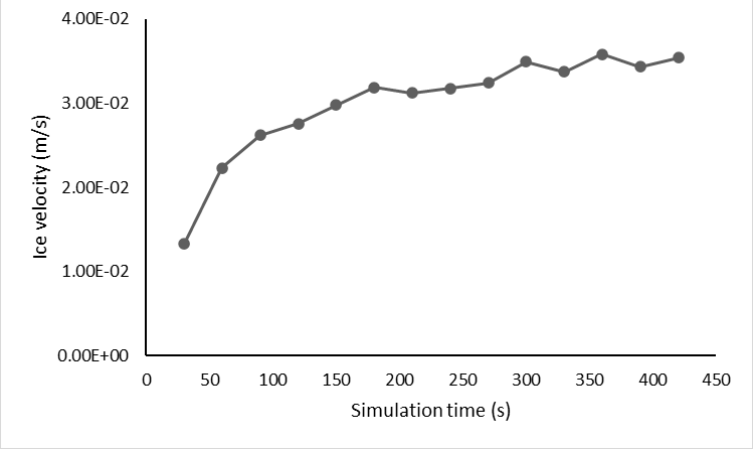

(c)

Figure 5- 3. The velocity results for the ice concentration of 0.325 and for the wind velocities of 0.515 (a), 1.165 (b), and 1.499 (c) m/s.

In Figure 5- 4 and Figure 5- 5, the ice velocities corresponding to ice concentrations of 0.525 and 0.65 are presented. The averaged velocities after stabilization for the three wind velocities are 0.009, 0.022 and 0.032 for the former concentration, and 0.008, 0.022 and 0.031

for the latter concentration. As observed from the ice velocity values for both concentrations, approximately the same velocities are obtained for each wind velocity.

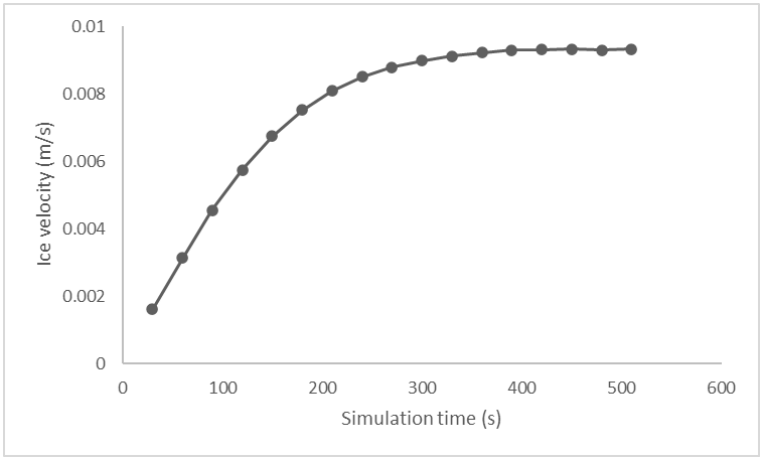

(a)

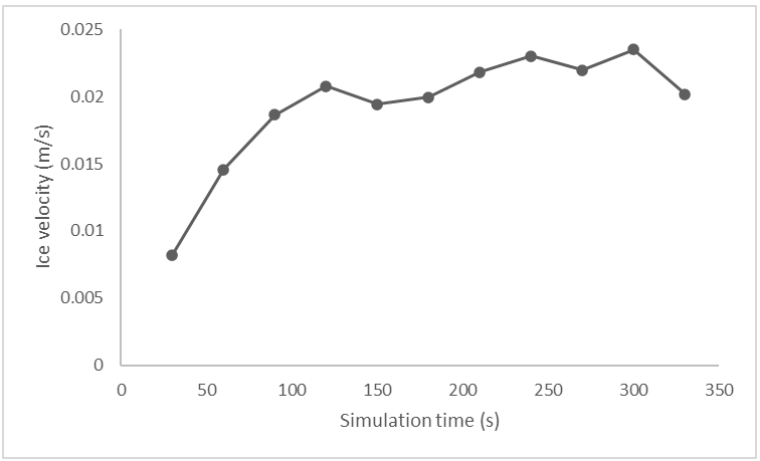

(b)

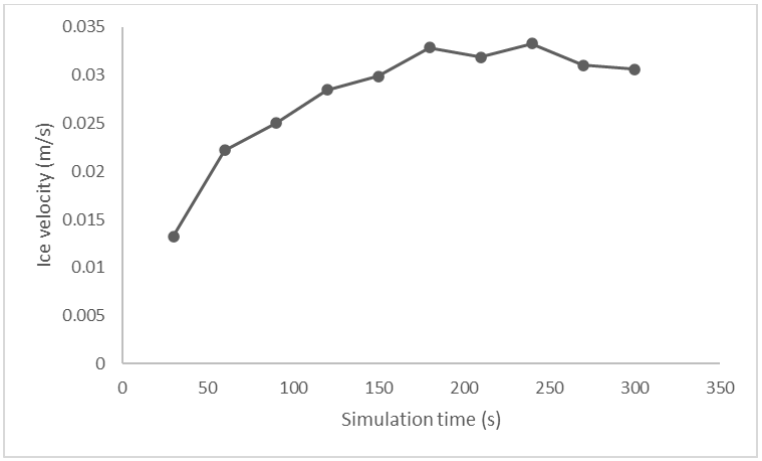

(c)

Figure 5- 4. The velocity results for the ice concentration of 0.525 and for the wind velocities of 0.515 (a), 1.165 (b), and 1.499 (c) m/s.

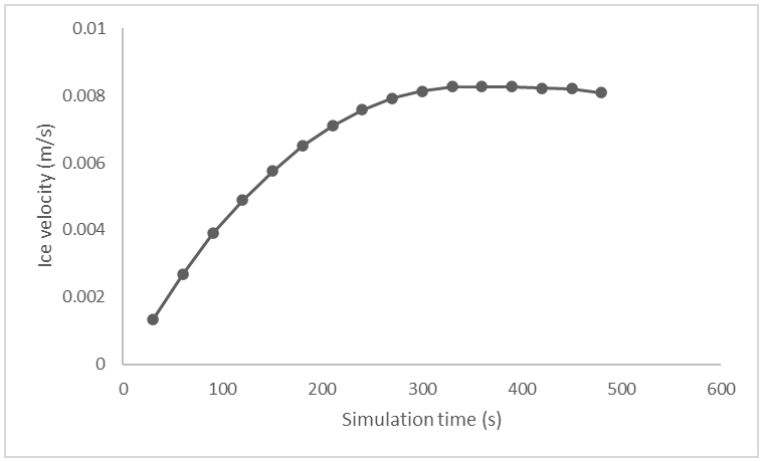

(a)

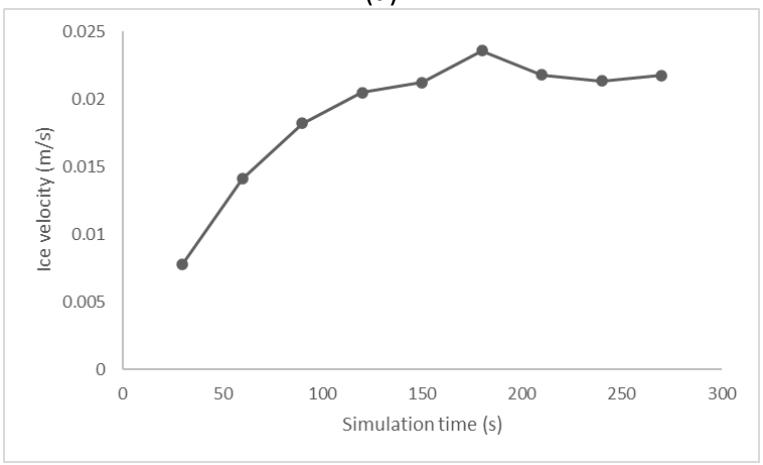

(b)

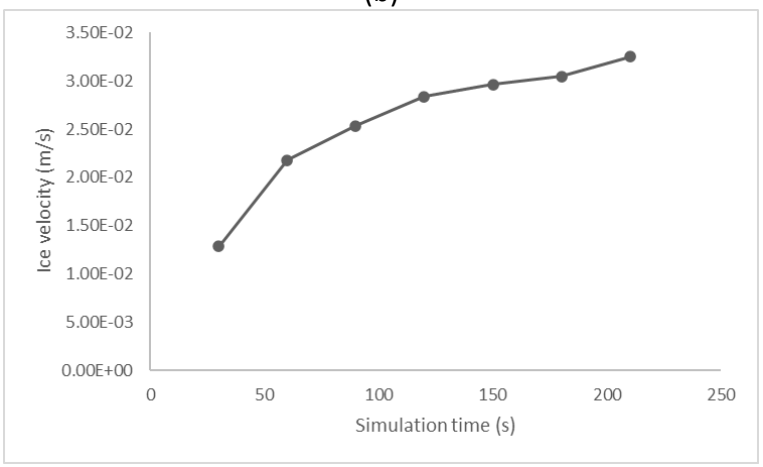

(c)

Figure 5- 5. The velocity results for the ice concentration of 0.65 and for the wind velocities of 0.515 (a), 1.165 (b), and 1.499 (c) m/s.

In Figure 5- 2 to Figure 5- 5, ice velocities reach a maximum level. The averaged velocities of ice after stabilization (reaching the maximum level) for different concentrations and wind velocities were calculated and are presented in Figure 5- 6. The averaged ice velocities showed ranges of 0.0075 to 0.0094 m/s, 0.021 to 0.022 m/s and 0.031 to 0.033 m/s for wind velocities of 0.514, 1.165 and 1.499 m/s.

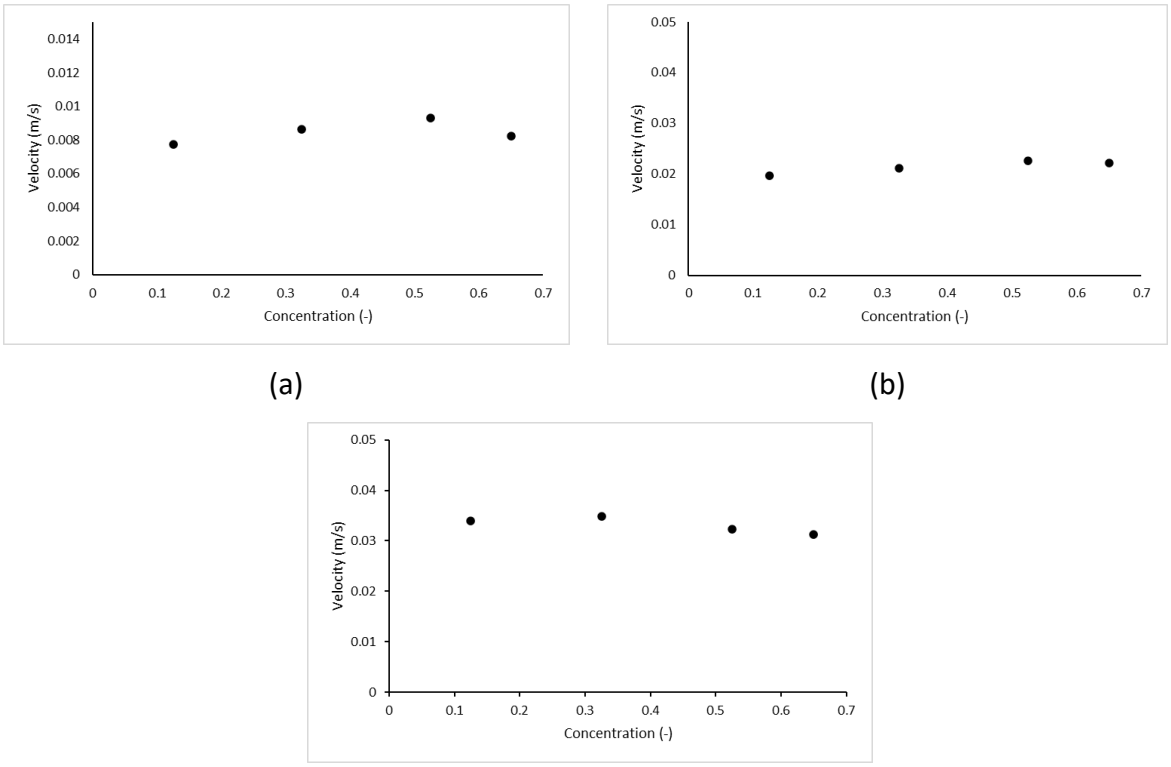

Figure 5- 6. The averaged simulated velocities of ice for wind velocities of 0.514 (a), 1.165 (b), and 1.499 (c) m/s.

The simulation of ice cover with the DynaRICE model was calculated by placing a cover along the channel and breaking it into pieces with the dimensions of ice in the experimental simulations. The averaged velocities of ice cover for different wind velocities are shown in Figure 5- 7. The averaged ice cover velocity values stabilized after some simulation time, as can be seen in Figure 5- 7. The averaged ice cover velocity values are 0.002719, 0.005822 and 0.010494 m/s for the wind velocities of 0.514, 1.165 and 1.499 m/s, respectively.

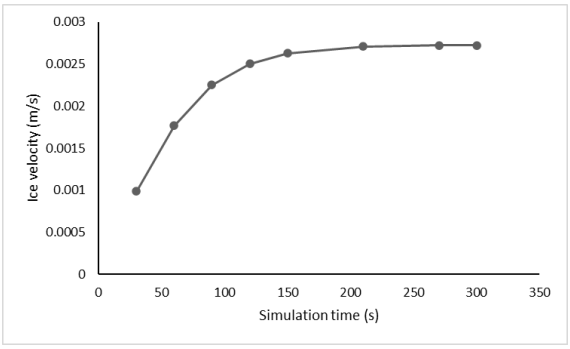

(a)

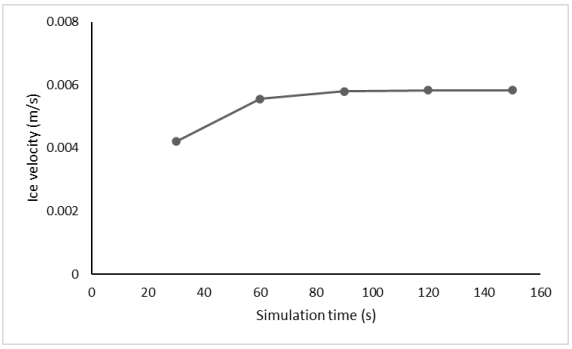

(b)

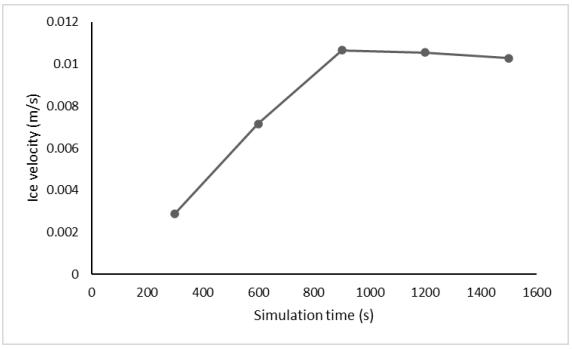

(c)

Figure 5- 7. The averaged simulated ice cover velocities for wind velocities of 0.514 (a), 1.165 (b), and 1.499 (c) m/s.

In Figure 5- 8, a comparison between ice velocity results from the PTV calculations, considering the entire measurement field, and the DynaRICE model is presented. The results are shown for different ice concentrations and repeated experiments. In this figure the results are compared with the DynaRICE model results, which are already presented in Figure 5- 6.

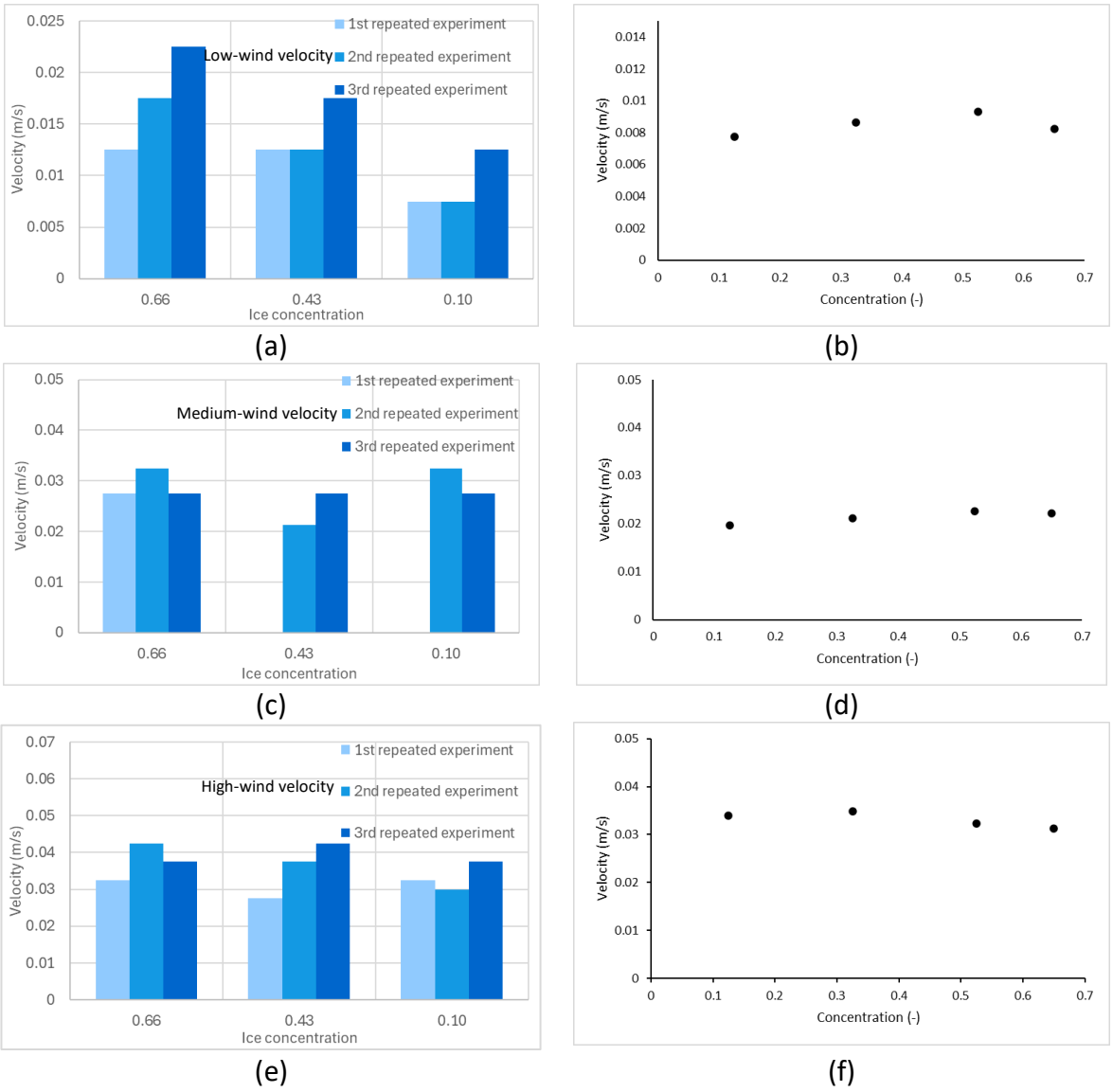

Figure 5- 8. The comparison between ice velocities from PTV calculation (a, c, e) and the results from the DynaRICE model (b, d, and f) for the wind fields with one, two and three working fans, respectively, and for different ice concentrations.

In Figure 5- 9, the ice cover velocities from experimental simulations under the effect of two and three working fans are provided. The averaged ice cover velocities of three repeated experiments under each wind field are presented. In Figure 5- 10, a comparison is provided between the calculated average ice cover velocities from the experimental simulation (using both the entire and limited, confined ice velocity fields) and the DynaRICE model with varying wind velocities. The trendlines for both numerical and experimental ice cover velocities are also shown. As seen in Figure 5- 10, the ice cover velocity results from the experimental simulations are linear when using the entire ice velocity field and logarithmic when using a limited, confined area, while the numerical simulation results are polynomial. The DynaRICE model generally showed lower values compared to the experimental velocities, except at low

wind velocity. The average velocity differences between the experimental results using a limited, confined area and the DynaRICE model is 58%. The difference between the experimental results using the entire ice velocity field and the DynaRICE model is reduced to 18%. These percentages are calculated based on the differences between the average of ice velocities under different wind field conditions and the DynaRICE model results, divided by the experimental velocity results. It can be observed that the DynaRICE model results are closer in value to the experimental modelling using the entire ice velocity field.

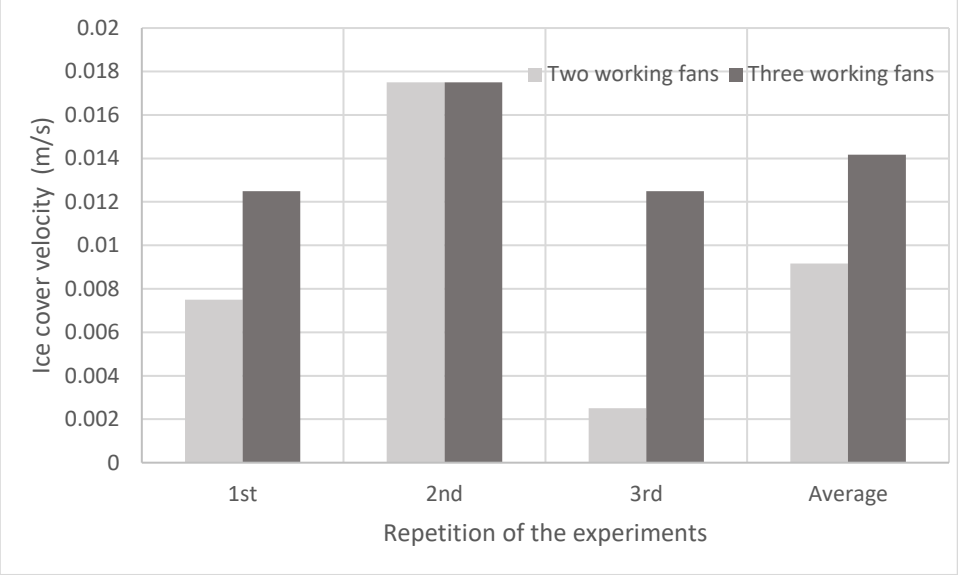

Figure 5- 9. Ice cover velocities from PTV measurements for three repeated experiments with two and three working fans, across the entire measurement field.

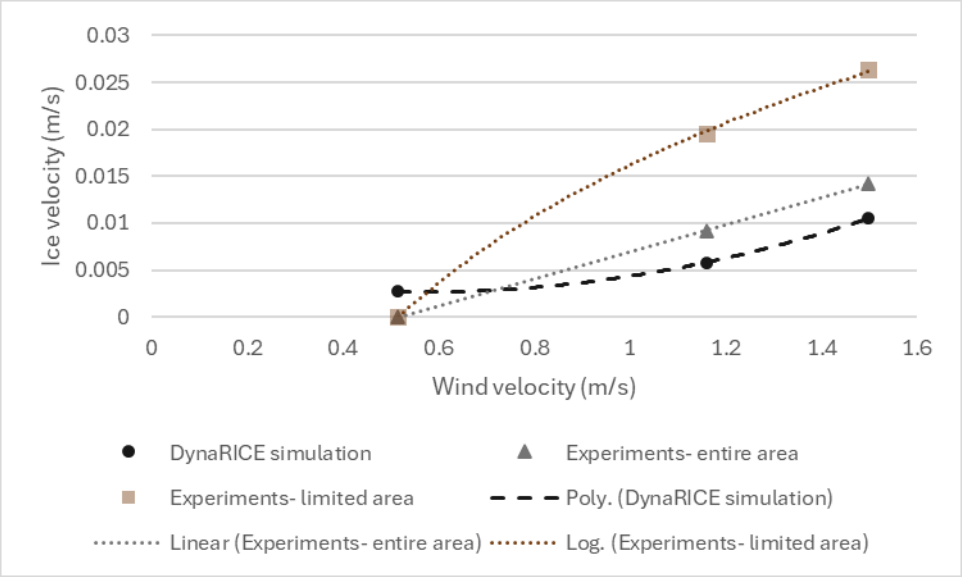

Figure 5- 10. A comparison between ice cover velocities from PTV calculation across the entire measurement field and the DynaRICE model.

In Figure 5- 11, the averaged velocities of ice pieces and ice cover, corresponding to different wind fields, are presented in a single plot. The results are based on the PTV calculations for both the entire measurement field and a limited field, which is confined to the area around the PIV measurement for wind velocity. The ice cover velocities are defined by a concentration of 1.

As can be observed from the plot, the relationship between ice velocity and concentration shows opposite trend for the two measurement approaches. Using the limited ice velocity field resulted in higher velocity values compared to those from the entire measurement field. However, the velocity of ice pieces under the three working fans in both approaches show closer values compared to those for other wind fields, with the ice pieces velocity for the medium wind field being identical at 0.0291 m/s in both cases. The ice cover velocities across different wind fields are lower compared to those of ice pieces.

In the limited ice velocity field, the ice cover velocities for the wind fields of two and three working fans show a 39% and 31 % difference, respectively, compared to the average ice piece velocities across varying concentrations. When considering the entire ice velocity field, the differences are 67% and 60%, respectively, for the same wind fields. This indicates that ice cover velocities become closer to the average velocities of ice pieces as wind velocity increases. The percentage difference is obtained from dividing the difference in ice pieces

velocities. Since the ice cover does not move under low wind velocity, these values are indicated as zero on the plot.

In the DynaRICE model, the differences between the velocities of ice pieces and ice cover under the low, medium and high wind conditions are 67%, 72% and 68%, respectively. These values are closer to the percentage difference obtained from the approach that considers the entire ice velocity field. The velocities of ice pieces and ice cover as obtained from the DynaRICE model simulation are provided in Figure 5- 6 and Figure 5- 10.

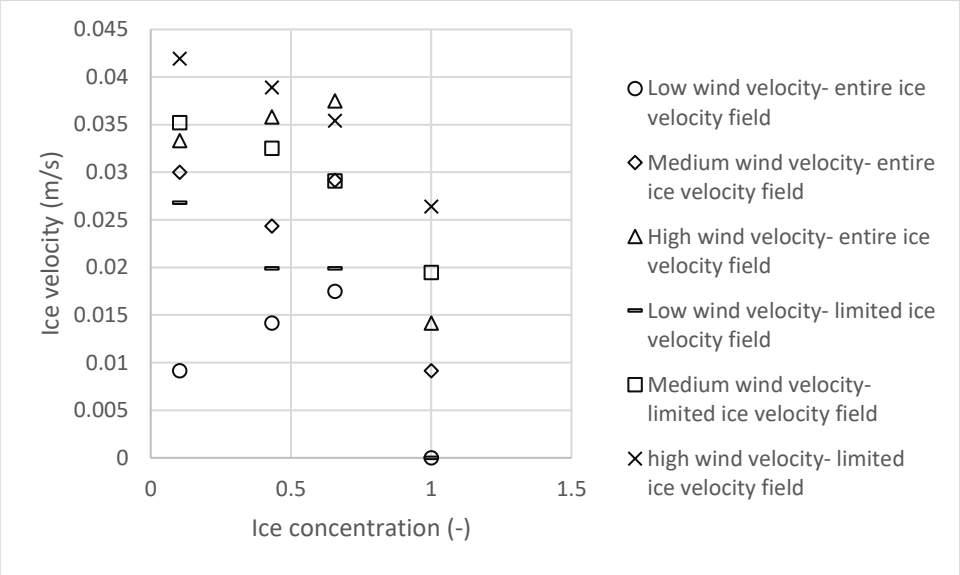

Figure 5- 11. Calculated ice velocities for ice cover with the concentration of 1 and ice pieces with different concentrations. The ice velocities are related to the different wind conditions and limited ice velocity field as well as entire ice velocity field.

Since the validity of the logarithmic distribution is confirmed by Wu (Wu, 1973), for this study the velocity profile is fitted to the logarithmic profile. The influence of wind resistance on ice can be assessed by converting Manning's roughness coefficient to a wind drag coefficient. This conversion utilizes the observed wind velocity profile obtained from PIV measurements (Figure 4- 4). A typical logarithmic law formulation for the boundary layer is given in Eq. 5-1 (Overland, 1985). In this equation, $u_{(z)}$ represents the wind velocity at height z, u_* is the shear velocity, K is Karman universal constant (0.4), and k is the roughness height.

$$u_{(z)} = \frac{u_*}{K} \ln\left(\frac{z}{k}\right) \qquad \textit{Eq. 5- 1}$$

Eq. 5-2 describes the relationship between the wind shear tension (τ), air density (ρ_a) and shear velocity (u_*), which facilitates the conversion from the Manning's roughness coefficient to the wind drag coefficient for the surface. Eq. 5-3 provides the relation between the wind drag coefficient (C_a), shear tension (τ), and air density (ρ_a). In this equation, and for this study, $\bar{v}$ represents the average wind velocity over the flume's height.

$$\tau = \rho_a {u_*}^2 \qquad \textit{Eq. 5- 2}$$

$$C_a = \frac{\tau}{\rho_a \bar{v}^2} \qquad \textit{Eq. 5- 3}$$

To fit the observed wind velocity data from the PIV measurement to the logarithmic velocity in Eq. 5-1, Eq. 5-4 is used. In Eq. 5-4, $u_{(z)}$ is the wind velocity transformed to the logarithmic equation and z is the distance from the water surface. This equation allows for a linear regression based on $ln(z)$ to find A and B. In Eq. 5-5, the relationship between shear velocity (u_*) and Karman universal constant (K), and in Eq. 5-6, the formulation for the roughness height (k) in linear regression and based on Eq. 5-4 are provided.

$$u_{(z)} = A \cdot ln(z) + B \qquad \textit{Eq. 5- 4}$$

$$u_* = A \times K \qquad \textit{Eq. 5- 5}$$

$$k = \exp\left(-\frac{B}{A}\right) \qquad \textit{Eq. 5- 6}$$

By adjusting the Manning's coefficient to match the wind drag coefficient using Eq. 5-2 and Eq. 5-3, the wind drag coefficient can be determined for the observed velocities obtained from the PIV measurements. The values of A for the wind fields with one and two working fans are negative. This occurs because the average wind velocity values do not exhibit an increasing trend with distance from the water surface. Consequently, for calculating the wind drag coefficient (C_a), only the wind field with three working fans is considered. The observed wind

velocities (from the PIV measurements) and the logarithmic trend values of wind velocity ($u_{(z)}$) are compared in Figure 5- 12.

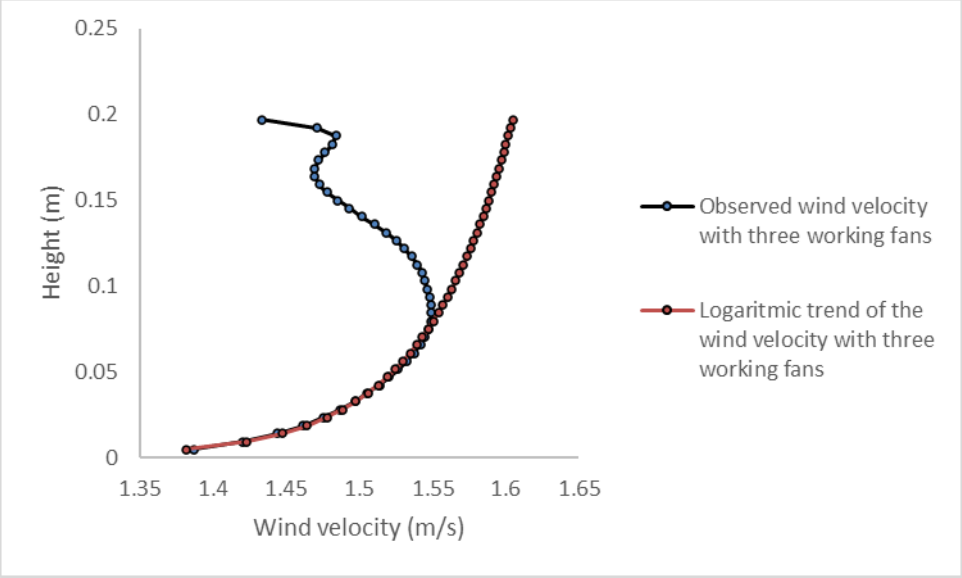

Figure 5- 12. Comparison between the observed wind velocity field of three working fans and the transformed logarithmic wind velocity values.

The regression between the wind velocities of three working fans and the predicted logarithmic values up to the limit of 8 cm distance from the water surface shows 99% data coverage (R^2). The calculated wind drag coefficient from Eq. 5-3 is $C_a = 2 \times 10^{-4}$. The observed wind velocity profile for this study is influenced by the resistance of the water surface and the significant effect of the flume ceiling (which is immovable). For the calculation of C_a, the lower boundary, represented by the water surface, is considered. In the DynaRICE model, a value of 15×10^{-3} is applied for the wind drag coefficient, which is an order of magnitude higher than 2×10^{-4} (obtained from the logarithmic profile). This discrepancy can be attributed to the low range of wind velocities in the experiments. The lower the range of wind velocity, the more the wind velocity profile is influenced by the upper boundary of the wind field. At higher wind velocities, the wind velocity profile approaches a logarithmic shape. It is notable that, within this range of wind velocities, a fully turbulent flow does not develop, and the flow remains within the boundary layer regime. This situation is mentioned in Wu, 1973, that in low wind shear velocities, transition of the boundary layer from laminar to turbulent emerges, while in high wind velocities it is turbulent.

To obtain the closest results with the DynaRICE model, the numerical simulation results were compared with the PTV calculations using a limited area (Figure 4- 8 (a)) while varying the wind drag coefficient. Trial-and-error simulations were conducted for cases with low ice concentration, and the closest ice velocity results, based on the adjusted wind drag coefficient, were used for each wind velocity and all ice concentrations Figure 5- 13. The ice velocity results with a drag coefficient of 0.0015 (previously shown in Figure 5- 6) and the experimental results are also presented in Figure 5- 12. Examples of the trial-and-error process are provided in Table 5- 1, showing the corresponding error values. Based on these results, for wind fields generated by one and two working fans, a wind drag coefficient of 0.002 and 0.0025 yielded the smallest errors, whereas for three working fans, a coefficient of 0.009 produced the smallest errors in ice velocity results. In Figure 5- 14, the wind drag coefficients, for which the closest results were obtained from the DynaRICE model and compared to the experimental model, are presented versus wind velocity. In this graph, the line corresponding to a wind drag coefficient of 0.0015 is shown, representing the default value in the DynaRICE model.

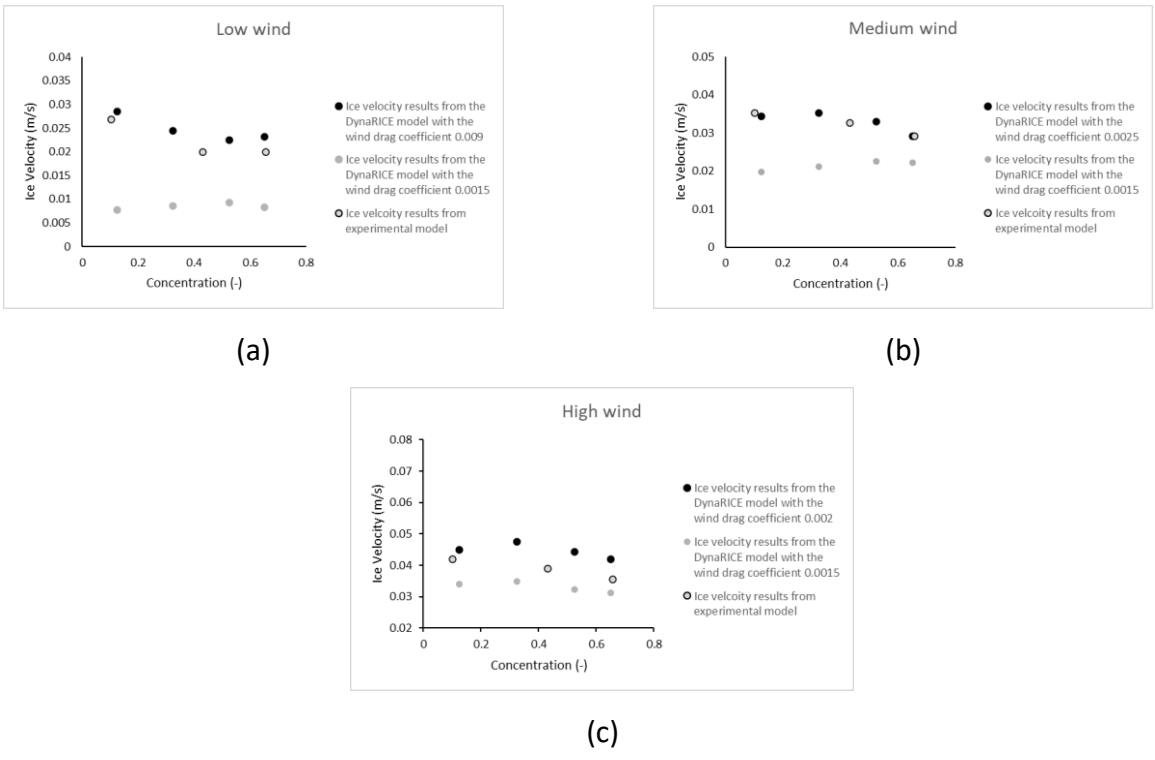

Figure 5- 13. Ice velocity results from the DynaRICE model with a wind drag coefficient of 0.0015 (grey dots) and 0.0009 for low wind (a), 0.0025 for medium wind (b), and 0.002 for high wind (c) velocities.

Table 5- 1. Trial-and-error results for wind drag coefficients at different wind velocities and an ice concentration of 0.0125, compared with experimental results from PTV calculations using a limited ice velocity area.

	Wind drag coefficient	DynaRICE model ice velocity results (m/s)	Experimental ice velocity results (m/s)	Calculated error for ice velocity
Low Wind velocity	0.0015	0.008	0.027	0.711
	0.003	0.012		0.557
	0.006	0.019		0.285
	0.008	0.020		0.255
	0.009	0.029		-0.065
Medium Wind velocity	0.0015	0.020	0.035	0.442
	0.002	0.030		0.162
	0.0025	0.034		0.027
	0.003	0.038		-0.073
Medium Wind velocity	0.0015	0.034	0.042	0.190
	0.002	0.039		0.067
	0.003	0.045		-0.072

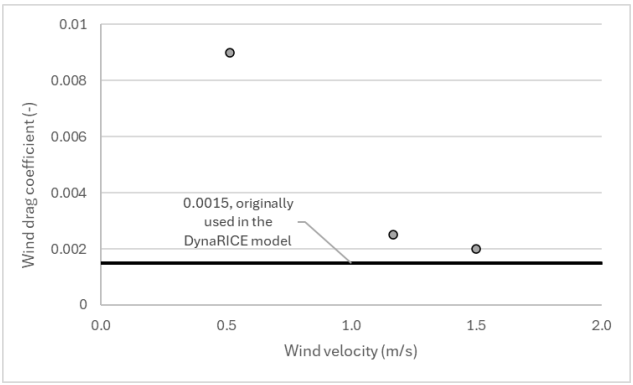

Figure 5- 14. The wind velocity versus wind drag coefficient obtained from the closest results of the DynaRICE model compared to the experimental velocity.

6 Model calibration with the real-case scenarios

In this section, two studies conducted using the DynaRICE model, referring to the real-case scenarios, will be discussed. The first study examines ice forces imposed on a photovoltaic structure, while the second focuses on polynya formation in the Vistula Lagoon, both considering the effect of wind. These studies were performed using the latest updated version of the DynaRICE model to account for wind tension on the ice.

6.1 Ice forces on photovoltaic structure

A study was conducted to show the importance of the wind effect on ice (Kolerski et al., 2021). The study was related to the installation of a floating photovoltaic structure on the Łapino reservoir. During freeze-up, skim or frazil ice may form in turbulent flow, while static ice cover may form in the low flow conditions. The latter is usually the hydrodynamic condition affecting the floating photovoltaic structure, leading to static ice cover formation. Among all the weather and hydrological parameters examined, wind was found to be the most influential factor.

The site is located in the reservoir of the Łapino dam, with both inflow discharge from the Radunia River, and the outflow discharge at the hydroelectric power plant of 22 m^3/s. Downstream water level was considered as the normal pool level, equals to 99.6 m. Based on the observed low flow velocity, the ice cover would form in the study area. At the aim of power production, water level was decreased by 1 and 2 m, lowering the water levels to 98.6 and 97.6 m, respectively. For starting the simulation, the stationary ice cover with the thickness of 0.15 m was estimated for the whole area of the study, based on hydrological and meteorological data, as well as heat balance of the surface of the ice. A simplified method known as “freezing degree-days (FDD)”, was used for this purpose. The major advantage of this method is its simplicity for application in practical issues, and high compatibility with the observations.

Dynamic impact of the wind may push ice floes towards structures. Wind data for the study related to the years between 2015 and 2019, from the Institute of Meteorology and Water Management, and the closest observation location to the Łapino reservoir. Winds with the constant speeds from 10 to 26 m/s were used for 12 hours of the simulation time. The north

direction for the wind velocity was considered, due to the topography of the area. In the case of the northern wind, the ice shoved by the wind can extend to a length of about 1000 m, and may put the front edge of the structure under the large forces. The model covered 36 ha, which was 70% that of the reservoir. An example of ice jam around the photovoltaic platform is presented in Figure 6- 1. The provided legend shows the thickness of ice cover around the structure, indicating the highest accumulation next to the front edge of the structure.

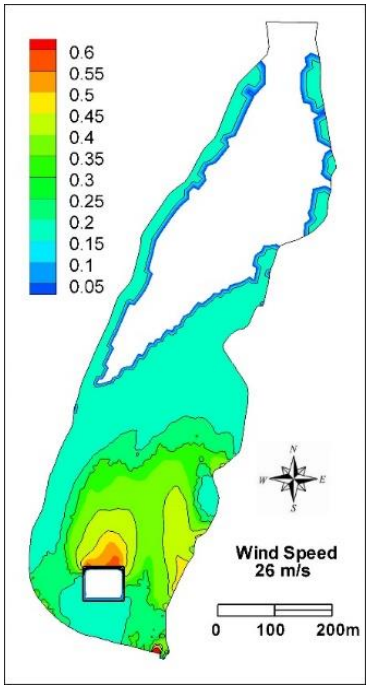

Figure 6- 1. Ice jam around the PV structure, with the wind velocity of 26 m/s (Kolerski et al., 2021).

Figure 6- 2 illustrates the different values of normal and tangential loads applied to the edges of the structure. For the normal forces, the maximum load was exerted on the left side of the northern edge. The maximum normal forces, imposed in cases with a wind velocity of 26 m/s and a damming level reduction of 1 m, were 1.43 and 2.7 times greater than the forces applied to structures with wind velocities of 20 m/s and 15 m/s, respectively. The bottom edge bears negligible forces. Among the corner edges, the left edge experiences comparatively smaller loads. A 2 m reduction in the damming level did not significantly affect the imposed normal forces.

For the tangential forces on Figure 6- 2, the maximum load was observed in the leftward direction on the right side. This maximum value for a wind velocity of 26 m/s was 2.67 and 1.6 times greater than those at 20 m/s and 15 m/s, respectively. On this edge, fluctuations in tangential forces were attributed to ice jamming variations and discrete areas of maximum

ice jamming. The tangential loads on the southern edge are minimal due to the wind direction. For the corner edges, the tangential force was oriented southward, with the highest values observed at the tops of both edges. Additionally, a 2 m reduction in damming level did not noticeably alter the maximum range of tangential loads, though it increased the maximum load on the left edge by six times.

Table 6- 1 presents the normal and tangential forces on the edges of the structure, while Figure 6- 3 illustrates the direction and magnitude of force vectors for the case of 26 m/s wind velocity. According to Table 6- 1, greater fluctuations in the magnitude of forces were observed on the different edges in the 26 m/s case. However, as wind velocity decreased, the forces became more balanced. Furthermore, the negligible tangential forces on the southern edge across different wind velocities suggest that the wind has little effect on this edge, likely due to reduced contact between the ice cover and the southern edge.

Considering both Table 6- 1 and Figure 6- 3, tangential forces on the northern edge are primarily directed westward, while on the eastern edge, they are directed southward. Since the southern and western edges did not experience significant total forces, a southeast direction for tilting can be predicted. The tilting directions remained largely consistent across variations in pool level and wind speed.

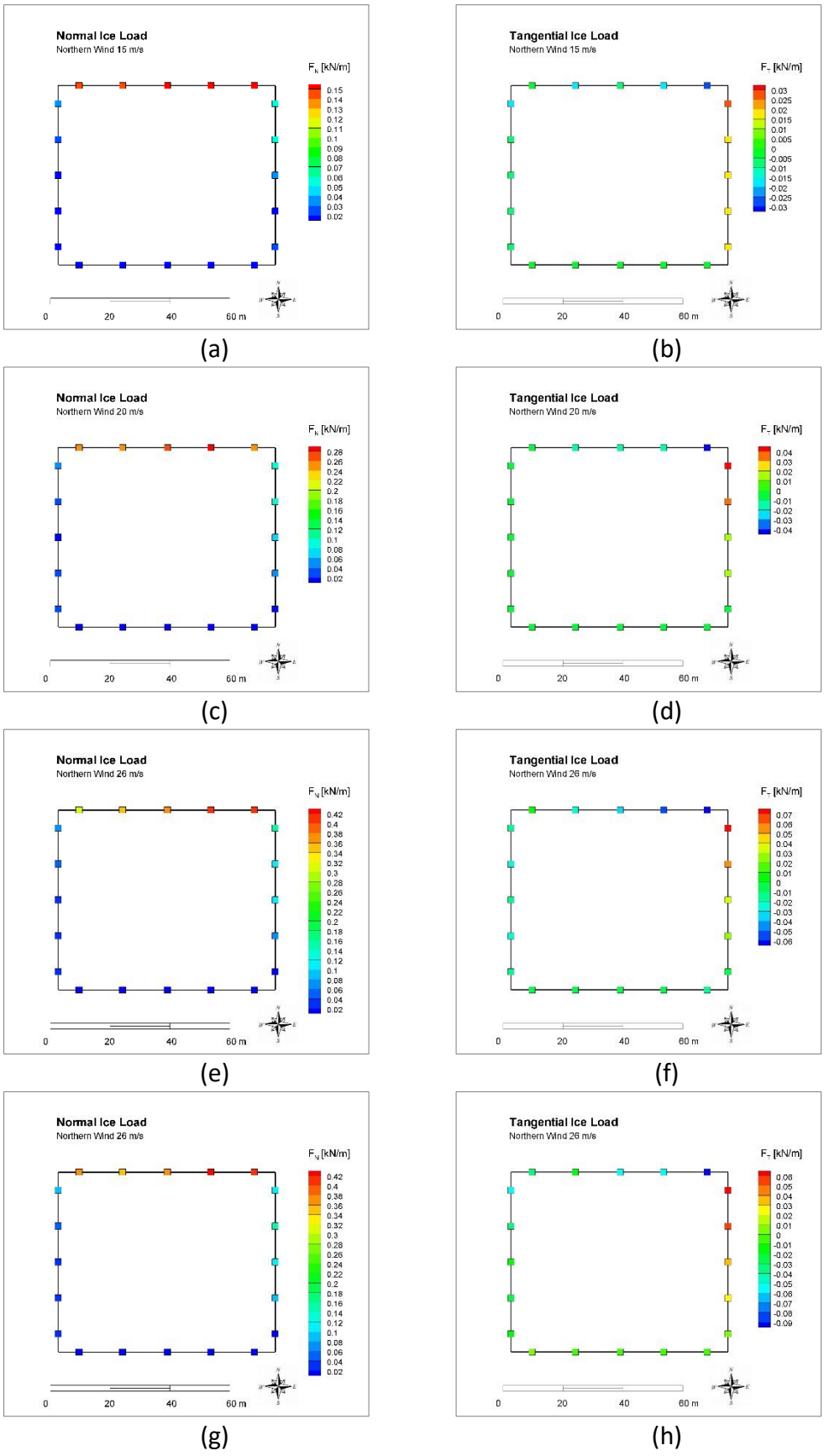

Figure 6- 2. Normal and tangential ice forces for different wind velocities, figures (a) to (e) are attributed to 1 m, and (g) to (h) to 2 m damming level reduction (Kolerski et al., 2021).

Table 6- 1. Resultant forces of static ice pressure on PV structure, for the northern wind, and variable speed (Kolerski et al., 2021).

positive direction		Wind 26 m / s				Wind 20 m / s		Wind 15 m / s	
		Pool level reduction of 1m		Pool level reduction 2 m		Pool level reduction of 1 m			
		Normal force	Tangential force	Normal force	Tangential force	Normal force	Tangential force	Normal force	Tangential force
		kN/m	kN/m	kN/m	kN/m	kN/m	kN/m	kN/m	kN/m
North edge	→	0.3	0.01	0.36	-0.04	0.26	-0.01	0.14	0
		0.35	-0.03	0.35	-0.02	0.26	-0.02	0.14	-0.02
		0.37	-0.04	0.38	-0.05	0.27	-0.02	0.16	-0.01
		0.41	-0.05	0.43	-0.05	0.3	-0.02	0.16	-0.02
		0.42	-0.07	0.4	-0.1	0.25	-0.05	0.16	-0.03
East edge	↓	0.15	0.08	0.12	0.07	0.09	0.05	0.06	0.03
		0.12	0.05	0.15	0.06	0.09	0.04	0.05	0.02
		0.11	0.04	0.11	0.04	0.07	0.02	0.04	0.02
		0.08	0.03	0.09	0.03	0.05	0.02	0.02	0.02
		0.02	0	0.02	0.01	0.01	0	0.03	0.02
South edge	←	0.02	-0.02	0	0	0.01	0	0.01	0
		0.01	-0.01	0.01	0	0.01	0	0.01	0
		0.01	0	0.01	0	0.01	0	0.01	0
		0.01	0	0.01	0	0.01	0	0.01	0
		0.01	0	0.01	0.01	0.01	0	0.01	0
West edge	↑	0.04	-0.02	0.04	-0.02	0.04	-0.01	0.02	-0.01
		0.03	-0.03	0.04	-0.03	0.03	-0.01	0.02	-0.01
		0.04	-0.02	0.04	-0.02	0.02	-0.01	0.02	-0.01
		0.05	-0.03	0.06	-0.04	0.03	-0.01	0.03	-0.01
		0.08	-0.02	0.09	-0.05	0.05	-0.01	0.04	-0.02

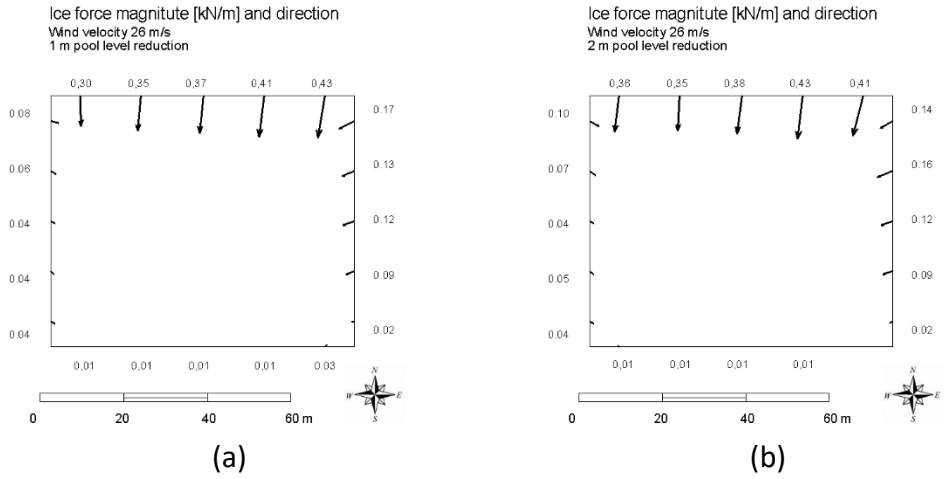

Figure 6- 3. Direction and magnitude of the force vectors on the structure edges for 26 m/s of the wind velocity, and 1 m as well as 2 m damming level reduction (Kolerski et al., 2021).

Figure 6- 4 shows the maximum tangential and normal forces on the structure at different wind speeds. The normal force exhibited a larger range of variation compared to the tangential force, with its variation range being 5.8 times greater. A sharp increase in the normal force was observed between 10 and 20 m/s, rising from 0.07 to 0.31 kN/m. From 22 to 24 m/s, a less steep increase was noted, followed by a sharp rise of 0.42 kN/m as wind speed reached 26 m/s.

In terms of tangential loads, no linear trend was observed. Between 10 to 13 m/s, 18 to 29 m/s, and 25 to 26 m/s, slight changes were recorded in maximum tangential loads, typically

followed by a sudden increase in maximum load. This sudden rise was especially prominent between 20 and 22 m/s, where the load increased from 0.05 to 0.07 kN/m before a quick drop back to 0.06 kN/m. Overall, a downward trend in tangential loads was identified between 21 and 24 m/s.

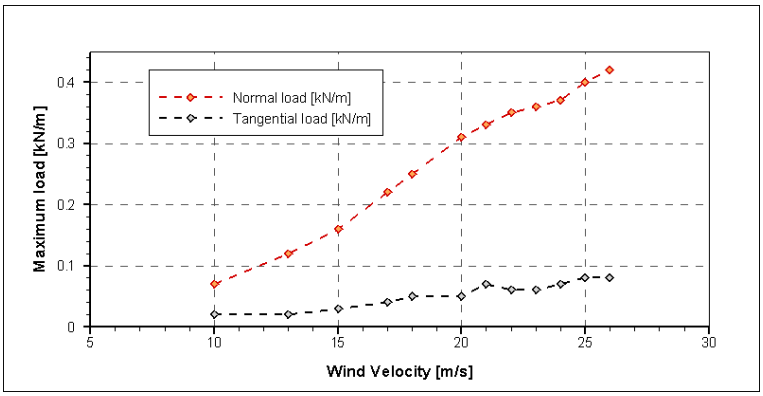

Figure 6- 4. Maximum normal and tangential forces for different wind velocities (Kolerski et al., 2021).

Figure 6- 5 illustrates the ice expansion and the distances of double and triple thicknesses from the structure following ice shoving under wind influence. The structure is located approximately 1200 m from the upstream boundary. For wind velocities below 10 m/s, there is no notable variation in ice cover expansion. However, after reaching 10 m/s, the ice cover shifts abruptly, contracting suddenly to 1070 m. At 13 m/s, another sharp contraction to 800 m occurs. From 17 to 21 m/s, the ice cover shows slight variations in length, ranging from 800 to 700 m. Between 21 and 23 m/s, a sharp shrinkage to 600 m is observed, followed by further shrinkage at 25 m/s.

The location of the double thickness of the ice cover highlights the wind's power in contracting the ice cover: the farther the ice shifts from the structure, the stronger the wind's contracting effect. For wind velocities below 13 m/s, double thickness is not observed. Between 13 and 15 m/s, the double thickness appears in the immediate vicinity of the structure. From 15 to 17 m/s, the double thickness reaches 71 m from the structure. Between 17 and 21 m/s, there is a slight increase to 164 m. A mild linear increase in the location of the double thickness occurs between 22 and 24 m/s, followed by decreases at 25 and 26 m/s.

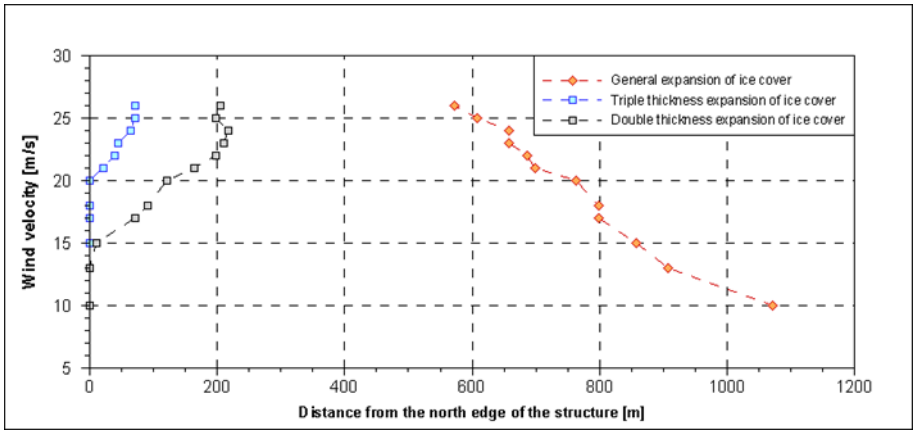

Figure 6- 5. Expansion of the ice cover, and the distance of the double, as well as triple ice thickness from the structure (Kolerski et al., 2021).

6.1.1 The effect of wind on polynya in Vistula Lagoon

This research was initiated and carried out by Professor Chubarenko from the Atlantic Branch of the P.P. Shirshov Institute of Oceanology, which is part of the Russian Academy of Sciences (IO RAS) and based in Kaliningrad, Russia. He is the head of the Laboratory of Coastal Systems, whose primary work focuses on numerical modelling of coastal lagoons and sediment transport. This research project was a collaboration between Gdańsk University of Technology and the Shirshov Institute, conducted without formal funding. Despite the promising results, the study was terminated due to political reasons.

The contact area of the inland water and the sea, coastal lagoons (inland shallow water bodies) can be formed as a transition zone of two flow regimes. Lagoons are separated from and connected to the ocean, by a barrier and at least one restricted inlet, respectively (Kolerski et al., 2019). Ice phenomena can be observed in Vistula Lagoon (southern part of the Baltic Sea). It happens usually, during the first 10 days of December. And, it fades in the late April or March that can be related to the specific western wind condition, leading to the ice drifting and accumulation (Girjatowicz, 2011). Figure 6- 6 illustrates the location of the Vistula Lagoon (Kolerski et al., 2019).

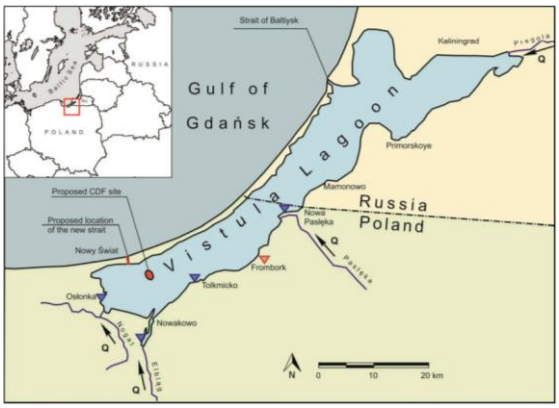

Figure 6- 6. Vistula Lagoon site in the Baltic Sea (Kolerski et al., 2019).

Vistula Lagoon is considered as one of the largest estuarine lagoons in Baltic Sea, with the average depth of 2.7 m, and the volume of 2.3 km^3. The main features of the ice phenomena in the Vistula Lagoon are, the periodical ice breakdowns, and the emergence of the polynya near the inlet. A polynya is defined as an opening of water in the ice (Zhelezova et al., 2018).

For this study, the polynya formation based on the water level data from the years between 2012 to 2013, was simulated with the DynaRICE model. The simulated model was calibrated with existing data for the polynya extension. Examples of calibration are presented in Figure 6- 7. In Figure 6- 7 (a1) and (b1) show the location of the polynya for March and February, respectively. The green dots indicate the polynya area based on field data, while the polynya area simulated by the DynaRICE model is shown with blue dashed lines outlined in black. Figure 6- 7 (a2) and (b2) illustrate the ice expansion along the polynya for March and February. The locations of the polynyas in the Vistula Lagoon are highlighted with a red circled boundary. It can be inferred that the locations of the polynyas, based on both numerical and field data, are generally consistent.

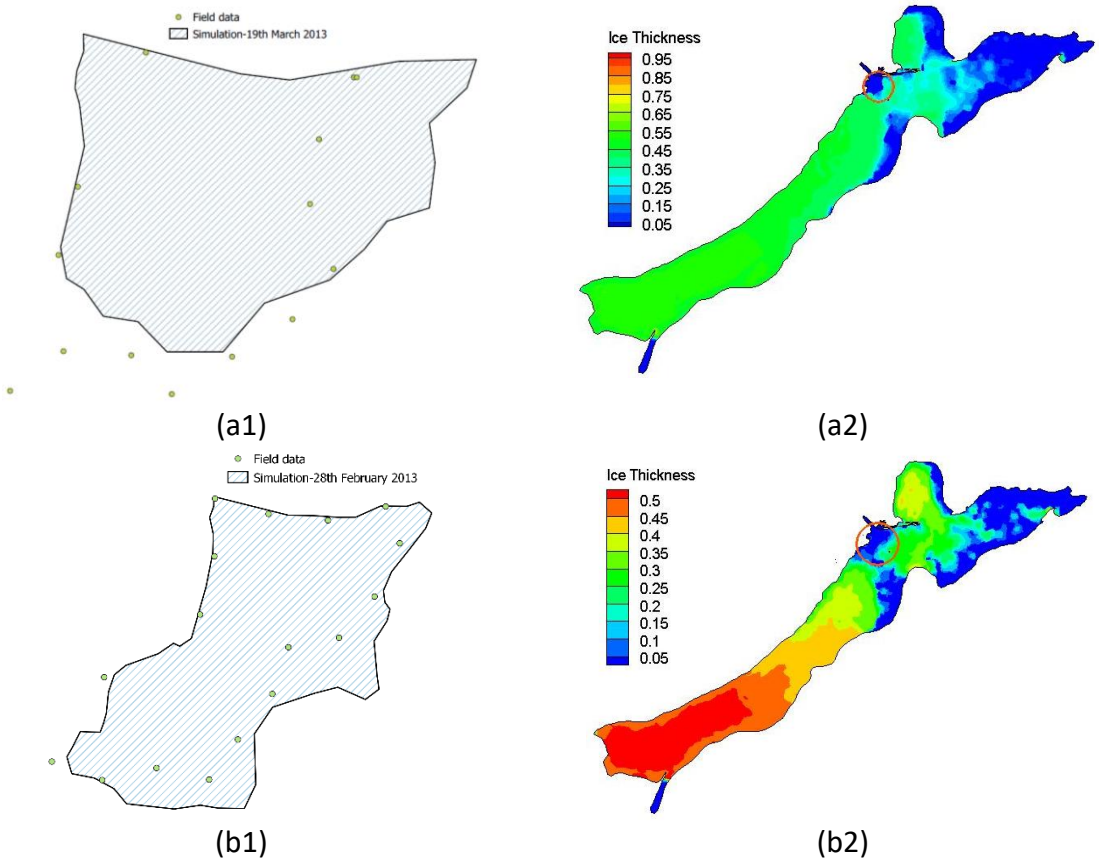

Figure 6- 7. Polynya calibration and ice expansion and thickness simulation along the Vistula Lagoon using the DynaRICE model: March 19th (a1 and a2) and February 28th (b1 and b2).

Based on Figure 6- 7 (a1) and (b1), the polynya area and location simulated by the DynaRICE model for February 28th closely resemble those observed in existing data. The simulated polynyas for both dates show greater similarity to real data on the left side of the polynya. In the March simulation, the bottom section of the polynya extends inward compared to the observed data, whereas in the February simulation, it extends further outward. The top sections of the simulated and observed polynyas for both February and March are well-aligned.

7 Summary of the results

The study is related to the wind effect on ice velocity. This study has advanced to some extent and should continue and proceed with further development. The experimental study was performed in the wave flume of the Institute of Hydro-Engineering of Polish Academy of Sciences (IHE PAS). In the experimental study wind and ice velocities were measured. The ice was simulated with polypropylene pallets and no thermal condition was considered. The considered length of the flume was 3.9 m and the height of the wind field above the water field was 0.2 m. A wind generator consisting of three fans would generate three different wind fields. This could be done by turning on one, two and three working fans. Two ice sizes were considered for the experiments (with rectangular shape): 10×10 cm as ice piece and 40×60 cm as ice cover. These both types of ice had a thickness of 1cm and a rectangular shape. For the size of 10×10 cm, concentration of ice was a varying parameter for the experiments. Initial water was used for the experiments, although water would find marginal velocities under the influence of wind (0.0049, 0.0052 and 0.035 m/s, respectively). For measuring wind and water velocity, PIV technique (Particle Image Velocimetry) and for ice velocity PTV technique (Particle Tracking Velocimetry) were used. The measurement of the wind velocity field was done from a side window (flume bank) and that of ice velocity from a top window.

PIV technique measures velocity vectors of seeding particles, which are captured from successive images. The velocity vector measurements were carried on by a Flow Master PIV system. For a two-dimensional PIV technique in the wind field, different materials were tested as seeding particles; water particles showed reliable results because they the requirements of the experiments and being aligned with the laboratory environment. The velocity of water particles as seeding material for the wind field was predominantly under the wind field influence and not under the influence of gravity effect. For the water field velocity measurement, using PIV technique, hollow glass spheres were used as seeding material, which were previously used in the laboratory (used for the experiments). After seeding the wind and water fields with water particles and hollow glass spheres, respectively, it was noticed the water fields was more homogenously seeded. The processing of raw data from PIV measurement was done with DAVIS software and the related data analysis was done with MATLAB.

PTV technique, which in this study is used for ice velocity measurement, is based on tracking routes of individual particles (ice pieces), as a function of displacement in time. The computations of the PTV technique were done with PTVlab software. The velocity of ice was measured under the influence of three wind fields (measured by PIV technique). Three ranges of ice concentration were considered: low, medium and high concentrations. Each experiment was repeated three times. Each PTVlab run for ice velocity computation would consider one wind velocity field and one ice concentration. Therefore, for each ice concentration range and wind velocity field, three PTVlab runs were performed; the maximum run time was 60 seconds.

DynaRICE model was used for numerical model simulation. The generated mesh was 20 m long. An optimized size for the mesh cells was chosen, based on the simulation time. Infinitesimal water discharge 0.0001 m^3/s and water level 0.595 m were considered at the upstream and downstream boundary hydrodynamic conditions. For an initial hydraulic condition, cold start runs in DynaRICE simulation were used with no ice condition. The initial conditions for considering wind effect were produced by hot runs in DynaRICE model, resulting in the desired ice concentrations observed in experimental simulation. Four ranges of ice concentrations were considered, low, medium and high. For each simulation with DynaRICE model, three sets of runs were needed. The runs were dedicated to obtaining hydrodynamic and ice initial conditions as well as wind conditions (final run). The wind velocities of 0.515, 1.166 and 1.499 m/s were considered for the simulations with DynaRICE model, which were based on measurements from experimental simulations. The averaged ice velocities for the wind velocities of 0.515, 1.166 and 1.499 m/s, varied within the ranges of 0.0075 to 0.0094 m/s, 0.021 to 0.022 m/s and 0.031 to 0.033 m/s, respectively (Figure 5- 6). The results from the DynaRICE model for different wind velocities versus ice concentration showed an overall trend of stabilization. For the same sequence of wind velocities, the averaged ice cover velocities were 0.003, 0.006 and 0.010 m/s, respectively.

For the PIV measurement, the time instance of 0.0018 s was considered for the measurement of velocity vectors. 900 images were obtained for each PIV measurement in the duration of 18 s. The velocity vectors were obtained from the movement of seeding particle materials. The velocity vectors in x direction were considered for this study.

For data analysis of velocity fields, at first a 3D matrix was considered to store the data. Three dimensions of the matrix were time, velocity vectors, different trials, and time. The averaged values of velocity vectors along the height of the fields and the averaged values of all trials were calculated (Figure 4- 1). The standard derivation values (STDE) showed marginal values for calculated averaged velocity values (Figure 4- 2).

To provide a more detailed analysis of the PIV measurement data, statistical analysis was utilized by grouping the entire data from different trials into one group to avoid the averaging effect (velocity averaged along the x-axis and over time). This way velocities varying along the y axis, referring to the height levels of the flume, would be obtained. It would provide the velocity data varying along the height of the flume. The velocities were arranged so that velocity range for each height level was obtained. Also, the averaged value of velocities for each height level was calculated. Negative wind velocity values from the PIV measurement could relate to the turbulence in the wind field, leading to directing the seeding particles to the opposite direction of the main wind stream. The most unified velocity graph along the height of the flume was related to the three working fans (Figure 4- 3 (c)). Smaller velocity values with negative direction were observed in the wind field related to the three working fans. It could be related to the lower **turbulence strengths** in this wind field compared to one working fan since the turbulence strength has a direct relation with the velocity of the wind field (Kolerski and Wielgat, 2014). The values related to the turbulence strength for this study are not directly measured, though.

To obtain more detailed statistical analysis, swarm plots were used, considering the number of replications of velocity values, at each height level, apiece (Figure 4- 4). The plots provide information for the density function (thickness of the plot) and absolute count from different trials (grey hue). The location of the maximum water discharge line, which provides seeding particle material, seems to be in the range of maximum repeating velocity values. **The closeness of the maximum water discharge to the mean wind velocity values (indicated by the red markers) shows the validity of assumption of steady and uniform flow**. It was noticed, the rearrangement of the nozzles, and to instal the nozzles along the longitudinal direction of the flume may assist to solve the issue of inhomogeneous seeding, which was observed the most in the wind field of one working fan. The averaged wind velocity values (averaged values of the red markers in Figure 4- 4 over the depth of the wind fields) for three

wind fields were 0.515, 1.166 and 1.499 m/s with calculated errors of 1%, 11% and 4%, consecutively. The results seem to be reliable for a low-budget experiment.

The PIV measurement for water velocity calculation showed the marginal velocity values and the average of 0.0049, 0.0052 and 0.035 m/s for one, two and three working fans, respectively (Figure 4- 5). As can be expected, the maximum water velocity values could be obtained at the adjacent vicinity of the water surface, which is at the immediate distance of the wind field. The negative velocity values at the water fields were also observed which seem to be due to the wind field effect; the negative velocity values were observed for the wind fields as well.

The velocity results from the PIV measurements were compared with those from the anemometer device, as the PIV technique in this laboratory had previously been applied only to measurements of water velocity fields. This could be considered as a comparison between invasive and non-invasive method. The measurement of the wind velocity was performed at the mid-length section of the wind field related to the PIV measurement. With the invasive method, there always can be the possibility of disturbing wind field, due to the intrusion of a measurement instrument to the field. The obtained measurement results from anemometer device showed the averaged velocity results (along the depth of the wind field) 0.52, 0.92 and 1.27 m/s for one, two and three working fans, respectively. **It could be understood that the averaged wind velocity results from the PIV measurement showed closeness to the same values from anemometer device**.

For the ice velocity measurement, PTV method was used. The ice velocity vectors were captured with the PTVlab software. The velocity measurement with this software was in a way that the tracers would be detected by the software (ice in this study). In this study, the averaged velocity related to a limited confined area around the location of the PIV measurement (wind field) was considered as the **first approach** of the ice velocity measurement (which is referred to in Figure 3- 25). To make it clearer, it can be said, wind and water measurement fields in this study are perpendicular and intersect each other. Therefore, the averaged velocity in this method pertains a limited area, not the entire field of measurement. The concentration of ice was determined by counting the ice pieces. Three ranges of low, medium and high concentrations were considered (Figure 4- 8). The averaged measured velocities (averaged ice area velocity) for ice pieces for three different wind fields, considering ice concentration changes, were ranged from 0.019 to 0.026 m/s for one working

fan; same ranges for two and three working fans were 0.029 to 0.035 and 0.035 to 0.041 m/s. **It could be noticed that based on the first approach for analysis of the ice velocity, with increasing the ice concentration, the ice velocity would generally decrease** (Figure 4- 8). Also, the averaged ice area velocity for the ice cover and for the two and three working fans were 0.0195 and 0.0265 m/s.

For the **second approach,** for analysis of the extracted data from PTVlab software, statistical analysis was performed for calculated velocity vectors (ice velocity fields). For conducting this analysis, the entire measurement field was considered (Figure 3- 17), and the data were put in a Matlab SQLite database. The data used in this analysis were obtained from the entire measurement field (velocity vectors from the entire coordinate of the domain) and not limited only to a part of it (Figure 4- 10). By which it means, all the velocity vectors from the entire domain were taken into account. The analysis was done for the velocity of ice pieces and covers. The velocity results are shown in Figure 4- 11 to Figure 4- 19, based on the repetition of velocity vectors. The peak repeated longitudinal ice velocity for each ice concentration and wind velocity field are shown in Table 4- 2 for ice pieces and Table 4- 3 for ice covers. **No relation between the ice concentration and velocity was observed, based on the second approach of ice velocity measurement. It was noticed that the inversed trend between ice velocity and ice concentration were obtained concerning merely the areas at the location of wind measurement field with PIV technique (second approach of the ice velocity measurement)**. The overall trend for the ice velocity versus concentration seemed to be unified, especially under the influence of the wind fields of two and three working fans.

The broken ice pieces velocities obtained from the approach that considered a limited ice velocity field generally showed larger values compared to the approach considered the entire ice velocity measurement field (Figure 5- 11). As wind velocity increases, the velocities of the ice pieces in both approaches show closer values.

In Figure 7- 1, the velocities of ice pieces are shown with varying ice concentrations for each wind field. The DynaRICE model velocities are represented by a red shade, while the PTV results, using the entire and limited, confined ice velocity fields, are shown in blue and black, respectively. Based on R squared values, the overall trends appeared linear; however, the trends for low wind field condition using limited confined area, and medium wind field using

the entire ice velocity field, as well as high wind field from the DynaRICE model exhibited a polynomial trend.

As seen in Figure 7- 1 for each wind field condition, the results from the DynaRICE model were closer to the PTV results using the entire wind field. Interestingly, at high concentration the results from PTV measurement using entire ice velocity field and limited confined area at each wind field, showed closer values compared to the lower concentrations. The reason could be that, at high concentration the difference between velocities using limited area and the entire ice velocity field were minimal. Additionally, the PTV-calculated ice velocities using limited confined area showed closer values to the numerical simulations in high wind field condition compared to the low and medium wind fields.

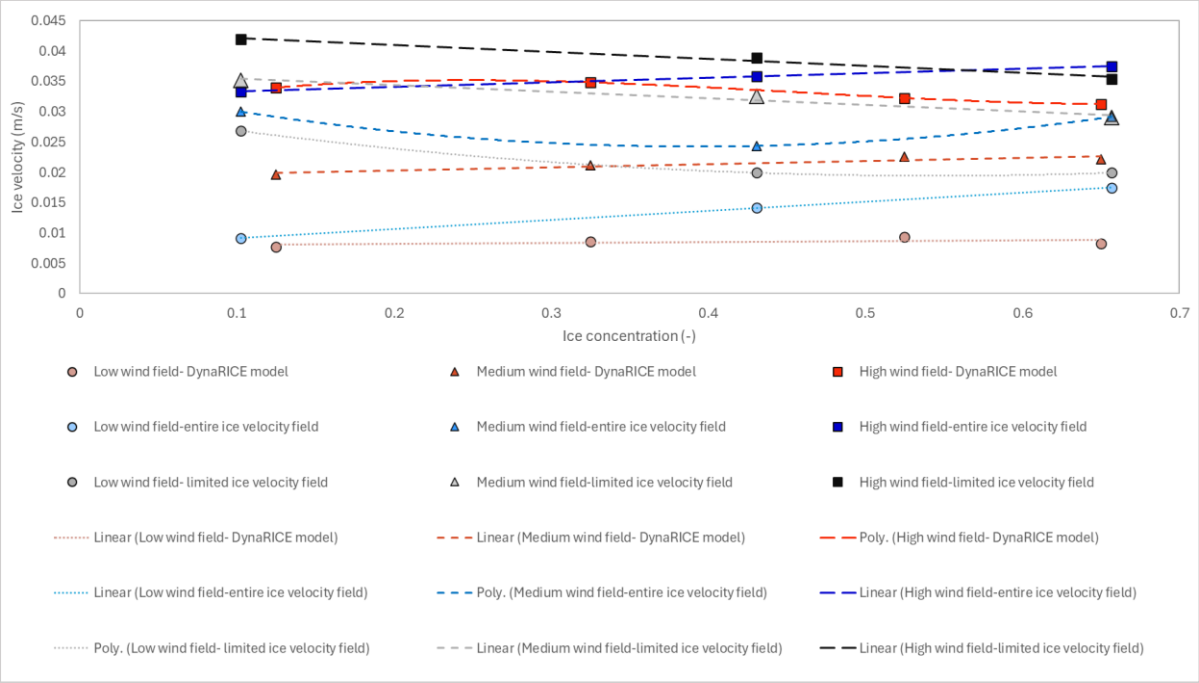

Figure 7- 1. The trends in the velocities of ice pieces, compared to ice concentration under different wind field conditions, obtained from the PTV calculations and the DynaRICE model.

For the ice cover velocity, the results related to the DynaRICE model were 0.0027, 0.0058 and 0.01 m/s for one working fan and two as well as three working fans, respectively. The experimental results for two and three working fans were 0.0091 and 0.0141 m/s. The ice cover velocity results from the DynaRICE model showed higher values compared to the results from experimental simulation (Figure 5- 10).

Based on the PTV analysis, the ice cover velocity exhibits lower values compared to the average ice pieces velocities under each wind field condition (Figure 5- 11). Ice cover remained stationary under low wind velocity conditions. As wind velocity increases, the ice cover velocities also rise, eventually reaching values comparable to those of the ice pieces, indicating that wind velocity has a greater impact on cover velocity. The difference between ice cover and ice pieces velocities is more pronounced when using the entire ice velocity measurement field, with the percentage difference being closer the results obtained from the DynaRICE model simulation. Furthermore, ice cover velocities were lower compared to the DynaRICE model results for each wind field condition. The DynaRICE model results for ice velocities were closer to the experimental results when using the entire ice velocity field (Figure 5- 10).

The averaged ice velocity results from all ice concentrations versus wind velocity related to the PTV calculations are provided in Figure 7- 2. In Figure 7- 2 (a) the averaged ice velocities with considering limited measurement filed and in Figure 7- 2 (b) those related to the entire measurement field are shown. The results are previously shown in Figure 4- 8 and Figure 4- 11 to Figure 4- 19.

As seen in Figure 7- 2 (a), which relates to the PTV calculations using limited confined area, the relationship between ice and wind velocities exhibits polynomial trends across all wind fields. However, the same relationship for average ice velocities, when using the entire ice velocity field and averaging across the entire ice concentrations (as shown in Figure 7- 2 (b)) follows a linear trend. In contrast, within Figure 7- 2 (b), the trends for ice-wind velocity corresponding to each individual ice concentration do not exhibit a linear trend, though the overall average displays a linear trend when the data are synergised.

Comparing the average ice velocity equation trends (indicated by black lines), it can be observed that the coefficient of x^2 in the equation corresponding to the limited confined area (polynomial trend in Figure 7- 2 (a)) is similar in value to the coefficient of x in the linear trend for the entire ice velocity field (linear trend in Figure 7- 2 (b)). It is also noticeable that at low wind velocities, both approaches for PTV calculations (using limited confined area and the entire ice velocity field) may show similar trend, when considering the average velocities of all ice concentrations. However, it is speculated that at higher wind velocities (higher than the range of this study) the ice velocity results from the PTV calculations related to limited

confined area (polynomial trend) change more significantly with wind velocity compared to when using the entire ice velocity field (linear trend).

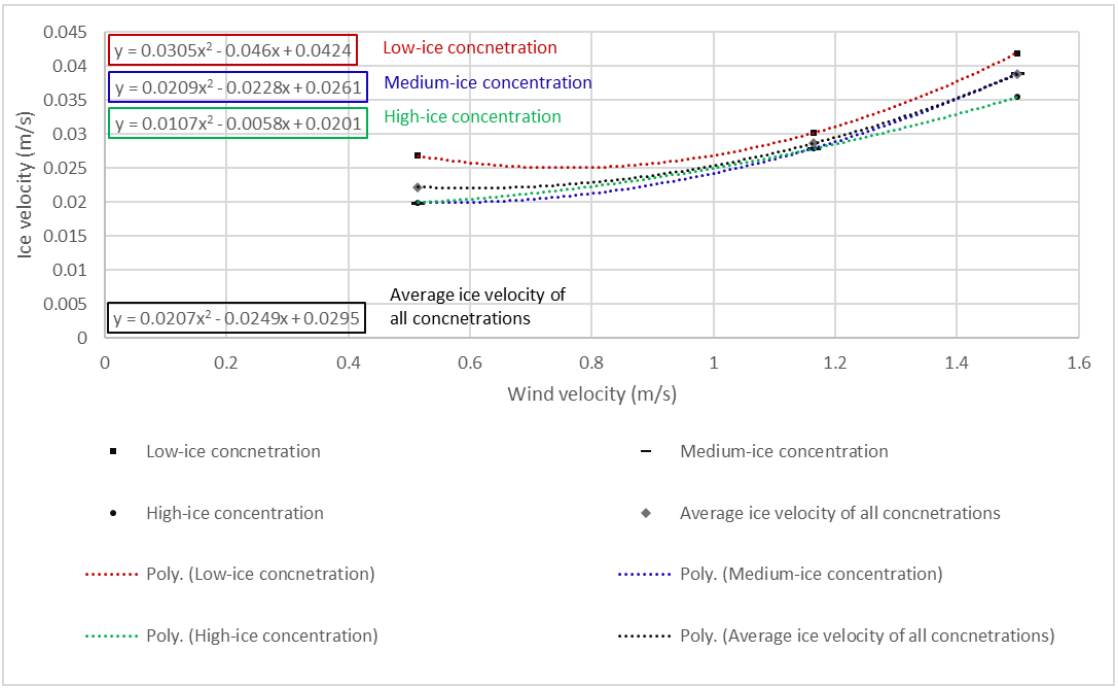

(a)

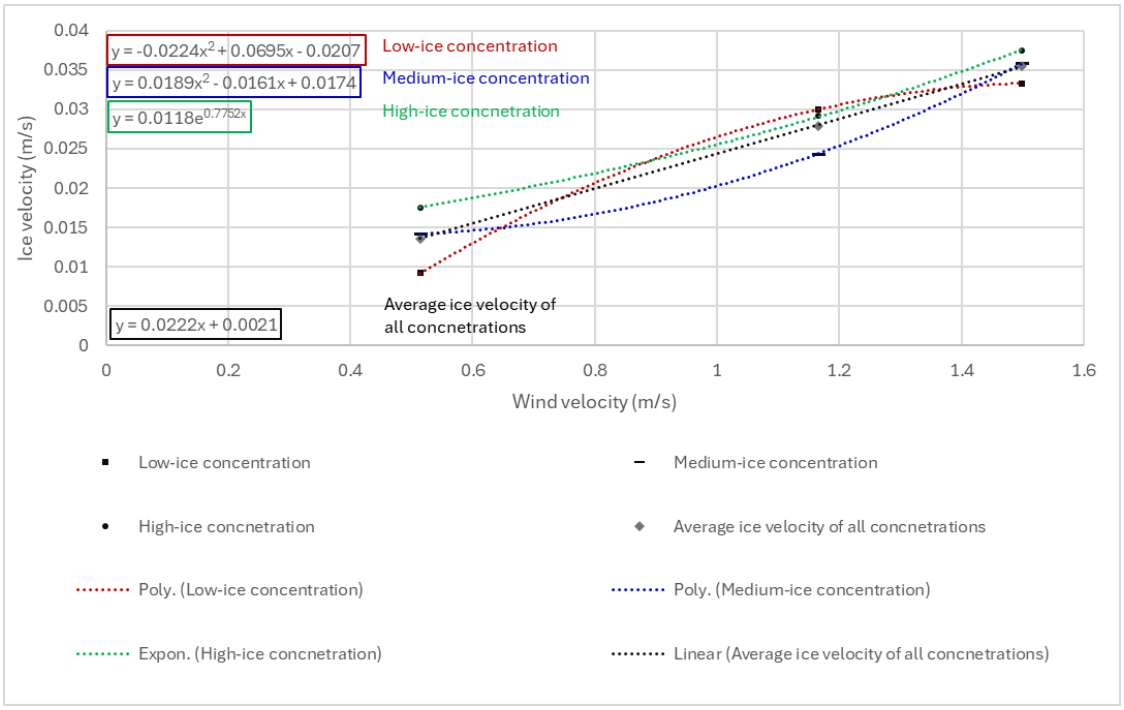

(b)

Figure 7- 2. The relationship between ice velocity and wind velocity for ice pieces using limited area (a) and entire measurement field (b)

Ice velocity results obtained from using a limited area and the entire measurement field showed that the relationship between ice concentration and velocity is observed only in the former. It can be noted that using the limited ice velocity area, which is adjacent to the wind velocity measurement field, appears to be more reliable than the approach that considers the entire ice velocity measurement field. Using the entire measurement field reduces the ice velocity to a noticeable extent, which is primarily due to areas located at a significant distance from the PIV measurement field (for wind velocity measurements).

Moving to the vertical wind distribution over the surface, the logarithmic trend of wind velocity (as expected based on (Wu, 1973)) was clearly observed for the high wind velocity in the experimental modelling (Figure 5- 12). For high wind velocity, the value of the wind drag coefficient (C_a) obtained from the logarithmic wind velocity profile was 2×10^{-4}. This small value, compared to the expected range for the wind drag coefficient, was attributed to the low wind velocity and the influence of the upper boundary of the flume (flume ceiling).

By adjusting the wind drag coefficient in the DynaRICE model from 0.0015 to 0.002, 0.0025, and 0.009 for high, medium, and low wind velocities, respectively (Table 5- 1), the ice velocity results from the DynaRICE model more closely aligned with the ice velocity results from the experimental simulation. Wind velocities above 2 m/s primarily affect ice dynamics, indicating that the default value of 0.0015 for the wind drag coefficient is appropriately applied in the DynaRICE model. However, further improvement could be achieved by accounting for changes in the wind drag coefficient under the entire range of wind velocity conditions within the DynaRICE model.

The following is the summary of the results of the study:

- The effect of wind plays an important role in the ice processes in cold regions. Therefore, in this study the effect of wind on ice was considered. The current formulation for wind effect does not include specific characteristics of ice, e.g., size and thickness.
- The study relates to the wind effect on ice velocity. Changing parameters for this study are wind velocity, ice size, and ice concentration.
- The experiments related to this study were done in a wave flume at Institute of Hydro-Engineering of Polish Academy of Sciences. The water section of the flume (3.9 m long)

was used for locating ice above the water surface (0.595 m). A wind flume was designed and installed above the water surface (0.2 m).

- PIV technique was used for measuring wind and water velocity and PTV technique for measuring ice velocity.
- For the PIV technique, seeding the measurement field was required. Seeding gas fields is usually more problematic than seeding liquid fields. A number of tests were conducted on different seeding materials in the wind fields. The results showed that water particles met the requirements of this study, in terms of ease of use, lack of pollution or corruption, and sufficient dispersion in the wind field. Performing PIV measurement experiments on water particles showed they were not majorly under the gravity effect. Seeding the water fields by hollow glass spheres left the water fields more homogenously seeded compared to the seeded wind fields with water particles. Although, using water particles as a seeding material in the wind fields may result in reliable velocity measurements. For the future wind velocity measurements, modification in the location and number of wind generators and water sprays are recommended. It is recommended that wind generators and water sprays be in a longitudinal direction along the flume.
- For analysing the results of the PIV measurement, statistical analysis was performed in MATLAB. As the final attempt, the histogram bin counts at each height level of the wind field were used, to allocated velocities to various ranges. This provided information related to the repetition of the velocity values.
- Three wind velocity fields were considered: Low, medium and high. With the PIV technique measurement. The measured wind velocities with PIV technique were 0.515, 1.166 and 1.499 m/s, respectively. The error values for wind velocity measurement were 1%, 11% and 4% for one, two and three working fans, respectively, which seem reliable for a low-budget experiment. Comparing the PIV wind velocity measurement results (non-invasive) with the results from the invasive measurement (anemometer device) showed the results from the PIV measurement using water particles as seeding material are reliable. For the future experiments it is recommended to provide continuous ranges of wind fields. As the current study used wind fields with one, two and three working fans.

- Marginal water velocities of 0.0049, 0.0052 and 0.035 m/s were obtained under the wind influences of one, two and three working fans, respectively as measured by the PIV technique.
- For ice velocity measurement, PTV technique was used, utilizing the top view of the flume for the measurement. The wind and ice velocity measurement fields were perpendicular to each other. The ice concentration was captured by counting the ice pieces, taking into account three ranges of ice concentration: low, medium and high. The analysis of the results was done in PTVlab software. Averaging ice velocity over a limited area of measurement field, generally led to an inverse relationship between ice concentration and velocity.
- Using a limited confined area for the velocity measurement of ice pieces (**first approach** of ice velocity measurement) resulted in an inverse correlation between ice velocity and concentration. Generally, the velocity of ice pieces from the PTV calculation, when using a limited confined area showed higher values compared to the results obtained from the entire ice velocity field. However, as wind velocity increased, the PTV results from both the entire ice velocity field and limited confined area converged to more similar values. Additionally, at high wind field, the velocity of ice pieces in the limited confined area showed closer values to the DynaRICE model results compared to the results at low and medium wind fields.
- Performing statistical analysis of PTV measurement of ice velocity using the entire measurement field (MATLAB SQLite database, referred to in the **second approach** of the ice velocity measurement) resulted in no observed relationship between ice velocity and concentration. A generally consistent trend in the relationship between ice concentration and velocity was observed, especially for the wind velocities related to the operation of two and three fans. It can be noticed that considering the entire ice velocity measurement field, the ice concentration did not significantly affect the ice velocities.
- The relationship between ice velocity, averaged across ice concentration, and wind velocity (related to the PTV calculations) showed linear trend when using the entire ice velocity field, and a polynomial trend when using limited confined area Figure 7- 2.

It is speculated that within the range of wind velocities considered in this study, both trends exhibit more similar values compared to the higher velocity ranges.

- In the simulation with the DynaRICE model, for the wind fields generated by one, two and three working fans the average ice velocities varied in the ranges of 0.0075 to 0.0094 m/s, 0.021 to 0.022 m/s and 0.031 to 0.033 m/s. The linear trend in the relationship between ice concentration and velocity indicated an overall stabilization. The velocity of ice pieces related to the DynaRICE model at each wind field showed lower values compared to the PTV calculations using the entire ice velocity field and limited confined area. These velocity results from the DynaRICE model showed values closer to the PTV calculation when using the entire ice velocity field, compared to the limited confined area.
- The ice cover velocity showed a smaller range compared to those of ice pieces under each wind field. Using the entire ice velocity field revealed greater velocity differences between the ice cover and ice pieces— 67% and 60% for two and three working fans, respectively. These values were closer to the results from the DynaRICE model (72% and 68%) compared to those from the approach using a limited, confined area (39% and 31%).
- The experimental ice cover velocities, based on the entire ice velocity field, showed a linear distribution with varying wind fields, and a logarithmic distribution when using a limited, confined area. The trend of ice cover velocities using the DynaRICE model followed a polynomial distribution. The average velocities, using the entire ice velocity field and the limited, confined area showed differences of 18% and 58% with the results from the DynaRICE model, respectively.
- Considering both approaches for analysing the ice velocity results from PTV measurements, it was observed that using a limited area provides more reliable results, based on the location of the considered area being adjacent to the wind velocity measurement field. Additionally, using the entire ice velocity measurement field resulted in a decrease in ice velocities. This decrease in ice velocity was attributed to areas located at a greater distance from the wind velocity measurement field. Therefore, using a limited area adjacent to the wind velocity measurement field is the preferred approach for analysing ice velocity results from PTV measurements.

- By adjusting the wind drag coefficient in the DynaRICE model to achieve results closer to the experimental simulation, slightly higher values (0.002 and 0.0025) were obtained for high and medium wind velocities compared to the baseline value of 0.0015 typically used in the DynaRICE model. However, for the low wind velocity, a much higher value (0.009) was obtained. This indicates that the wind drag coefficient varies with different wind velocities. Generally, the lower the wind velocity, the higher the wind drag coefficient. This indicates that, in this approach, low wind velocity does not effectively drag the ice.
- The real-case scenarios serve as practical implementations of the DynaRICE model, showing its capability to predict ice forces on structures and ice dynamics in estuaries. The photovoltaic scenario focused on ice forces affecting a floating structure (PV) caused by ice jams under wind influence in the Łapino reservoir. This analysis revealed that wind significantly contributes to ice jams, resulting in normal and tangential forces on structure elements. For example, a northward wind of 26 m/s caused a significant shove-induced ice jam, leading to fluctuating forces on the structure. This study reveals the importance of considering wind forces when designing structures in ice-prone regions.
- The polynya scenario examined the formation of polynyas in the Vistula Lagoon under wind influence, comparing the results with field data. In this lagoon, the formation of polynyas within the seasonal ice is expected. The comparison of the location and size of the simulated polynya using the DynaRICE model with field observations for both February and March showed a close match. This simulation demonstrated the model's capability in predicting lagoon hydrodynamics and ice cover shifts driven by wind, which can affect the navigation and shore protection in the lagoon area. By accurately capturing polynya and ice cover dynamics, the DynaRICE model provides valuable understanding of seasonal ice behaviour, which is crucial for ice mapping.

8 Conclusions

In conclusion, this study investigates the effect of wind on ice velocity, with an emphasis on ice concentration, size and wind velocity. At this stage, the study is at a basic level and requires further improvement. The study applied PIV (Particle Image Velocity) and PTV (Particle Tracking Velocimetry) techniques. Using these techniques, reliable wind, water and ice velocities were obtained.

The categorization of the data from the PIV measurements were found to be optimal for achieving the study's goal of determining a range for wind velocity. For the data from the PTV measurement, using the averaged ice velocity data from around the location of the PIV measurement appeared to be optimal in relation to the ice concentration. The water velocities showed marginal values under the wind field conditions.

The experiments conducted in a wave flume showed that the wind velocity has noticeable impact on ice velocity. The wind velocity has impact on ice drift through the surface ice concentration. The relationship between ice concentration and ice velocity for the averaged ice velocity, generally showed an inverse linear trend. The calculated ice velocity using the DynaRICE model generally showed linear constant ice velocity relationship with ice concentration. It appears that the ice concentration parameter may not have a strong effect on the ice velocity when using the DynaRICE model.

The DynaRICe model was used to simulate the wind effect on ice movement with the default parameters, including wind drag coefficient (0.0015). The velocity results for the ice pieces from the DynaRICE model showed lower values compared to the experimental simulations. The ice velocities from the DynaRICE model and PTV calculation using limited confined area aligned more closely at higher wind velocity. The ice velocity results from PTV calculations showed closer values at high ice concentration.

The relationship between averaged ice-wind velocities across all concentrations from the PTV calculations exhibited a polynomial trend. The averaged ice velocities across all concentrations for different wind fields showed similar trends in the velocity range of this study (Figure 7- 2 (a)). It is speculated that the averaged ice velocities across all concentrations

exhibited strong changes with increasing wind velocity (higher than the wind velocity ranges of this study).

For the larger ice pieces which are considered as a broken ice cover in the experiments, the velocities were lower than those of the ice pieces under each wind field, indicating that the ice cover is less influenced by wind velocity compared to the smaller ice pieces. For ice cover velocity under different wind field conditions, the results from the experimental modelling generally showed higher values compared to the DynaRICE model simulation, with a larger difference between averaged values. It can be expected that, with the increase in wind velocity, the experimental ice cover velocity growth decreases.

The profile for the measured wind velocity (red signs in Figure 4- 4) showed that it follows a logarithmic trend (Figure 5- 12), typically used for wind velocity profiles in wind-sea interactions. The logarithmic trend was observed for high wind velocity near the water surface. The logarithmic trend was not consistent across other conditions (low and medium wind velocities), which is because of the dominant effect of the immovable ceiling. The wind-ice interaction formulation and wind drag coefficient in the DynaRICE model are derived from sea ice formulations which relates to higher wind velocity range compared to that used in this study. This may lead to the differences between the ice velocity results from the DynaRICE model and the experimental results. To reach closer ice velocity results from the DynaRICE model to those of experimental modelling, the wind drag coefficient was adjusted. The adjusted wind drag coefficient in the DynaRICE model showed higher values for low wind velocities compared to medium and high wind velocities. It suggests that wind velocity influences the wind drag coefficient, in the way that the lower the wind velocity the higher the wind drag coefficient. It means for the high wind velocities (higher than the range used in this study) the value of the default wind drag coefficient used in the DynaRICE model should not be changed.

The results of the experiments along with the obtained error ranges confirmed the reliability of the PIV measurements, using the water particles as seeding material. It is important to optimize the wind field measurement for future experiments. Future work should focus on testing the continuous and higher wind velocity ranges and refining the experimental setup to enhance the understanding of wind-ice velocity measurements.

The DynaRICE model simulations for the real-case scenarios confirm the model's effectiveness in capturing ice behaviour under varying wind conditions. For all the simulations, the model parameters, including the wind drag coefficient, are set to their default values. In the photovoltaic scenario, the model accurately simulated the wind-driven ice forces exerted on structural elements, providing useful insights for optimizing floating structure designs in cold regions. This demonstrates the model's resilience and applicability for infrastructure and environmental management. The results indicate that wind significantly influences force distribution along the structure, particularly due to ice jams and the forces they exert. These findings underscore the importance of considering wind dynamics and associated risks in structural design for cold environments. It is worth noting that the scenarios are based on the extreme wind speed to demonstrate the maximum load on the structure. For such high wind, the default drag coefficient should be used.

Additionally, the Vistula Lagoon scenario demonstrated that the DynaRICE model effectively simulates polynya formation under wind conditions from field data. The alignment between the model’s simulation of polynya location and extent and the observed ice expansion data highlights the model's capability in replicating ice phenomena in estuarine lagoons. By closely reproducing the location and extent of polynyas, the model offers valuable insights into ice dynamics critical for protecting the shore of the lagoons from wind-driven ice movements.

These two real-case scenarios illustrate the model's robustness in predicting diverse ice conditions under wind influence, emphasizing the importance of continued refinement of wind-ice velocity studies in both laboratory and real-world scenarios. The ice dynamics is mainly affected by the wind with higher magnitude (above 2 m/s), which means the default value of the wind coefficient is properly used. However, updating the model by the variation of the wind drag coefficient with the wind velocity will be valuable improvement to see a comprehensive understanding.

Appendices

Appendix (A)

In Appendix (A), narrowed down quantile ranges of 2.5% to 97.5% (of the data) is shown on the figures for the wind fields of two and three working fans. The lower range (0.25% of data) and higher range (0.95% of data) are indicated by orange and blue circles, respectively (Figure 9- 1).

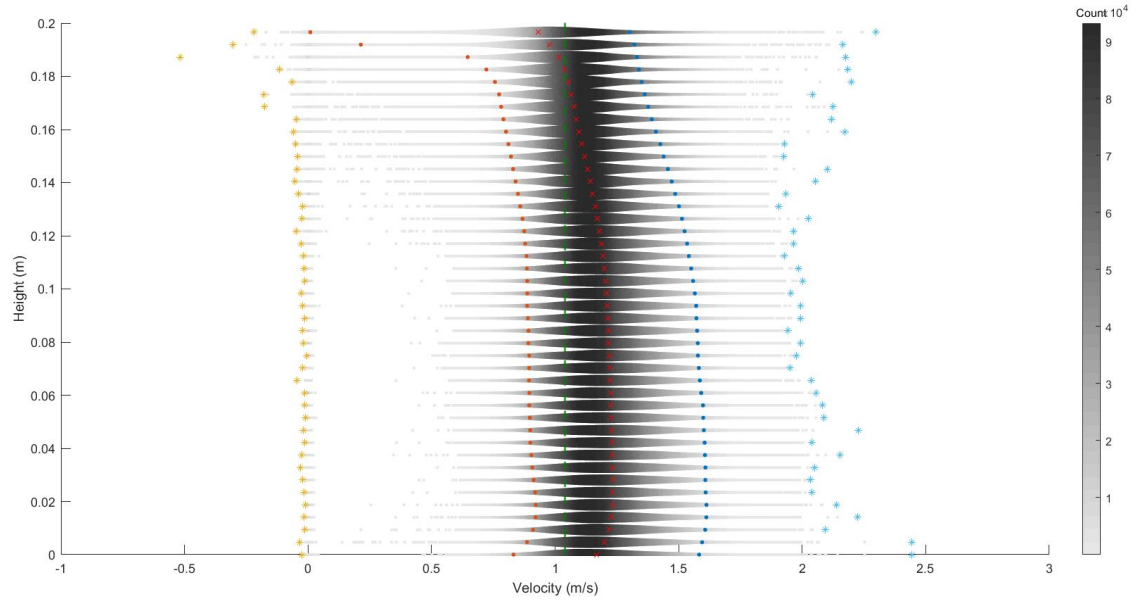

(a)

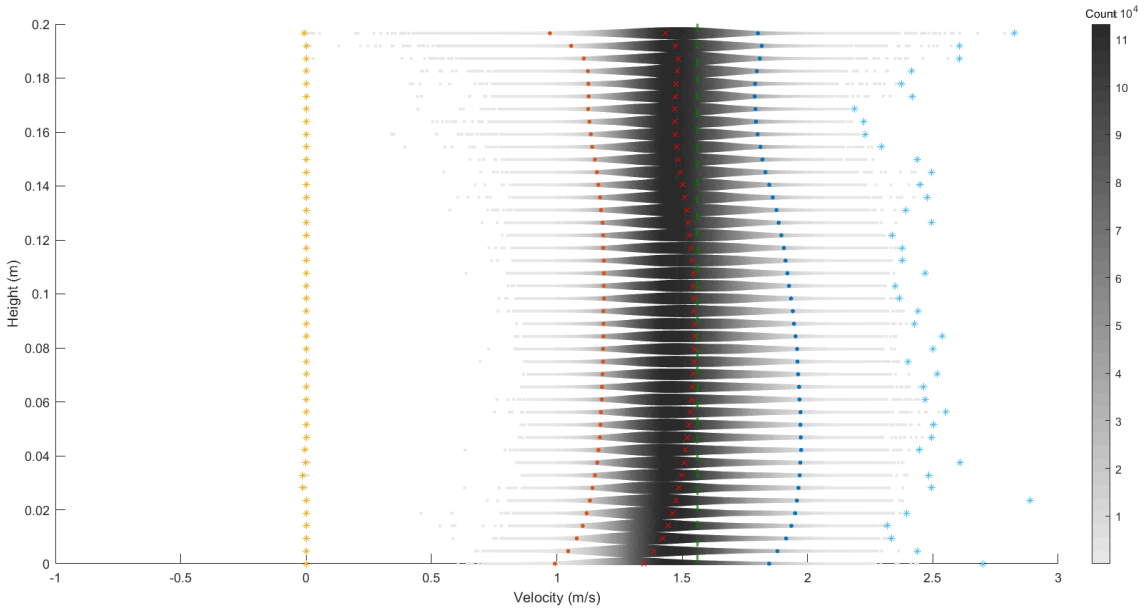

(b)

Figure 9- 1. The wind velocity fields for two (a), three (b) working fans with the quantile range of 0.25% to 0.75% with orange and blue indicators.

Appendix (B)

A table of symbols is provided in Appendix (B), listed in the order of their appearance.

Table 9- 1. Table of symbols.

u_a	Measured wind velocity at y elevation distance from the water surface
$(u_*)_a$	Wind shear velocity
K	Karman universal constant
k	Roughness depth of water
ρ_a	Air density
C_y	Wind velocity coefficient
U_y	Measured wind velocity at an anemometer height of y, from the water surface
d	Dynamic roughness of water surface
$\mathrm{F_H}$	Horizontal forces on an ice boom
$\mathrm{F_{current}}$	Current force on an ice boom
$\mathrm{F_{wind}}$	Wind force on an ice boom
$\mathrm{M_i}$	Mass density of ice
ρ_i	Density of ice
N	Concentration of ice
$\mathrm{t_i}$	Thickness of ice
$\vec{\mathrm{V}}_\mathrm{i}$	Ice velocity
t	Time
$\vec{\mathrm{R}}$	Internal ice resistance
$\vec{\mathrm{F}}_\mathrm{a}$	Wind drag force
$\vec{\mathrm{F}}_\mathrm{w}$	Water drag
$\vec{\mathrm{G}}$	Gravitational force
ρ_a	Air density
$\mathrm{C_a}$	Wind drag on ice coefficient
$\vec{\mathrm{W}}$	Wind speed at 10 m level above water surface
ρ	Water density
$\mathrm{C_w}$	water-on-ice drag coefficient
$\vec{\mathrm{V}}_\mathrm{w}$	Depth-averaged water velocity at the bottom of ice
u	Ice velocity component in the x direction
v	Ice velocity component in the y direction
$\mathrm{u_w}$	Water velocity component in the x direction
$\mathrm{v_w}$	Water velocity component in the y direction
σ_{xx}	Normal stress components
σ_{yy}	Shear stress components
η	Water surface elevation

t_i	Thickness of ice rubble
t_2	Submerged thickness of ice rubble
e	Ice porosity
Z	Distance from water for ice rubble
g	Gravitational acceleration
τ_f	Shear stress on the failure plane
σ	Normal stress on the failure plane
c	Cohesion on the failure plane
$\emptyset$	Internal friction angle of a failed material
θ	Failure angle
σ_3	Maximum stress on a failure plane
σ_1	Minimum stress on a failure plane
σ_h	Horizontal effective pressure
σ_o	Vertical effective pressure
k_o	At-rest coefficient of lateral pressure
k_a	Active coefficient for horizontal hydrostatic pressure
k_p	Passive coefficient for horizontal hydrostatic pressure
j	Empirical constant for tension imposed on ice
N_{max}	Maximum ice concentration
$\tau_s^{(i-a)}$	Shear stress imposed on ice by wind
$\mathrm{C_a}$	Wind drag coefficient on ice
$\overrightarrow{v_a}$	Wind velcoity
l	Smoothing length
l_*	Smoothing length from previous time step
n	Number of steps
Δt	Time step
$\vec{v}$	Parcel velocity
M_0	Initial mass density
l_0	Initial smoothing length
m	Mass of each ice parcel
ΔA	Size of the ice parcel
Δx	Parcel size in x direction
Δy	Parcel size in y direction
l_x	Smoothing length in x direction
l_y	Smoothing length in y direction
lU	Longitudinal wind velocity vector in PIV technique
$\overline{\mathrm{IU}}$	Average of longitudinal wind velocity vector in PIV technique
Q	Number of longitudinal wind velocity vector in PIV technique
z	Distance from the water surface
$u_{(z)}$	Wind velocities at height z based on logarithmic law

Acknowledgements

A tribute is paid to the Institute of Hydroengineering, Polish Academy of Sciences for their immense help for organizing and conducting the experiments. I would also like to thank Dr. Maciej Paprota and Dr. Wojciech Artichowicz as well as Prof. Boris Chubarenko for their invaluable support and expertise for carrying out this study.

I am profoundly grateful to my supervisor, Tomasz Kolerski, for his steadfast support, acknowledgment, and guidance throughout my studies, which kindled an incandescent enthusiasm for my research. From the beginning, he supported me with his extensive knowledge, patience, and understanding, making this journey both joyful and easier.

I know I have been fortunate to find Tomasz and to experience a new beginning under his supervision. His belief in me helped me to believe in myself during tough times. His mentorship has enlightened my career. Words fail to fully capture the depth of my gratitude, but I will remain forever thankful.

References

Adrian, R.J., 2005. Twenty years of particle image velocimetry. Experiments in Fluids.

Adrian, R.J., 1991. Particle-imaging techniques for experimental fluid mechanics. Annual review of fluid mechanics 23, 261–304.

Adrian, R.J., Westerweel, J., 2011. Particle image velocimetry. Cambridge university press.

Ashton, G.D., 1986. River and lake ice engineering. Water Resources Publication.

Asvall, R.P., 2007. Selective withdrawal to reduce regulation effects on ice cover downstream outlet of Alta power plant, in: 14th Workshop on the Hydraulics of Ice Covered Rivers, Québec, Canada–2007.

Beltaos, S., 2003. Threshold between mechanical and thermal breakup of river ice cover. Cold Regions Science and Technology 37, 1–13.

Beltaos, S., Prowse, T., 2009. River-ice hydrology in a shrinking cryosphere. Hydrological Processes: An International Journal 23, 122–144.

Biegowski, J., Paprota, M., Sulisz, W., 2020. Particle image velocimetry measurements of flow over an Ogee-Type Weir in a hydraulic flume. International Journal of Civil Engineering 18, 1451–1462.

Brevis, W., Niño, Y., Jirka, G.H., 2011. Integrating cross-correlation and relaxation algorithms for particle tracking velocimetry. Experiments in Fluids 50, 135–147.

Carson, R., Beltaos, S., Groeneveld, J., Healy, D., She, Y., Malenchak, J., Morris, M., Saucet, J.-P., Kolerski, T., Shen, H.T., 2011. Comparative testing of numerical models of river ice jams. Canadian Journal of Civil Engineering 38, 669–678.

Carter, D., Sodhi, D., Stander, E., Caron, O., Quach, T., 1998. Ice thrust in reservoirs. Journal of cold regions engineering 12, 169–183.

Creutin, J.D., Muste, M., Bradley, A.A., Kim, S.C., Kruger, A., 2003. River gauging using PIV techniques: a proof of concept experiment on the Iowa River. Journal of Hydrology 277, 182–194.

Crissman, R., Abdelnour, R., Shen, H.T., 1995. Design alternatives for the Lake Erie-Niagara River ice boom, in: 8th Workshop on River Ice, Kamloops, BC, Canada.

Dal Sasso, S.F., Pizarro, A., Manfreda, S., 2020. Metrics for the quantification of seeding characteristics to enhance image velocimetry performance in rivers. Remote Sensing 12, 1789.

Das, B.M., Sobhan, K., 2012. Principles of Geotechnical Engineering .(p. 666).

Essel, E.E., Clark, S.P., Dow, K., Tachie, M.F., 2021. Experimental and numerical investigation of three-dimensional open channel with simulated partial ice-covers. Journal of Hydraulic Research 59, 977–988.

Ettema, R., Fujita, I., Muste, M., Kruger, A., 1997. Particle-image velocimetry for whole-field measurement of ice velocities. Cold Regions Science and Technology 26, 97–112.

Evers, K.-U., Shen, H.H., Dai, M., Yuan, Y., Kolerski, T., Wilkinson, J., 2002. A twin wave tank pancake ice growth experiment. Presented at the Proceedings of the 16th IAHR International Symposium on Ice, Dunedin, New Zealand, pp. 12–16.

Fujita, I., Muste, M., Kruger, A., 1998. Large-scale particle image velocimetry for flow analysis in hydraulic engineering applications. Journal of hydraulic Research 36, 397–414.

Gebre, S., Alfredsen, K., Lia, L., Stickler, M., Tesaker, E., 2013. Review of ice effects on hydropower systems. Journal of Cold Regions Engineering 27, 196–222.

Girjatowicz, J.P., 2011. Ice conditions on the southern Baltic Sea coast. Journal of Cold Regions Engineering 25, 1–15.

Guest, P.S., Davidson, K.L., 1991. The aerodynamic roughness of different types of sea ice. Journal of Geophysical Research: Oceans 96, 4709–4721.

Hammar, L., Shen, H.T., 1995. Frazil evolution in channels. Journal of Hydraulic Research 33, 291–306.

Hammar, L., Shen, H.T., Evers, K.U., Kolerski, T., Yuan, Y., Sobczak, L., 2002. A laboratory study on freeze up ice runs in river channels, in: Ice in the Environments: Proceedings of 16th International Association of Hydraulic Research Symposium on Ice. pp. 36–39.
Hardalupas, Y., Sahu, S., Taylor, A.M., Zarogoulidis, K., 2010. Simultaneous planar measurement of droplet velocity and size with gas phase velocities in a spray by combined ILIDS and PIV techniques. Experiments in fluids 49, 417–434.
Haynes, F.D., Sodhi, D.S., Kato, K., Hirayama, K., 1983. Ice forces on model bridge piers. COLD REGIONS RESEARCH AND ENGINEERING LAB HANOVER NH.
Hopkins, M.A., Tuthill, A.M., 2002. Ice boom simulations and experiments. Journal of cold regions engineering 16, 138–155.
Høyland, K.V., Nord, T.S., Turner, J., Hornnes, V., Gedikli, E.D., Bjerkås, M., Hendrikse, H., Hammer, T., Ziemer, G., 2021. Fatigue damage from dynamic ice action-The FATICE project. Presented at the Proceedings of the 26th International Conference on Port and Ocean Engineering under Arctic Conditions: June 14-18, 2021, Moscow, Russia.
Huang, F., Shen, H.T., Knack, I., 2012. Modeling Border Ice Formation and Cover Progression in Rivers, in: Proceedings of the 21st IAHR International Symposium on Ice, Dalian, China.
Husted, B.P., Petersson, P., Lund, I., Holmstedt, G., 2009. Comparison of PIV and PDA droplet velocity measurement techniques on two high-pressure water mist nozzles. Fire safety journal 44, 1030–1045.
Ji, S., Liu, L., Ji, S., Liu, L., 2020. Contact Force Models for Granular Materials. Computational Granular Mechanics and Its Engineering Applications 51–96.
Jodeau, M., Hauet, A., Paquier, A., Le Coz, J., Dramais, G., 2008. Application and evaluation of LS-PIV technique for the monitoring of river surface velocities in high flow conditions. Flow Measurement and Instrumentation 19, 117–127.
Jones, S.J., McKenna, R.F., Tillotson, J., Jordaan, I.J., 2012. Ice-Structure Interaction: IUTAM/IAHR Symposium St. John's, Newfoundland Canada 1989. Springer Science & Business Media.
Knack, I.M., Shen, H.T., 2017. Numerical modeling of ice transport in channels with river restoration structures. Can. J. Civ. Eng. 44, 813–819. https://doi.org/10.1139/cjce-2017-0081
Kolerski, T., Radan, P., 2022. The Application of the Thermal Stabilization Prompted by the Ice Cover Expansion Considering the Energy Production Optimization in the Dam-Reservoir Coupled Systems on the Vistula River. Energies 15, 823.
Kolerski, T., Radan, P., Gąsiorowski, D., 2021. Ice Load Characteristics on Floating Photovoltaic Platform. Energies 14, 2466.
Kolerski, T., Shen, H.T., 2015. Possible effects of the 1984 St. Clair River ice jam on bed changes. Canadian Journal of Civil Engineering 42, 696–703.
Kolerski, T., Shen, H.T., Kioka, S., 2013. A numerical model study on ice boom in a coastal lake. Journal of Coastal Research 29, 177–186.
Kolerski, T., Wielgat, P., 2014. Velocity field characteristics at the inlet to a pipe culvert. Archives of Hydro-Engineering and Environmental Mechanics 61, 127–140.
Kolerski, T., Zima, P., Szydłowski, M., 2019. Mathematical modeling of ice thrusting on the shore of the Vistula Lagoon (Baltic Sea) and the proposed artificial island. Water 11, 2297.
Kołodko, J., Jackowski, B., 1984. Ice Floods Caused by Wind Action, in: Channels and Channel Control Structures: Proceedings of the 1st International Conference on Hydraulic Design in Water Resources Engineering: Channels and Channel Control Structures, University of Southampton, April 1984. Springer, pp. 439–444.
Lal, A.W., Shen, H.T., 1993. A mathematical model for river ice processes. US Army Corps of Engineers, Cold Regions Research & Engineering Laboratory.
Lal, A.W., Shen, H.T., 1991. Mathematical model for river ice processes. Journal of hydraulic Engineering 117, 851–867.
Lin, D., Grundmann, J., Eltner, A., 2019. Evaluating image tracking approaches for surface velocimetry with thermal tracers. Water Resources Research 55, 3122–3136.

Lindenschmidt, K.-E., Sereda, J., 2014. The impact of macrophytes on winter flows along the Upper Qu'Appelle River. Canadian Water Resources Journal/Revue canadienne des ressources hydriques 39, 342–355.
Liu, L., Shen, H.T., 2005. CRISSP2D Version 1.0 programmer's manual. CEE Report 05–19.
Liu, L., Shen, H.T., 2000. Numerical simulation of river ice control with booms.
Lu, S., Shen, H.T., Crissman, R.D., 1999. Numerical study of ice jam dynamics in upper Niagara River. Journal of cold regions engineering 13, 78–102.
Matousek, V., 1984. Types of ice run and conditions for their formation, in: IAHR International Symposium on Ice. Hamburg Germany, pp. 315–327.
Melling, A., 1997. Tracer particles and seeding for particle image velocimetry. Measurement science and technology 8, 1406.
Michel, B., Ramseier, R.O., 1971. Classification of river and lake ice. Canadian Geotechnical Journal 8, 36–45.
Okamoto, K., Nishio, S., Kobayashi, T., Saga, T., Takehara, K., 2000. Evaluation of the 3D-PIV standard images (PIV-STD project). Journal of Visualization 3, 115–123.
Osterkamp, T.E., 1978. Frazil ice formation: A review. Journal of the Hydraulics Division 104, 1239–1255.
Overland, J.E., 1985. Atmospheric boundary layer structure and drag coefficients over sea ice. Journal of Geophysical Research: Oceans 90, 9029–9049.
Overland, J.E., Pease, C.H., 1988. Modeling ice dynamics of coastal seas. Journal of Geophysical Research: Oceans 93, 15619–15637.
Paprota, M., 2020. Experimental study on spatial variation of mass transport induced by surface waves generated in a finite-depth laboratory flume. Journal of Physical Oceanography 50, 3501–3511.
Paprota, M., 2017. Experimental study on wave-current structure around a pneumatic breakwater. Journal of Hydro-environment Research 17, 8–17.
Patalano, A., Carlos Marcelo, G., Andrés, R., 2017a. A simple and user-friendly toolbox for large scale water surface Particle Image Velocimetry (PIV) and Particle Tracking Velocimetry (PTV). Computers & Geosciences 109, 323–330.
Patalano, A., García, C.M., Rodríguez, A., 2017b. Rectification of Image Velocity Results (RIVeR): A simple and user-friendly toolbox for large scale water surface Particle Image Velocimetry (PIV) and Particle Tracking Velocimetry (PTV). Computers & Geosciences 109, 323–330.
Prowse, T., Bonsal, B., Duguay, C., Lacroix, M., 2007. River-ice break-up/freeze-up: a review of climatic drivers, historical trends and future predictions. Annals of Glaciology 46, 443–451.
Pu, J., Ke, Z.-Q., Wang, J.-H., You, H.-D., Du, Z.-N., 2013. An experimental investigation on fluid flow characteristics in a real coolant channel of LP turbine blade with PIV technique. Experimental thermal and fluid science 45, 43–53.
Reyes, V.A., Sierra-Espinosa, F.Z., Moya, S.L., Carrillo, F., 2015. Flow field obtained by PIV technique for a scaled building-wind tower model in a wind tunnel. Energy and Buildings 107, 424–433.
Shan, H., Kerenyi, K., Patel, N., Guo, J., 2022. Laboratory test of second log-wake law for effects of ice cover and wind shear stress on river velocity distributions. Journal of Cold Regions Engineering 36, 04022001.
Shen, H.T., 2010. Mathematical modeling of river ice processes. Cold Regions Science and Technology 62, 3–13.
Shen, H.T., 2008. CRISSP2D User's Manual (No. 1.1). Department of Civil and Environmental Engineering Clarkson University, Potsdam, NY 13699-5710, U.S.A.
Shen, H.T., 2005. CRISSP2D Programmer's Manual. CEATI Report No. T012700-0401.
Shen, H.T., 2002. Development of a comprehensive river ice simulation system, in: Proceedings of the 16th International Symposium on Ice–Ice in the Environment. pp. 142–148.
Shen, H.T., 1996. River ice processes, in: 13th IAHR International Ice Symposium. beijing, China.

Shen, H.T., Gao, L., Kolerski, T., Liu, L., 2008. Dynamics of ice jam formation and release. Journal of Coastal Research 25–32.
Shen, H.T., Huang, F., 2024. Forecasting River Ice Breakup and Ice Jam Flooding, in: In the Process of Publication. Presented at the 27th IAHR International Symposium on Ice, Gdańsk University of Technology, Gdańsk, Poland.
Shen, H.T., Liu, L., 2003. Shokotsu River ice jam formation. Cold Regions Science and Technology 37, 35–49.
Shen, H.T., Lu, S., Crissman, R.D., 1997. Numerical simulation of ice transport over the Lake Erie-Niagara River ice boom. Cold regions science and technology 26, 17–33.
Shen, H.T., Shen, H., Tsai, S.M., 1990. Dynamic transport of river ice. Journal of Hydraulic Research 28, 659–671.
Shen, H.T., Su, J., Liu, L., 2000. SPH simulation of river ice dynamics. Journal of Computational Physics 165, 752–770.
Shen, H.T., Wang, D.S., Lal, A.W., 1995. Numerical simulation of river ice processes. Journal of Cold Regions Engineering 9, 107–118.
Sodhi, D.S., 1996. Ice action on riprap: Small-scale tests. DIANE Publishing.
Spreen, G., Kwok, R., Menemenlis, D., 2011. Trends in Arctic sea ice drift and role of wind forcing: 1992–2009. Geophysical Research Letters 38.
Stanislas, M., Kompenhans, J., Westerweel, J., 2013. Particle image velocimetry: Progress towards industrial application. Springer Science & Business Media.
Su, J., Shen, H.T., Crissman, R.D., 1997. Numerical study on ice transport in vicinity of Niagara River hydropower intakes. Journal of cold regions engineering 11, 255–270.
Tauro, F., Grimaldi, S., 2017. Ice dices for monitoring stream surface velocity. Journal of Hydro-environment Research 14, 143–149.
Tauro, F., Salvatori, S., 2017. Surface flows from images: ten days of observations from the Tiber River gauge-cam station. Hydrology Research 48, 646–655.
Techet, A.H., McDonald, A.K., 2005. High speed PIV of breaking waves on both sides of the air-water interface, in: 6th International Symposium on Particle Image Velocimetry. pp. 1–14.
Thomas Jr, E., Williams, J.D., Silver, J., 2004. Application of stereoscopic particle image velocimetry to studies of transport in a dusty (complex) plasma. Physics of plasmas 11, L37–L40.
Timgren, A., Trägårdh, G., Trägårdh, C., 2008. Application of the PIV technique to measurements around and inside a forming drop in a liquid–liquid system. Experiments in Fluids 44, 565–575.
Troitskaya, Y., Sergeev, D., Ermakova, O., Balandina, G., 2011. Statistical parameters of the air turbulent boundary layer over steep water waves measured by the PIV technique. Journal of physical oceanography 41, 1421–1454.
Unduche, F.S., Doering, J., 2007. Experimental study of the formation of different types of surface ice runs. Presented at the Submitted to the CRIPE conference, Quebec City, Canada.
Wang, C., Wei, Z., 2015. A virtual particle images generation system for 3D-PTV verification. Procedia Engineering 126, 554–558.
Wang, D.S., Shen, H.T., Crissman, R.D., 1995. Simulation and analysis of upper Niagara River ice-jam conditions. Journal of cold regions engineering 9, 119–134.
Wang, J., Hua, J., Sui, J., Wu, P., Liu, T., Chen, P., 2016. The impact of bridge pier on ice jam evolution–an experimental study. Journal of Hydrology and Hydromechanics 64, 75–82.
Watanabe, E., Hasumi, H., 2005. Arctic sea ice response to wind stress variations. Journal of Geophysical Research: Oceans 110.
Wazney, L., Clark, S.P., Malenchak, J., Knack, I., Shen, H.T., 2019. Numerical simulation of river ice cover formation and consolidation at freeze-up. Cold Regions Science and Technology 168, 102884.
Wolski, K., Tyminski, T., Gluchowska, B., 2017. Analysis of ice phenomena hazard on the middle Odra river. Annals of Warsaw University of Life Sciences-SGGW. Land Reclamation 49.

Wu, J., 1973. Prediction of near-surface drift currents from wind velocity. Journal of the Hydraulics Division 99, 1291–1302.
Wu, J., 1969. Wind stress and surface roughness at air-sea interface. Journal of Geophysical Research 74, 444–455.
Wu, J., 1968. Laboratory studies of wind–wave interactions. Journal of Fluid Mechanics 34, 91–111.
Yapa, P.D., Shen, H.T., 1984. Effect of ice cover on hydropower production. Journal of Energy Engineering 110, 231–234.
Zhai, B., Liu, L., Shen, H.T., Ji, S., 2022. A numerical model for river ice dynamics based on discrete element method. Journal of Hydraulic Research 60, 543–556.
Zhang, W., Wang, Y., Lee, S.J., 2008. Simultaneous PIV and PTV measurements of wind and sand particle velocities. Experiments in Fluids 45, 241–256.
Zhelezova, E., Krek, E., Chubarenko, B., 2018. Characteristics of the polynya in the Vistula Lagoon of the Baltic Sea by remote sensing data. International Journal of Remote Sensing 39, 9453–9464.
Zufelt, J.E., Ettema, R., 1996. Model ice properties. COLD REGIONS RESEARCH AND ENGINEERING LAB HANOVER NH.